

Transport Measurements of Single Wall Carbon Nanotube Multiterminal Devices with Normal and Ferromagnetic Contacts

INAUGURALDISSERTATION

zur
Erlangung der Würde eines Doktors der Philosophie
vorgelegt der
Philosophisch-Naturwissenschaftlichen Fakultät
der Universität Basel

von

Gunnar Gunnarsson
aus
Reykjavík (IS)



Basel, 2008

Genehmigt von der Philosophisch-Naturwissenschaftlichen Fakultät auf
Antrag von

Prof. Dr. Christian Schönenberger
Prof. Dr. Jean-Philippe Ansermet
Dr. Takis Kontos

Basel, den 16. November 2007

Prof. Dr. Hans-Peter Hauri, Dekan

*Vísindin efla alla dáð,
orkuna styrkja, viljann hvesa,
vonina glæða, hugann hressa,
farsældum vefja lýð og láð;
tífalda þakki því ber færa
þeim, sem að guðdómseldinn skæra
vakið og glætt og verndað fú
viskunnar helga fjalli á.*

Jónas Hallgrímsson. „Til herra Páls Gaimard“

Contents

1	Introduction	1
2	Spin transport – Spintronics	5
2.1	Introduction	5
2.2	Ferromagnetism	5
2.2.1	Origin of ferromagnetism	5
2.2.2	The spin polarization in ferromagnet	6
2.2.3	Anisotropy energy and Domains	7
2.2.4	Hysteresis and coercivity	8
2.2.5	Anisotropic magneto resistance – AMR	10
2.3	Giant magnetoresistance – GMR	11
2.4	Tunnelling magneto resistance	13
2.4.1	Jullière’s model	14
2.4.2	Datta Das transistor	16
2.5	The Conductivity mismatch problem	17
3	Carbon nanotubes	19
3.1	The geometry of carbon nanotubes	19
3.2	The band structure of graphene	20
3.3	The Band structure of SWCNT	22
3.4	SWCNT quantum dot	24
4	Sample processing	29
4.1	SWCNT based devices	29
4.2	Obtaining the wonder material	29
4.2.1	Estimating the quality of the nanotube material	30
4.2.2	Nanotubes from suspension solution	32
4.2.3	Nanotubes grown by Chemical Vapor Deposition – CVD	38
4.2.4	Which material to choose	43
4.3	Making of a SWCNT devices	43
4.3.1	Big pads and markers	45

4.3.2	Localizing suitable nanotubes for contacting	46
4.3.3	Making the contacts	47
5	Measurements on SWCNT spin-valves	49
5.1	The basic idea	49
5.2	Spin-valve devices	51
5.3	Ferromagnetic Contact materials	52
5.3.1	The ideal contact material	52
5.3.2	PdNi alloy	52
5.3.3	Co and NiFe	57
5.3.4	PdNi/Co bilayer	61
5.4	Temperature dependence of TMR	64
6	Non-local measurements	69
6.1	Introduction	69
6.2	Measurements	70
6.3	Resistor model	73
6.4	Possible source of oscillations	77
6.5	Conclusion	78
7	Summary	81
7.1	Obtaining SWCNT	81
7.2	Ferromagnetic contact material and switching characteristics .	81
7.3	Temperature dependence of TMR	82
7.4	Non-local measurements	82
A	The CVD procedure	89
A.1	The catalyst preparation	89
A.2	The oven and the gas handling system	89
A.3	The growing protocol	90
B	Measurement setups	93
B.1	Setup of the linear response measurements	93
B.2	Setup for doing grayscale measurements	94
	Publications	95
	Curriculum Vitae	97
	Acknowledgements	101

List of Figures

2.1	Split of electron band structure	6
2.2	Forming of domains	9
2.3	Magnetohysteresis of single domain particle and multidomain material	9
2.4	Anisotropic magnetoresistance	11
2.5	GMR. Current perpendicular to the plane	12
2.6	GMR in CIP spin-valve and equivalent resistor model	14
2.7	Tunnelling between two FM electrodes	15
2.8	Datta Das transistor	17
2.9	Conductivity mismatch problem solved	17
3.1	The definition of the wrapping vector of carbon nanotubes	20
3.2	Graphene unit cell	21
3.3	Band structure of graphene and the first Brillouine zone	22
3.4	Band structure of (9,0) and (10,0) SWCNT	23
3.5	Energy band of (9,0) and (10,0) nanotubes near K -point	25
3.6	Schematics of a quantum dot	26
3.7	Properties of SWCNT quantum dot	27
4.1	SEM and AFM pictures of nanotubes compared	31
4.2	AFM pictures of nanotubes	33
4.3	distribution of diameter and length of laser ablation nanotubes	33
4.4	SEM picture of SWeNT nanoubes spread directly from the solution	34
4.5	Gate response of nanotubes spread from suspension solution	35
4.6	SEM figures of tubes from suspension solution ready to be contacted	36
4.7	Gate response of semiconducting nanotubes	37
4.8	Two methods of spreading catalyst	38
4.9	SEM images of CVD grown nanotubes	40
4.10	Gate response of two CVD grown tubes at room temperature	41

4.11	Fourfold symmetry in SWCNT quantum dot	42
4.12	Electron beam lithography	43
4.13	Processing steps of the devices	45
4.14	The big pads and markers	46
5.1	Schematics of a SWCNT spin device and TMR curves	50
5.2	SEM picture of two types of spin devices	51
5.3	Magnetic moment of Pd _x Ni _{1-x} alloy as a function of x	53
5.4	Magnetic properties of PdNi/Pd film	54
5.5	Spin valve measurements using PdNi electrodes	55
5.6	Rotation of magnetization when field is applied out of plane	56
5.7	two examples of R as function of perpendicular H	57
5.8	MFM images of FM electrodes	58
5.9	Test device for Co and TMR measurements on Co devices	59
5.10	R as function of H in SWCNT contacted by Permalloy	60
5.11	PdNi/Co bilayer	61
5.12	Magnetic properties of PdNi/Co/Pd film	62
5.13	AMR measurements of PdNi/Co/Pd electrodes	63
5.14	Spin valve measurement on a SWCNT contacted with PdNi/Co electrodes	64
5.15	Temperature dependence of TMR	65
5.16	Temperature dependence of AMR	66
5.17	Conductance dependence of \sqrt{TMR}	67
6.1	Four terminal device and measurement setups	70
6.2	Characterization measurements on four terminal SWCNT device	71
6.3	Non local measurements as function of gate voltage	72
6.4	Non-local measurements with input resistance of 100 k Ω	73
6.5	The resistor model	74
6.6	Conductance measured between F2 and N4	77
6.7	Transmission through the F - N	78
A.1	A photo and schematics of the CVD system	90
A.2	The gas handling system	91
B.1	Setup of spin valve measurements	93

Chapter 1

Introduction

Spin based electronics or *spintronics* is a field having the electron's spin degree of freedom as a subject. It is about how to write, transfer and read information using the electron spin. The birth of spintronics is considered to be the discovery of the giant magnetoresistance (GMR) in 1988 [1] and since then a major progress has been achieved in the field [2, 3]. The best example of this progress is the development of so called spin-valves. Modern day spin-valves are based on the GMR and they are used for measuring small magnetic fields. Their most common application is as sensors in hard disk reading heads.

Spintronics can conceptually be divided in two parts. The first one is about generating and detecting spin polarized electrons, which is normally done using ferromagnetic materials, but can also be done using optical methods [3]. The latter part is about coherent transfer of spin information. It is of fundamental importance to understand how spin information can be transferred coherently over larger distances.

In recent years new nanoscale allotropes of carbon have been discovered. In 1985 the first fullerene, the buckyball was discovered [4] and 1991 carbon nanotubes (CNT) were discovered by Sumio Iijima [5]. CNTs behave as one-dimensional conductors and the coherence length of the electron in them is very long, especially in individual SWCNT, where the electrons have been found to be coherent over the distance of $3 \mu\text{m}$ [6]. Moreover, carbon is believed to have long spin coherence length, due to low spin orbit coupling and no nuclear spin of its main isotope ^{12}C . This all makes CNTs an interesting platform for spin transport studies.

The first work on CNT spin-valve devices was done on multiwall carbon nanotubes (MWCNTs) contacted by Co electrodes [7]. By applying magnetic field to the device the magnetization of the Co electrodes can be changed between parallel and antiparallel mutual orientation. The resistance for parallel

and antiparallel mutual orientation, R_P and R_A respectively, are measured and the TMR, which is defined as follows

$$TMR = \frac{R_A - R_P}{R_P}, \quad (1.1)$$

is calculated. The TMR of this first CNT spin-valve was 9% at maximum and it was positive (i.e $R_A > R_P$) [7, 8].

Negative TMR signal was later measured in similar devices, i.e. MWCNTs contacted with Co electrodes. The maximal size of the TMR signal in these devices was 36% for a low current bias, but higher current bias resulted in lower TMR signals [9]. The origin of the different sign of the TMR was not clear by then.

The first CNT spin devices fabricated in our lab were MWCNTs contacted by $\text{Pd}_{1-x}\text{Ni}_x$ ($x \approx 0.7$)¹. These ferromagnetic contacts were transparent, having room temperature resistance of 5.6 k Ω . What was new about these devices was that they were equipped with a back gate and could be tuned between different transport regimes [10]. More importantly it was shown that TMR was dependent on the back gate voltage [11]. Further studies revealed that the TMR signal was either negative or positive dependent on applied gate voltage, but the origin of this behavior was not well understood [12].

When the signal changes in TMR were studied single wall carbon nanotubes (SWCNT) grown in-house by chemical vapor deposition (CVD) using methane as a carbon source became available. The CVD growing process had been optimized to produce individual SWCNT [13]. Individual CVD grown SWCNTs were connected with PdNi contacts. In such device it was shown that the TMR signal was correlated with the coulomb oscillations of the quantum dot which is formed in the SWCNT between the contacts. In SWCNT the quantum dot behavior is much simpler than in MWCNT and the TMR could be tuned smoothly from positive to negative values by the gate voltage [12, 14]. This work demonstrated for the first time the control of spin transport in a three terminal device.

There are still many open questions concerning SWCNT spin devices. There are mainly two issues that one should be concerned about when constructing a SWCNT spin valve device. The first one is the switching characteristics of the electrodes. The switching in the devices contacted with PdNi contacts is not always clear indicating that the electrode consists of many magnetic domains.

The latter one is due to spurious effects in the SWCNT spin-valves. Such effects could be magneto-coulomb effect [15] or tunnelling anisotropic magnetoresistance (TAMR). Spurious effects could cause a “false TMR signal”,

¹ $\text{Pd}_{0.3}\text{Ni}_{0.7}$ will from now on be written as PdNi

i.e. a switching behavior in the signal as a function of applied field that does not originate from transport of spin.

The focus of this work was mainly to address these issues but some work was also done on how to process individual SWCNT devices. PdNi electrodes were studied in order to understand their switching behavior better. We worked to optimize the switching characteristics of the spin-valve devices, by trying other contact materials on the SWCNTs.

One way of avoiding spurious effects is to make multi-terminal devices. It has been shown in metallic nanostructures that by measuring non-local spin signals, artefacts can be avoided. Non-local spin transport measurements have been done on SWCNT contacted by four Co contacts [16]. The multiterminal devices made in this work have two normal contacts and two ferromagnetic contacts. They are gateable with a back-gate enabling it to study the behavior of the three quantum dots that are formed in each segment of the tube between the contacts.

Outline of this thesis

- **Chapter 2** is on the basics of spintronics. It includes a short description on ferromagnetism and on anisotropic magnetoresistance (AMR) and for historical reasons giant magnetoresistance (GMR) is briefly discussed. The tunnelling magnetoresistance is explained and Jullière's model.
- **Chapter 3** is on carbon nanotubes. It is focused on single wall carbon nanotubes (SWCNT), their structure and their electronic properties.
- **Chapter 4** is on processing of SWCNT devices. The first part of the chapter is on SWCNT production and characterization of the SWCNT material. A lot of time was invested in the lab in finding the best way to obtain individual SWCNT for our nanotube project. Both main approaches tested, i.e spreading tubes from suspension solution and CVD growth are described. In the latter part it is generally described how to make SWCNT devices.
- **Chapter 5** is on SWCNT based spin valves. The idea behind the SWCNT is discussed (the statement of the problem) and then measurements using different ferromagnetic contact materials are discussed. Temperature dependence on TMR in SWCNT is discussed in the last section of the chapter.
- **Chapter 6** is on measurements on multiterminal devices. Non-local and semi-nonlocal measurements are shown and discussed.

- **Chapter 7** is a summary of the thesis.

Details on experimental setups and recipes can be found in appendices.

Chapter 2

Spin transport – Spintronics

2.1 Introduction

Spin transport measurements date back to 1857 when Thomson (also known as Lord Kelvin) discovered the anisotropic magnetoresistance (AMR). In 1973 Tedrow and Meservey measured the spin polarization of ferromagnetic metals using tunneling from a ferromagnetic metal to a superconductor [17] and two years later, in 1975, Jullière discovered the tunneling magnetoresistance (TMR) [18].

The discovery of giant magnetoresistance (GMR) in 1989 [1] is considered to be the birth of spintronics as a research field. This was the first time that spin transport had been demonstrated in a non-magnetic material. GMR was embraced by the electronic industry. It is used to make so called spin-valves, which are very sensitive magnetic field detectors. GMR spin-valves are e.g. used as hard-disk read heads and the first GMR based hard-disk read heads were produced by IBM in 1997 [19]

In order to make a spintronic device one has to be able to generate and detect spin polarized electrons. This is normally done with ferromagnets as in this work, where SWCNT were contacted by electrodes of ferromagnetic metals.

2.2 Ferromagnetism

2.2.1 Origin of ferromagnetism

Ferromagnetism originates from the spins of not fully populated inner shells of the atoms. In transition metals it is the d shell, which is not completely full whereas in the rare earth metals it is the f shell. The interaction between

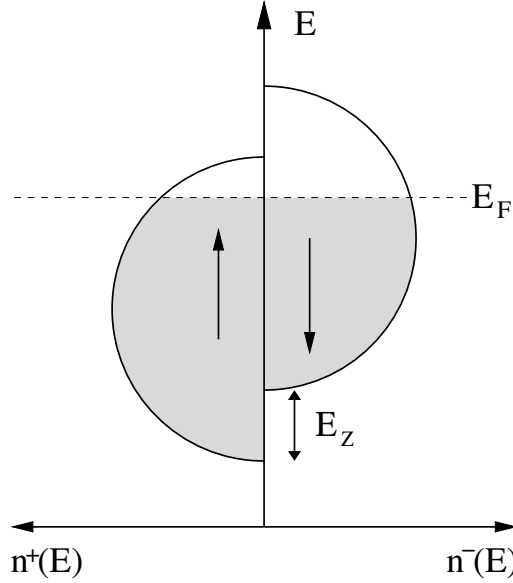


Figure 2.1: Bandstructure split due to exchange interaction E_z . The density of states for majority and minority spins ($n^+(E)$ and $n^-(E)$) are different. The magnetization points up.

two spins can be described by

$$U_{i,j} = -2J_{i,j}\mathbf{S}_i \cdot \mathbf{S}_j, \quad (2.1)$$

where $J_{i,j}$ is the overlap integral of the spins (see e.g. [20]). It is the $J_{i,j}$ that aligns the spins and in ferromagnets $J_{i,j} > 1$ for making it energetically favorable for the spins to be aligned parallel. The parallel ordering results in a net magnetization of the material. In general the situation is however more complicated. The size and sign of $J_{i,j}$ depends on the lattice structure of the material. Moreover the spins in the lattice are not necessarily all of the same size. All this can yield many types of spin ordering that are the subject of a vast field in physics: Magnetism (see e.g. [21]).

2.2.2 The spin polarization in ferromagnet

Due to the magnetic field induced by the ordered spins in ferromagnets the density of states as a function of energy is split. In Fig.2.1 the spin resolved density of states of the d electrons is sketched. Due to the splitting the density of states at Fermi energy differs between majority and minority spins [3]. In ferromagnetic metals it is custom to refer to the spins which are *parallel* to

the magnetization as *majority spins* and to the spins that are *antiparallel* to the magnetization as *minority spins* [17]. The spin polarization is defined as

$$P = \frac{n^+(E_F) - n^-(E_F)}{n^+(E_F) + n^-(E_F)}, \quad (2.2)$$

where $n^+(E_F)$ and $n^-(E_F)$ are the densities of states of majority and minority spins respectively at the Fermi energy. Because of the definition of *minority* and *majority* spins, the polarization can be negative, which is indeed the case in the sketch in Fig.2.1.

Spin polarization as it is defined in Eq.(2.2) is not possible to measure directly in a transport measurement. A more appropriate definition for transport measurements would be

$$P = \frac{I^+ - I^-}{I^+ + I^-}, \quad (2.3)$$

where I^+ and I^- are the currents of majority and minority spin electrons. Results on spin polarization from tunnelling measurements of Tedrow and Meservey ([17]) are better described by

$$P_T = \frac{n^+(E_F)|T_{\uparrow}| - n^-(E_F)|T_{\downarrow}|}{n^+(E_F)|T_{\uparrow}| + n^-(E_F)|T_{\downarrow}|}, \quad (2.4)$$

where $|T_{\uparrow}(\downarrow)|$ are the transmission matrixes for majority and minority spins respectively [22]. The spin polarization can also be measured using superconducting point contacts. In that case the definition of spin polarization would be

$$P_C = \frac{n^+(E_F)v_F^+ - n^-(E_F)v_F^-}{n^+(E_F)v_F^+ + n^-(E_F)v_F^-}, \quad (2.5)$$

where v_F^+ and v_F^- are the Fermi velocities for majority and minority spins respectively [22]

One should bear in mind that different measurement techniques for measuring spin polarization do not measure exactly the same thing and that is the reason why different methods yield different values of P [22].

2.2.3 Anisotropy energy and Domains

There are few things about the magnetic properties of ferromagnets that one should have in mind when constructing devices by contacting nanostructures using ferromagnetic electrodes. It is mainly the magnetic anisotropy and domain structure of the ferromagnet that is of importance.

Due to spin-orbit coupling, the electron wave functions of the spin controlling inner electrons have spheroidal and not spherical charge distribution, thus making the overlap energy ($J_{i,j}$) asymmetric. The asymmetry, which is tied to the direction of the spin, causes $J_{i,j}$ to have minima for spin orientation along certain crystallographic directions [20].

Co has a hexagonal crystal and the easy axis of the magnetization is along the hexagonal axis. Ferromagnets like Fe and Ni have a cubic crystal structure and easy axes of magnetization is along the edges of the cube [20, 23].

A bulk ferromagnet is normally divided into different regions or domains of parallel magnetization. This happens for single crystal bulk as well as for polycrystalline material. The domains are separated by transition layers called domain walls [23]. Due to the spin interaction energy and the crystalline anisotropy energy it costs energy to form the domain walls [20].

A homogeneously magnetized object induces a field around itself, as shown in Fig.2.2(a), which is called demagnetization field. The energy of the magnetic field is given by [24]:

$$E_m = \int_V B^2 dV \quad (2.6)$$

By splitting the magnet into areas of opposite magnetization the field energy (Eq.(2.6)) is lowered as shown in Fig.2.2(b) and (c). The lowest external magnetic field and thus the lowest field energy is obtained by the formation of so called closure domains, when the field lines are closed in the magnet as shown in Fig.2.2(d) [23]. For smaller magnetic particles (of size of 10 – 100 nm) the energy cost of forming domain walls overcomes the energy win of the demagnetizing field. The particles consist of one magnetic domain and thus are completely magnetized.

For single domain particles and smaller objects, especially of ferromagnetic materials with low crystalline anisotropy, the demagnetizing field plays a bigger role in defining the easy axis of magnetization. The demagnetizing field of a magnetic object is highly dependent on its shape and the orientation of magnetization. For an elongated structure the magnetic field energy (Eq.(2.6)) will be lower if the magnetization is along the elongated structure. This phenomenon is called shape anisotropy.

2.2.4 Hysteresis and coercivity

The energy of a single domain particle in an applied magnetic \mathbf{H} field is given by

$$E = -\boldsymbol{\mu} \cdot \mathbf{H} + KV \sin \theta, \quad (2.7)$$

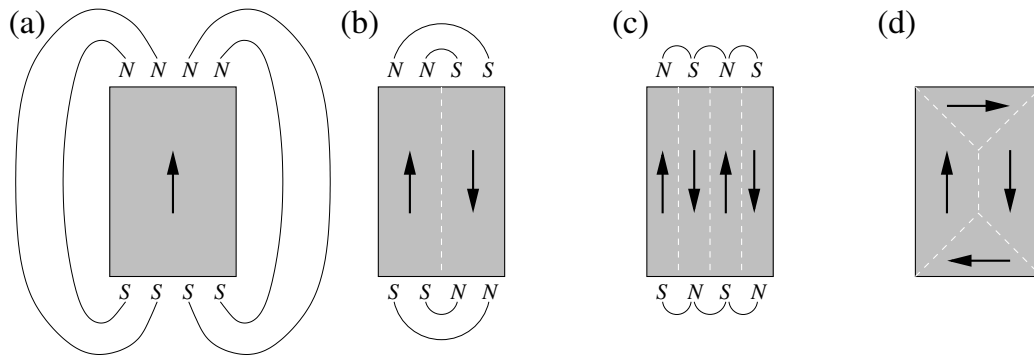


Figure 2.2: (a) The field around a magnetized object has an energy dependent on its strength and area (see Eq.(2.6)). This energy can be lowered by formation of domains. In (b) and (c) it is shown how the field is reduced when the object is split into areas of opposite direction. (d) So called closure domains minimize the demagnetizing field.

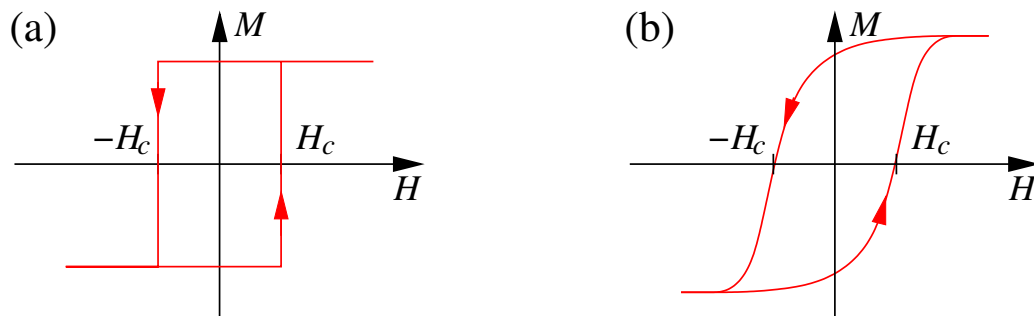


Figure 2.3: (a) Magnetohysteresis of a single domain particle. (b) Magnetohysteresis of a multidomain material.

where K is the anisotropy constant of the material, V the volume of the particle, μ its magnetic moment, and θ the angle between the magnetization direction and the easy axis [25]. For zero field an energy barrier of magnitude KV separates the two minima of $\theta = 0^\circ$ and $\theta = 180^\circ$. When the field is applied along the easy axis, the field strength needed to reverse the magnetization, the coercive field (H_c), is given by $H_c = KV/\mu$. When a field $H > H_c$ is applied in the opposite direction of the magnetization the magnetization reverses instantaneously. The the hysteresis curve of a single domain particle (M as a function of H) for H applied along the easy axis is sketched in Fig.2.3(a)

As mentioned above bigger ferromagnetic objects do normally consist of many magnetic domains. The net magnetization of all domains is far below the saturation magnetization of the ferromagnet. The switching of the magnetization with applied magnetic field is therefore not as simple as for the single domain case.

When the field is applied the domain walls move and the domains that are magnetized parallel to the applied field grown whereas others shrink. Only at higher magnetic fields, when the ferromagnet is approaching its saturation magnetization, the magnetization of the domains rotate to align to the applied field [20, 23]. The hysteresis curve of a multidomain object is sketched in Fig.2.3(b).

2.2.5 Anisotropic magneto resistance – AMR

Anisotropic Magnetoresistance (AMR) has been known for a long time. It was discovered by William Thomson in 1857 when he noticed that the resistivity of conductors of ferromagnetic metals depend on the orientation of their magnetization [26].

In Fig.2.4(a) it is shown how AMR manifests itself. At zero magnetic field a demagnetized polycrystalline ferromagnetic medium has the resistivity ρ_0 . When an external magnetic field is applied, the magnetic moments align themselves parallel along the field and the medium becomes magnetized. The resistivity changes when the medium becomes magnetized. The resistivity for current parallel to the magnetization (ρ_{\parallel}) and perpendicular to it (ρ_{\perp}) are different [27].

The resistivity of a ferromagnet is dependent on the angle θ between its magnetization (\mathbf{M}) and the current flow along it (\mathbf{J}) (see Fig.2.4(b)). In the first approximation this relation is given by:

$$\rho(\theta) = \rho_{\parallel} \cos^2 \theta + \rho_{\perp} \sin^2 \theta = \rho_{\perp} + \rho_{\Delta} \cos^2 \theta, \quad (2.8)$$

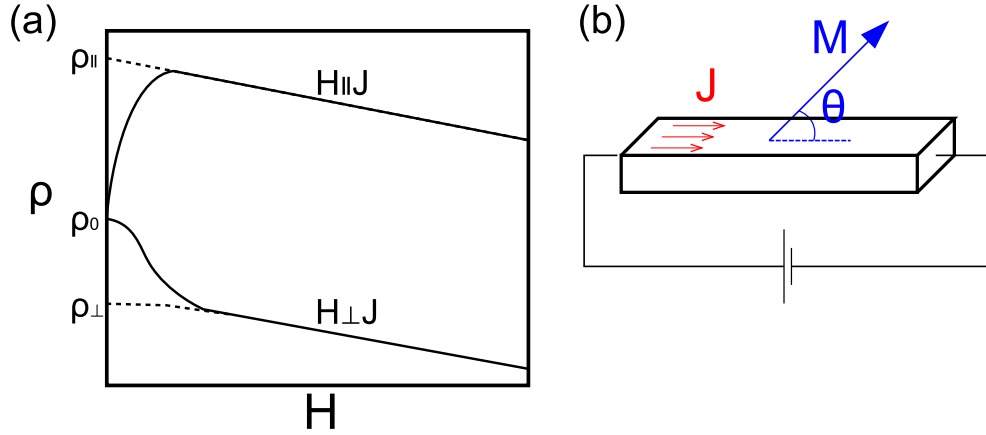


Figure 2.4: (a) resistivity ρ as function of magnetic field H when field is applied parallel (ρ_{\parallel}) and perpendicular (ρ_{\perp}) to the current flow (\mathbf{J}). (b) A current flow J in a magnetic conductor. The magnetization (\mathbf{M}) forms the angle θ to \mathbf{J} .

where $\rho_{\Delta} = \rho_{\parallel} - \rho_{\perp}$. ρ_{\parallel} is generally but not always greater than ρ_{\perp} [27]. The source of the asymmetry is spin-orbit coupling (see e.g.[27]).

The AMR can be used for monitoring the switching behavior of ferromagnetic electrodes. By measuring their resistance one can see if their magnetization are turning. The AMR is a relatively small effect. In $\rho_{\Delta}/\rho_{\parallel}$ is of the order of few % [27].

2.3 Giant magnetoresistance – GMR

The giant magnetoresistance (GMR) was discovered in 1988 as a large change in resistance in magnetic Fe/Cr multilayer in the presence of an applied magnetic field [1]. Soon after GMR was discovered in Fe/Cr/Fe trilayers [28]. As was shown later the effect can be obtained in trilayers having other magnetic materials such as Co [29].

Such trilayer structures, i.e. sandwiches of two ferromagnetic metals separated by a thin spacer layer of normal metal (see Fig.2.5), are of great industrial importance. They are called spin-valves and are used as magnetic field sensors. The resistance of the device is dependent on the relative magnetization orientation of the ferromagnets. It is R_P when the magnetizations are parallel and R_A when they are antiparallel. The GMR ratio is defined as

$$GMR = \frac{R_A - R_P}{R_P}. \quad (2.9)$$

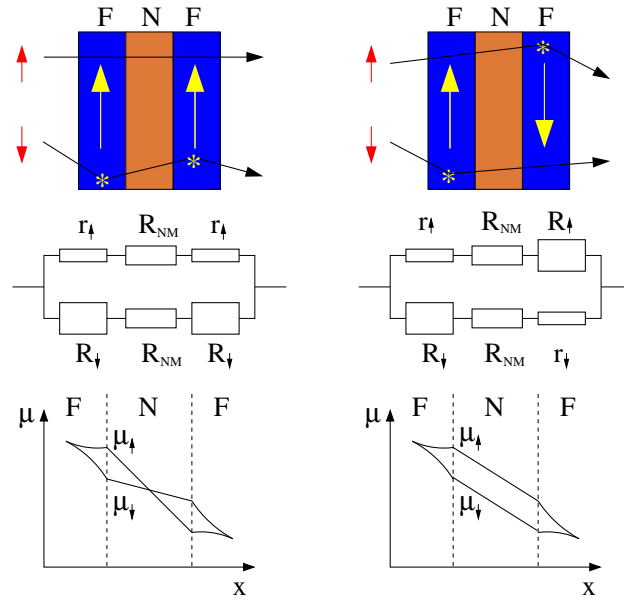


Figure 2.5: Giant magnetoresistance (GMR) device. A thin normal metal spacer (N) separates two ferromagnets (F). The current flows perpendicular to the plane of the sample. The equivalent resistor arrangement is shown in the middle. The resistivity for the minority spins is significantly higher than for the majority spin. The lowest schematics show how the chemical potential changes throughout the device when electronic potential is applied over it.

The resistance for the antiparallel magnetization is normally higher than for the parallel one. At zero applied magnetic field the relative orientation of the magnetization is governed by the exchange coupling between the ferromagnetic layers. The sign and size of the interlayer exchange coupling is dependent on the thickness of the nonmagnetic spacer. The coupling can thus be ferromagnetic and antiferromagnetic dependent on the spacer thickness [30, 31].

The device shown in Fig.2.5 is so-called current perpendicular to the plane (CPP) geometry. The resistance of such geometry is very low and difficult to detect. For practical applications, structures with the current in plane (CIP) are used because they have higher resistance and thus higher difference with magnetic field [29].

The GMR can be understood through Mott's two current model [32]. According to that the electrical conductivity of metal can be described by two more or less independent channels, one for majority spins and the other mi-

minority spins. Scattering processes that conserve spin states are much more probable than processes that flip spins.

Another point proposed by Mott is that the scattering probably of spin up and spin down is quite different, independent of the nature of the scattering process [33]. This is shown schematically in Fig.2.5. The resistance of the spin-valve is described by two channels in parallel having two resistors, two for each for each F layer and one for the spacer. The resistance for minority spins is significantly higher for majority spins

In the lowest row of Fig.2.5 the chemical potential for majority and minority spins is sketched when electrical potential is applied over the device. Due to the different resistance of the spins in the ferromagnetic layers their chemical potentials differ, also in the non-magnetic layer. This difference in the chemical potential of majority and minority spins in the non-magnetic layer is called spin accumulation.

The difference in the resistance in ferromagnets can be explained by the exchange split band structure. The scattering of the electrons depends on where the electron band cross the Fermi energy and due to the exchange splitting that can be significantly different between minority and majority spins [29]

As mentioned above commercial spin-valves have normally the Current In Plane (CIP) geometry. This gives higher resistance and thus higher resistance difference between parallel and antiparallel spin orientation. Having the current flowing in plane of the sandwich will qualitatively have the same effect as in CPP devices. This situation is shown schematically in Fig.2.6. Electrons with minority and majority spins are treated separately. When the electrons flow through the sandwich they will scatter back and forth from the upper F layer to the lower one. The resistivity corresponding to the scattering in the upper and lower F layer can thus be treated as resistors in series. The resistor model of CIP spin-valve is therefore the same as the resistor model for CPP devices.

2.4 Tunnelling magneto resistance

Tunnelling magneto resistance (TMR) was discovered in 1975 by M. Jullière [18] in a device that consisted of two Fe films separated by Ge. It was first in 1995 when room temperature TMR was discovered by J. S. Moodera [34] and in that time there was a booming interest in spintronics after GMR has been discovered in 1988 [1].

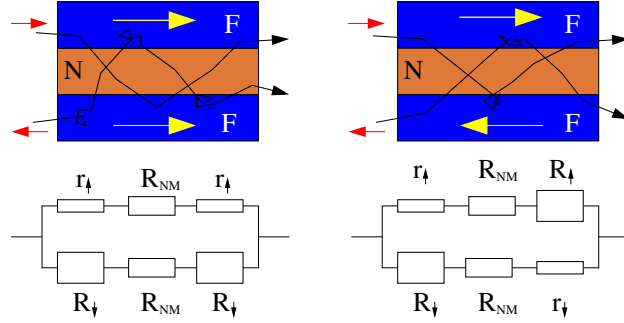


Figure 2.6: Current in Plane (CIP) spin-valve and equivalent resistor mode. Separate channels are for minority and majority spins. The electrons scatter from one F layer to the other on the way through the sandwich. The resistances corresponding to scattering in each F layer can be modelled as resistors in series.

The TMR signal is the same way as the GMR

$$TMR = \frac{R_A - R_P}{R_P} = \frac{G_P - G_A}{G_A}, \quad (2.10)$$

where $R_P (= 1/G_P)$ and $R_A (= 1/G_A)$ are the restances (conductance) of the device for parallel and antiparallel orientation respectively of the magnetization of the ferromagnets. The TMR is of quite different origin than the GMR.

2.4.1 Jullière's model

The Jullière's model is a simple model that describes the tunneling process between two ferromagnetic materials [18]. The device and the tunnelling process is shown schematically in Fig.2.7. The magnetization of the F electrodes, that are separated by a tunnelling barrier, is either parallel or antiparallel. The spin of the electrodes is conserved in the tunneling process and it's assumed that the spin up and spin down electrodes tunnel independently through the barrier.

The conductance of the barrier for both parallel and antiparallel orientation of magnetization can be estimated. When it is parallel, the majority spins of electrode 1 tunnel into the majority states of electrode 2 and the minority spins tunnel into the minority states. The tunneling is dependent on the density of states at the Fermi energy and thus the conduction obeys

$$G_P \propto n_1^+ n_2^+ + n_1^- n_2^-, \quad (2.11)$$

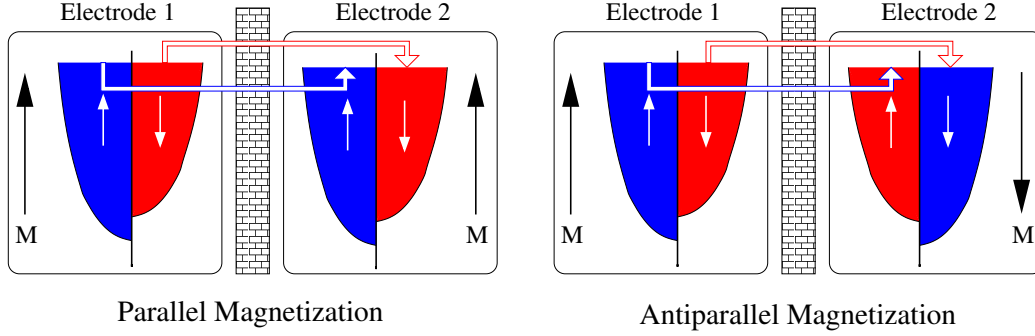


Figure 2.7: Two FM electrodes are separated by tunnelling barrier. When the magnetizations of the electrodes are parallel the majority spins of electrode 1 tunnel into the majority spins of electrode two and the minority spins into the minority spins. In the antiparallel orientation the majority spin of electrode 1 tunnel into the minority states of electrode 2 and the minority spins into the majority state.

where $n_{1(2)}^+$ and $n_{1(2)}^-$ is the density of majority and minority spins respectively at Fermi energy in electrode 1(2). In the antiparallel case the majority spins of electrode 1 tunnel into the minority states in electrode 2 and the minority spins tunnel into the majority states. The conductance of the device obeys

$$G_A \propto n_1^+ n_2^- + n_1^- n_2^+. \quad (2.12)$$

The TMR signal calculated by inserting Eq.(2.11) and Eq.(2.12) into Eq.(2.10) becomes

$$\begin{aligned} TMR &= \frac{G_P - G_A}{G_A} \\ &= \frac{n_1^+ n_2^+ + n_1^- n_2^- - (n_1^+ n_2^- + n_1^- n_2^+)}{n_1^+ n_2^- + n_1^- n_2^+}. \end{aligned} \quad (2.13)$$

Using definition of spin polarization,

$$P = \frac{n^+ - n^-}{n^+ + n^-} \Leftrightarrow \frac{n^+}{n^-} = \frac{1 + P}{1 - P}, \quad (2.14)$$

to rearrange Eq.(2.13) yields

$$TMR = \frac{2P_1 P_2}{1 - P_1 P_2}. \quad (2.15)$$

This formula is known as the Jullière's model for TMR¹ [18]. It does not

¹Other definitions are also used

$$TMR' = \frac{R_A - R_P}{R_A} = \frac{2P_1 P_2}{1 + P_1 P_2} \quad \text{and} \quad TMR'' = \frac{R_A - R_P}{R_A + R_P} = 2P_1 P_2$$

include spin flip effects nor does it depend on the properties of the tunnelling barrier.

Spin flipped in the tunnelling process

Spin flip processes can be included into the Jullière's model in a simple way. If γ is the ration between the spin conserving and spin flipping matrix elements, G_P and G_A (Eq.(2.11) and Eq.(2.12)) can be rearranged [35, 36]:

$$\begin{aligned} G_P &\propto n_1^+ n_2^+ + n_1^- n_2^- + \gamma(n_1^+ n_2^- + n_1^- n_2^+) \\ G_A &\propto n_1^+ n_2^- + n_1^- n_2^+ + \gamma(n_1^+ n_2^+ + n_1^- n_2^-). \end{aligned} \quad (2.16)$$

Calculating the TMR (Eq.(2.15)) gives:

$$TMR = \frac{(1 - \gamma) ((n_1^+ n_2^- + n_1^- n_2^+) - (n_1^+ n_2^+ + n_1^- n_2^-))}{n_1^+ n_2^- + n_1^- n_2^+ + \gamma(n_1^+ n_2^+ + n_1^- n_2^-)} \quad (2.17)$$

which can be rewritten using the definition of P

$$TMR = \frac{2(1 - \gamma)P_1 P_2}{1 - P_1 P_2 + \gamma(1 + P_1 P_2)}. \quad (2.18)$$

The magnitude of the TMR signal is according to this always diminished by spin-flip processes. This reduces to Eq.(2.15) if $\gamma = 0$ (as one would expect). In the other extreme, i.e. when all spin are flipped while tunnelling between the ferromagnets, $\gamma \rightarrow \infty$. The TMR signal becomes.

$$\lim_{\gamma \rightarrow \infty} \frac{2(1 - \gamma)P_1 P_2}{1 - P_1 P_2 + \gamma(1 + P_1 P_2)} = -\frac{2P_1 P_2}{1 + P_1 P_2} \quad (2.19)$$

which is always of opposite sign to Eq.(2.15). $\gamma = 1$ corresponds to the unpolarized case and results in $TMR = 0$

2.4.2 Datta Das transistor

According to Eq.(2.18) the TMR signal can be tuned if one can control the spins of the electrons in the tunnelling process, i.e rotate them coherently. A devices based on this idea, proposed by Datta and Das [37], so called Datta Das transistor, is shown schematically in Fig.2.8. A two dimensional electron gas (2DEG) is contacted by two ferromagnetic electrodes. The spins of the electrodes will rotate on the way between the electrodes. The change in their orientation is given by

$$\Delta\theta = 2m^* \eta L / \hbar^2, \quad (2.20)$$

where η is the spin-orbit coefficient. η can be tuned by applied gate voltage and thus the $\Delta\theta$.

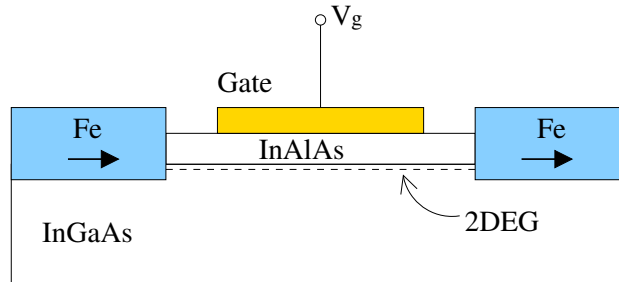


Figure 2.8: Datta Das transistor. Two dimensional electron gas (2DEG) is connected by two Fe electrodes that are parallelly magnetize in plane of the 2DEG. (Adapted from [37].)

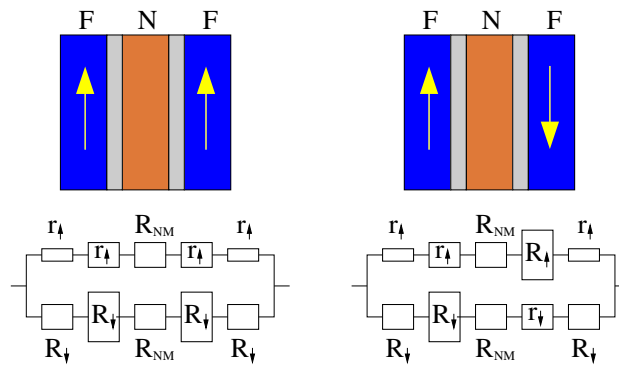


Figure 2.9: A way to solve the conductivity mismatch problem. A high spin dependent resistance, e.g. tunnelling barrier, is put between the ferromagnet and the spacer.

2.5 The Conductivity mismatch problem

A fundamental problem in spin injection is called the *the conductivity mismatch problem*. A semiconductor has usually much higher resistivity than the ferromagnets. In spin valve one wants to measure the difference of parallel and antiparallel magnetization of the FM electrodes. If the resistance of the spacer is high this difference is only a small fraction of the total signal and hard to detect [38]

One solution of this problem is to introduce a high spin dependent resistance between the ferromagnet and the spacer (see Fig.2.9). This could be a spin dependent tunnelling barrier [38]. This solution would give a larger difference in the R_P and R_A

Another solution would be to use half metal such as LaSrMnO_3 (LSMO) [19]. Such material can have spin polarization that is almost 100% [39]. Ferromagnetic metals have lower spin polarization. The polarization of Co that has the highest polarization of the elemental ferromagnets is $P = 45\%$.

Chapter 3

Carbon nanotubes

3.1 The geometry of carbon nanotubes

Needle like structure of concentric graphene shells, carbon nanotubes, were discovered by Sumio Iijima in 1991. The number of shells was typically ranging from 2 to about 50 and the diameter of the tubes was from 4 nm to 30 nm and their length was up to 1 μm [5]. The graphene shells are rolled up and make a seamless contacts. The molecular structure is thus continuous around the tube.

Since their discovery, carbon nanotubes have received a lot of interest due to their unique electrical and mechanical properties. There have been great improvements in the production of nanotubes. It is now possible to grow carbon nanotubes of single graphene shell, so-called Single Wall Carbon Nanotubes (SWCNT). Due to their small diameter and simplicity SWCNT are very interesting as a platform for research on mesoscopic systems.

The structure of SWCNT is described by so-called wrapping vector or chirality vector \mathbf{W} , which describes how a graphene sheet is rolled up. The crystal structure of graphene is shown schematically in Fig.3.1. The distance between adjacent atoms is $a_0 = 1.42 \text{ \AA}$. The base vectors used to describe the Bravais lattice of graphene, \mathbf{a}_1 and \mathbf{a}_2 (see Fig.3.1), have the length $a = \sqrt{3}a_0 = 2.46 \text{ \AA}$. The wrapping vector (\mathbf{W}), is given by

$$\mathbf{W} = n\mathbf{a}_1 + m\mathbf{a}_2, \quad (3.1)$$

where $n, m \in \mathbb{N}$ are called wrapping indices (see Fig.3.1). \mathbf{W} is the vector that connects two points that will fall together when the graphene sheet is rolled up. The radius of the nanotube is

$$d = \frac{a}{\pi} \sqrt{m^2 + mn + n^2}. \quad (3.2)$$

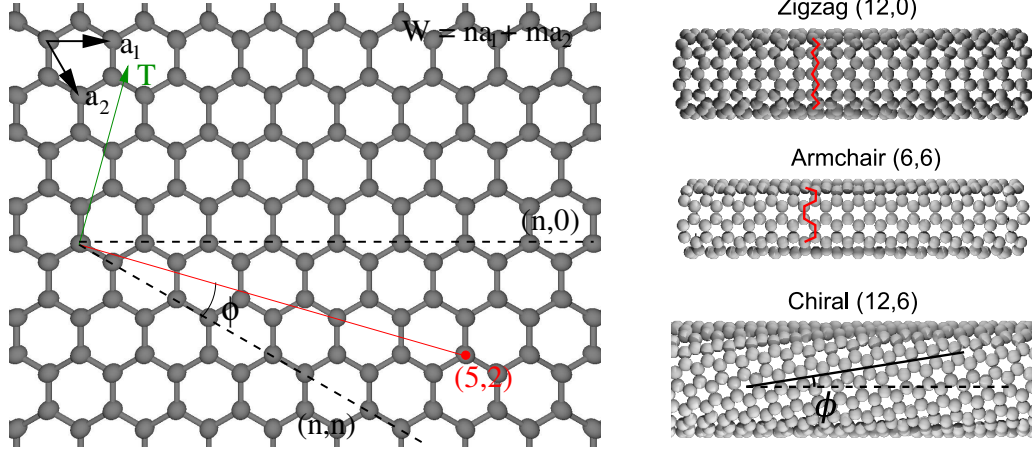


Figure 3.1: A graphene sheet shown schematically. \mathbf{a}_1 and \mathbf{a}_2 are the base vectors of the two dimension graphene lattice. The chiral vector, often given by two indices (n, m) , defines how the graphene is rolled. The three different types of structures of carbon nanotubes are shown to the left.

There are two special kinds of tubes. Tubes with wrapping indices $(n, 0)$ are called *zigzag tubes* and tubes having wrapping indices (n, n) are called *armchair tubes*. Other tubes are called *chiral tubes*. These three tube types are shown in Fig.3.1. The direction vector of the nanotube (\mathbf{T}) forms an angle ϕ to the graphene lattice called chiral angle (ϕ). ϕ is given by.

$$\phi = \arccos \left(\frac{\sqrt{3}(m+n)}{2\sqrt{m^2 + nm + n^2}} \right). \quad (3.3)$$

It takes values in the range $\phi = 0^\circ$ for armchair tubes to $\phi = 30^\circ$ for zigzag tubes.

3.2 The band structure of graphene

Graphene has interesting electrical properties and has received a lot of attention recently [40]. Single Walled Carbon Nanotubes (SWCNT) are special cases of graphene and their electronic properties can be derived from the properties of Graphene. As said above, a carbon nanotube is a graphene plate rolled up making a seamless contact. The electronic properties of SWCNT can be derived by applying the appropriate periodic boundary condition on the graphene.

In Fig.3.2 the unit cell of graphene is shown. Each unit cell has two carbon atoms located at \mathbf{x}_1 and \mathbf{x}_2 . The band structure of graphene can

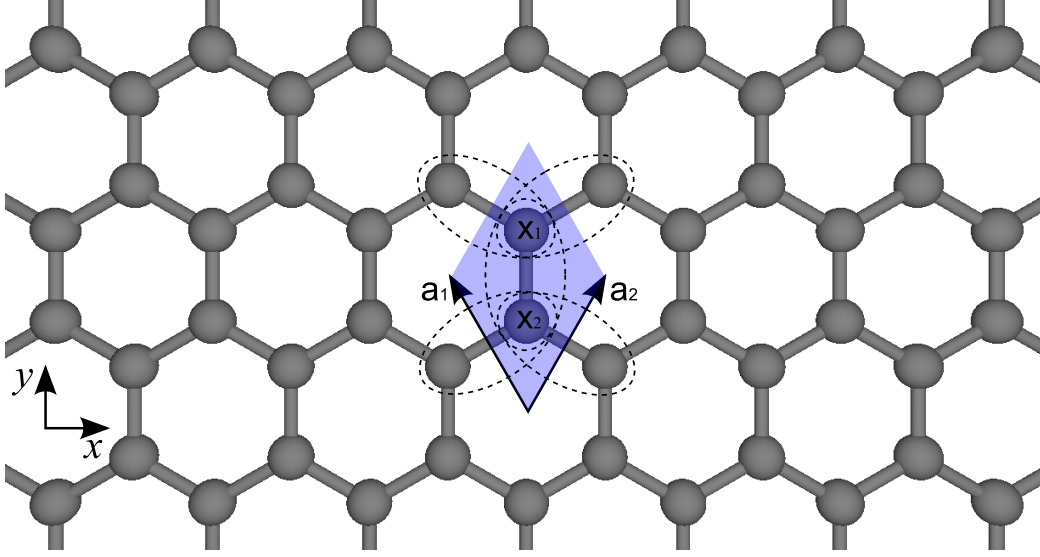


Figure 3.2: The Graphene unit cell (shaded) defined by the base vectors \mathbf{a}_1 and \mathbf{a}_2 . Two carbon atoms are in each cell at position \mathbf{x}_1 and \mathbf{x}_2 .

be calculated using the tight binding method. The wave function of the electrons is given by

$$\psi_{\mathbf{k}} = \sum_{\mathbf{R} \in G} \phi(\mathbf{x} - \mathbf{R}) e^{i\mathbf{k} \cdot \mathbf{R}}, \quad (3.4)$$

where G is the set of lattice vectors and $\phi(x)$ is the atomic wave function in each unit cell. $\phi(x)$ is a linear combination of the atomic wave functions of both carbon atoms in the unit cell

$$\phi(\mathbf{x}) = b_1 \phi_1(\mathbf{x}) + b_2 \phi_2(\mathbf{x}). \quad (3.5)$$

The Hamiltonian of the electrons in the system is given by

$$H = \frac{\mathbf{p}^2}{2m} + \sum_{\mathbf{R} \in G} (V_{at}(\mathbf{x} - \mathbf{x}_1 - \mathbf{R}) + V_{at}(\mathbf{x} - \mathbf{x}_2 - \mathbf{R})), \quad (3.6)$$

where $V_{at}(\mathbf{x})$ is the atomic potential of a carbon atom, \mathbf{p} is the electron momentum, and m the electron mass. The eigenvalue problem $H\psi_{\mathbf{k}} = E(\mathbf{k})\psi_{\mathbf{k}}$ is solved assuming only nearest neighbor interaction (see Fig.3.2). It yields a following dispersion relation for graphene [41]

$$E(k_x, k_y) = \pm \gamma \sqrt{1 + 4 \cos\left(\frac{\sqrt{3}ak_y}{2}\right) \cos\left(\frac{ak_x}{2}\right) + 4 \cos^2\left(\frac{ak_x}{2}\right)}, \quad (3.7)$$

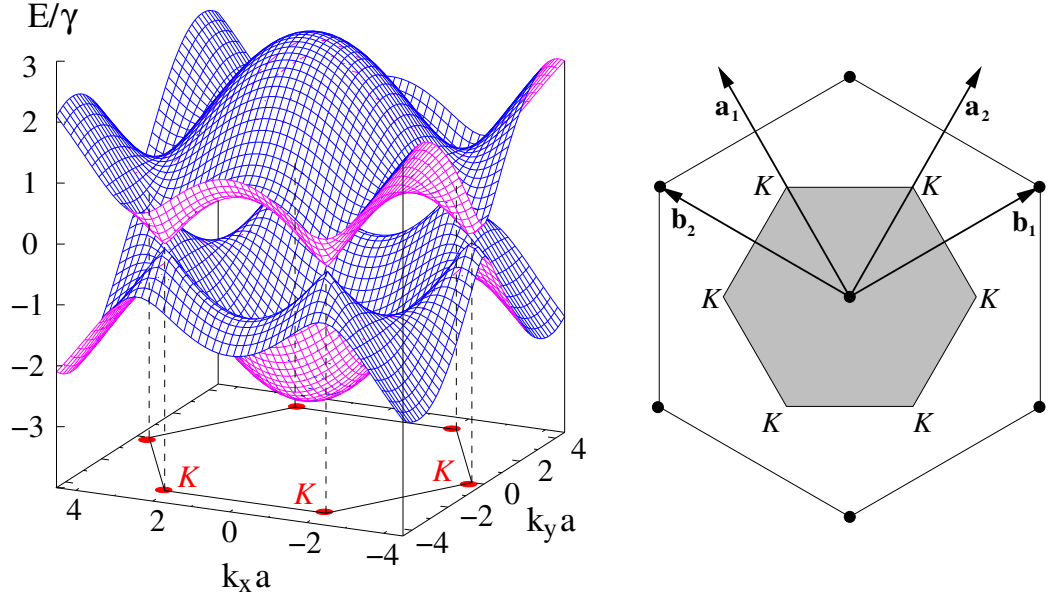


Figure 3.3: Band structure of graphene (left) and the first Brillouin zone (right). \mathbf{a}_1 and \mathbf{a}_2 are the base vectors of the graphene crystal and \mathbf{b}_1 and \mathbf{b}_2 corresponding reciprocal vectors. The points in the k -space, where the valence band and the conduction band touch is called K -points. They are located on the corners of the first Brillouin zone.

where γ is the nearest neighbour transfer integral, which takes value between 2.5 and 3.0 eV [42]. The band structure of graphene and the first Brillouin zone in the reciprocal lattice is plotted in Fig.3.3. The valence band and the conduction band touch each other at so-called K -points on the corners of the first Brillouin zone. These touching points are important when it comes to carbon nanotubes. Before coming to that it is useful to look at the expansion of the band structure around the K -points. $\boldsymbol{\kappa}$ is defined as the distance of \mathbf{k} from a K -point ($\boldsymbol{\kappa} = \mathbf{k} - \mathbf{K}$). The energy around the K point is given by

$$\epsilon(\boldsymbol{\kappa}) = \pm \hbar v_F |\boldsymbol{\kappa}|, \quad (3.8)$$

where the $v_F = 3\gamma a_0 / 2\hbar$ is the Fermi velocity. $a_0 = 1.42 \text{ \AA}$ and $\gamma = 2.9 \text{ eV}$ give a Fermi velocity of $v_F = 9.4 \times 10^5 \text{ m/s}$.

3.3 The Band structure of SWCNT

When rolling up the graphene sheet to make SWCNT as previously described, periodic boundary condition around the circumference of the tubes is invoked.

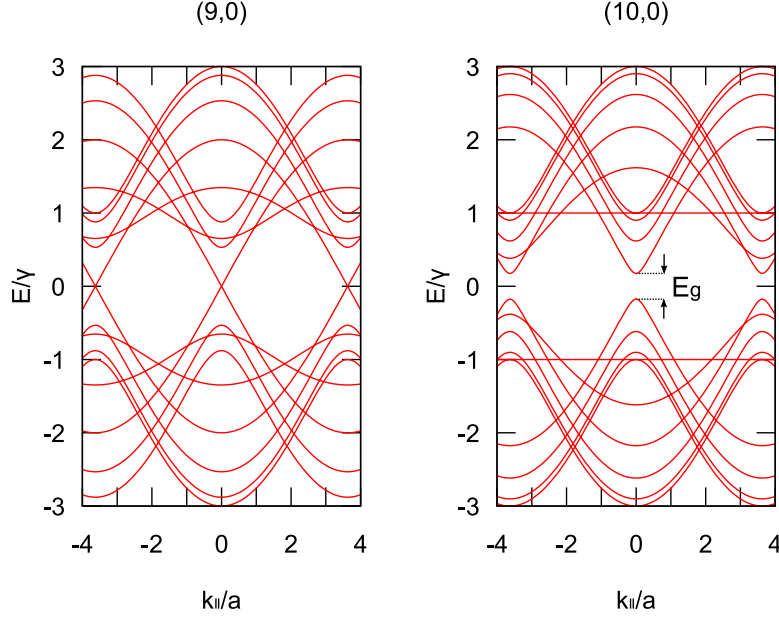


Figure 3.4: The band structure of (9,0) and (10,0) armchair nanotubes. The (9,0) tube is metallic while the (10,0) is semiconducting.

The wave vector \mathbf{k} can be written as

$$\mathbf{k} = k_{\parallel} \mathbf{e}_{\parallel} + k_{\perp} \mathbf{e}_{\perp}, \quad (3.9)$$

where \mathbf{e}_{\parallel} and \mathbf{e}_{\perp} are unit vectors parallel and perpendicular to the nanotube. k_{\parallel} has no restrictions but k_{\perp} obeys the periodic boundary condition $k_{\perp} = 2\pi p/d\pi$ where d is the diameter of the tube and $p \in \mathbb{N}$. Calculating k_x and k_y as a function of k_{\parallel} and k_{\perp} and using Eq.(3.7) gives the band structure. Two examples can be seen in Fig.3.4, where the band structure of two armchair nanotubes having the wrapping indices (9, 0) and (10, 0) are shown. The (9, 0) tube is metallic while the (10, 0) tube is semiconducting.

In order to get a general result on the electrical properties of SWCNT, i.e. to obtain the electrical properties of tubes with the wrapping indices m and n , it is better to use the expansion around the K -point. Like \mathbf{k} in Eq.(3.9) κ has two components κ_{\parallel} and κ_{\perp} , which are parallel and perpendicular to the tube, and the periodic boundary conditions on \mathbf{k} give following quantization of κ_{\perp}

$$\kappa_{\perp} = 2\pi \frac{(m-n)/3 + p}{\pi d}, \quad (3.10)$$

where $p \in \mathbb{Z}$. For tubes with wrapping indices m and n , where $(m-n)/3 \in \mathbb{Z}$, κ_{\perp} can be zero. The band structure around the K -point can be calculated by putting Eq.(3.10) into Eq.(3.8), which gives

$$\epsilon(\kappa_{\parallel}) = \pm \frac{2\hbar v_F}{d} \sqrt{\left(\frac{m-n}{3} + p\right)^2 + \left(\frac{\kappa_{\parallel} d}{2}\right)^2}. \quad (3.11)$$

Two examples of band structure around K -point are shown in figure Fig.3.12. An important result is that when $\kappa_{\perp} = 0$ $\epsilon(\kappa_{\parallel})$ becomes zero when $\kappa_{\parallel} = 0$. This means that the lowest conduction band and the highest valence band touch each other and the tubes are metallic. Thus all tubes having wrapping indices (m, n) where $(m-n)/3 \in \mathbb{Z}$ are metallic. This means that for tubes having coincidental wrapping vectors 1/3 of them are *metallic* and 2/3 *semiconducting*. This is an important result. Methods of producing SWCNT give tubes with wide distribution of the wrapping vector. The statistics on the electrical properties of the tubes can give valuable information on the quality of the material. It should be noted that one sometimes talks about a third type of nanotubes, so-called *small bandgap nanotubes*. That tubes are in fact metallic tubes, but due to perturbation the lowest conduction band and the highest valence band do not touch each other in at the K -point. This results in a small band gap.

Another important result is the size of the bandgap. The minimal value that $|(m-n)/3 - p|$ can take when $(m-n)/3 \notin \mathbb{Z}$ is 1/3. That means that the value of $|\epsilon(0)|$ for semiconducting tubes is $2\hbar v_F/3d$. The size of the bandgap is thus given by

$$E_g = \frac{4\hbar v_F}{3d} = \frac{4\pi\hbar v_F}{3a\sqrt{m^2 + mn + n^2}}, \quad (3.12)$$

i.e. the bandgap is inversly proportional to the tube's diameter, d . For example the size of the bandgap of a (10,0) tube is $E_g = 1.1$ eV.

3.4 SWCNT quantum dot

Basic concepts of a quantum dot

Quantum dots are objects, in which the electronic wave function is confined in such way that, due to boundary conditions, the energy of the electrons becomes quantized. Quantum dots have been realized in varous different systems, such as two dimensional electron gas semiconductor heterostructures that is confined using top gates and in carbon nanotubes.

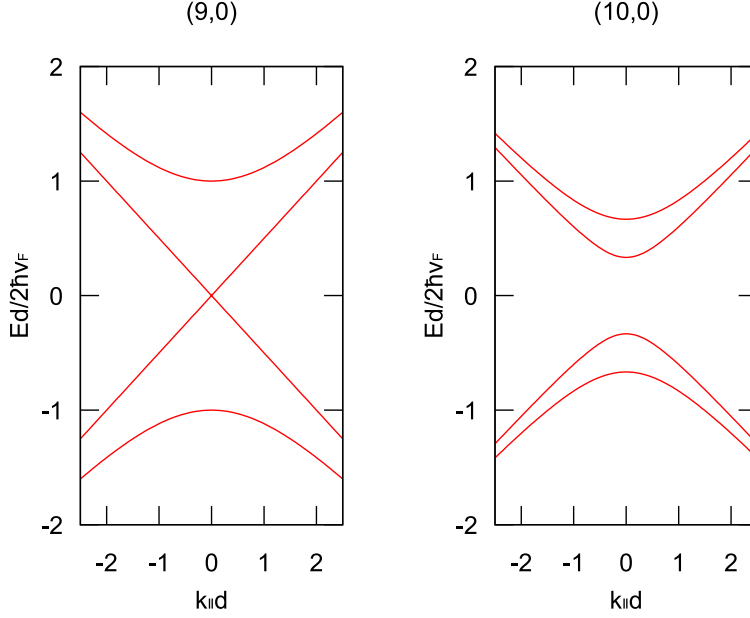


Figure 3.5: Energy bands of (9,0) and (10,0) nanotubes near K -point. The four bands nearest to the gap region are plotted. This scaling (i.e. plotting $E_d/2\hbar v_F$ as function of $k_{\parallel}d$) does only distinguish between metallic and semiconducting tubes.

Fig.3.6(a) depicts the schematics of a quantum dot. The dot is connected by two contacts, the source (S) and the drain (D) having the capacitances C_s and C_d respectively to the quantum dot. A gate having the capacitance C_g to the dot can be used to tune the energy of the electron levels in the dot. The total capacitance of the dot is $C_{\Sigma} = C_s + C_d + C_g$. By applying voltage V_g on the gate, the energy levels of the dot are shifted by

$$\Delta E_n(V_g) = \frac{C_g}{C_{\Sigma}} V_g = \alpha V_g, \quad (3.13)$$

where α is the active gate coupling. In Fig.3.6(b), the energy landscape of the dot is shown schematically. The source and the drain are separated from the dot by potential barriers. The chemical potential of the source and drain is μ_s and μ_d respectively and the source drain voltage is defined as $V_{sd} = \mu_s - \mu_d$. The spacing between the energy levels of the dot is δE and the position of the levels can be tuned by the V_g as explained above. In Fig.3.6(c), transport measurements of the dot are shown. The upper part shows the conductance

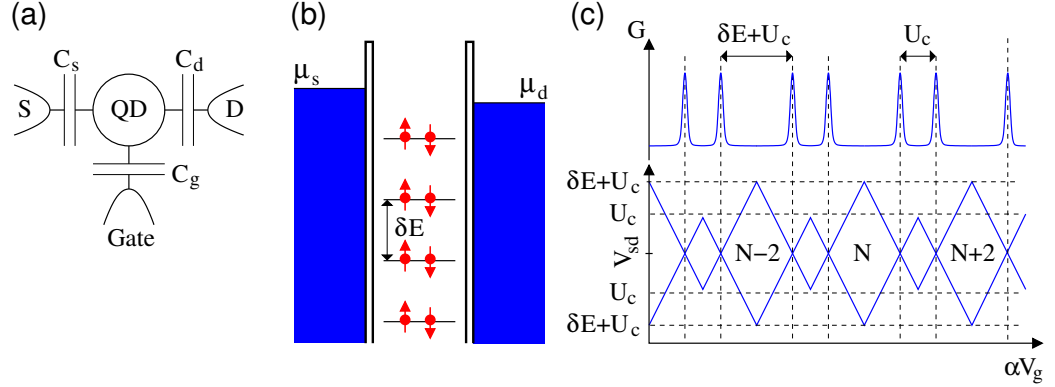


Figure 3.6: (a) Schematics of a quantum dot. The source (S), the drain (D), and the gate have the capacitances C_s , C_d , and C_g respectively to the dot (b) The potential landscape of the dot and the electrodes. The chemical potential of the source and the drain is μ_s and μ_d respectively, The spacing of the dots energy levels is δE . (c) Linear response, conductance (G) as function of gate voltage (V_g), and the stability diagram of the dot.

(G) as function of V_g when V_{sd} is small ($V_{sd} \ll \delta E$), the so-called linear response. Peaks appear in G when the energy levels are filled. The spacing of the peak when an empty level is filled with one electron till it's filled with the next one is $U_c = e^2/2C_\Sigma$ i.e the single electron charging energy of the dot. The spacing between a peak corresponding to filling a level with the second electron and the peak corresponding to adding the first electron to the next level is $\delta E + U_c$. The lower part of Fig.3.6(c) is the stability diagram of the dot. The stability of the dot is dependent on V_g and V_{sd} . The number of electrons is stable inside the so-called Coulomb diamonds.

In so-called grayscale measurement the differential conductance, dG/dV_{sd} , is measured as function of V_{sd} and V_g . The stability diagram is thus obtained from the grayscale plot. The edges of the Coulomb diamonds appear as a high differential conductance in such measurements. Inside the diamonds the differential conductance is zero if no second order tunnelling processes are present.

Quantum dot in SWCNT

When a carbon nanotube is contacted with two electrodes that form a barrier to it (see Fig.3.7(a)) a quantum dot is formed. The metal contacts form a barrier in the tube and k (parallel to the tube) becomes quantized. The quantization is given by $k = \pi n/L$, where $n \in \mathbb{N}$, assuming very high potential

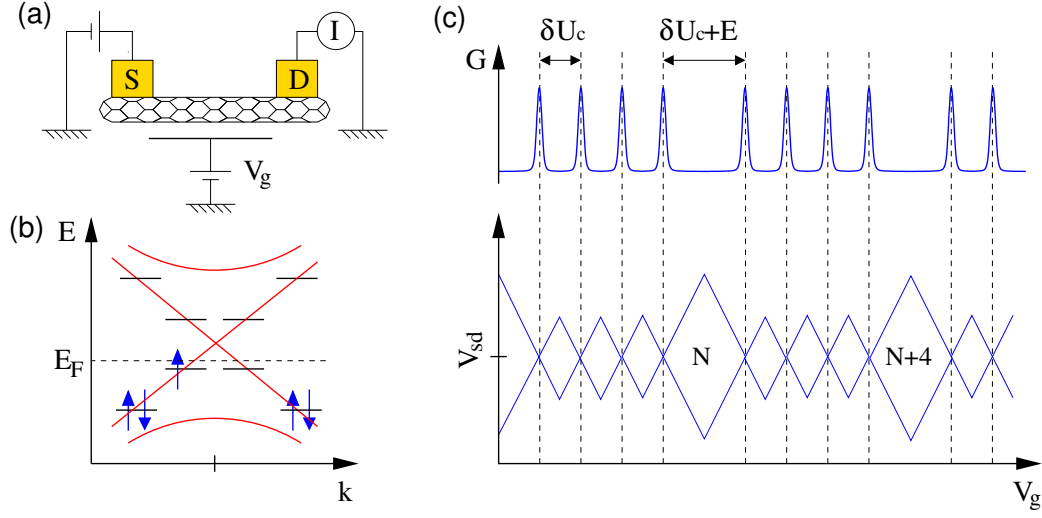


Figure 3.7: (a) SWCNT contacted by two electrodes. Between the electrodes quantum dot is formed that can be tuned by a gate. (b) Band structure of metallic SWCNT; when the tube is contacted, k becomes quantized. The degeneracy is fourfold when the Fermi energy (E_F) is localized where only one band is present. (c) Linear response, G as function of V_g and stability diagram of a SWCNT quantum dot. The Coulomb peaks and diamonds form a fourfold pattern.

barriers. The resulting energy level spacing at the Fermi energy is

$$\delta E = \frac{h v_F}{2L} \quad (3.14)$$

As can be seen in Fig.3.7(b) the quantization of k causes fourfold degeneracy of the energy levels, when the Fermi energy (E_F) is, where only one band is present. In Fig.3.7(c) the G measured as function of V_g and the stability diagram (dG/dV_{sd} as function of V_g and V_{sd}) are depicted. Due to the fourfold degeneracy the Coulomb peaks in G and the diamonds of the stability diagram have a fourfold pattern.

This fourfold pattern is a hallmark of a good metallic SWCNT. It is not often seen in semiconducting tubes because of the short distance between the first and second band nearest to the band gap (see Fig.3.5). Tubes, which are bundled or have a high density of defects lack the fourfold symmetry.

Chapter 4

Sample processing

4.1 SWCNT based devices

As discussed in previous chapter Single Wall Carbon Nanotubes (SWCNT) have unique electrical properties. These properties make them an ideal platform for studying the phenomena of quantum mechanics. For doing so we need to get the wonder material on a surface, find a suitable tube and contact it.

4.2 Obtaining the wonder material

When looking for suitable nanotube material one is mainly concerned about four issues. Firstly, the nanotubes should be single walled. Secondly one wants individual tubes because the unique electronic properties of SWCNT are much better resolved when only one tube is contacted. Thirdly, the nanotubes have to be long enough to be able to make the devices of interest, and finally the density of the tubes on the surface should be such that it is possible to find and contact a nanotube without shorts from other tubes.

There are two ways of getting nanotubes on a surface. They can be spread from a suspension solution or they can be grown there directly. When the nanotubes are spread on the surface one uses material that is grown by methods that are known for making material of high quality, such as High Pressure Carbon monoxide (HiPCO) growth or laser ablation . A powder of nanotubes is produced in both of these methods. The powder is dissolved in a solution and purified. SWCNT have a strong tendency to form ropes and in the purifying process the ropes are separated using ultrasound and bigger (heavier) particles are separated from the solution. As said above the advantage of spreading the nanotube material from suspension solution

is that one can use material which is known to have a high quality. The disadvantage is that preparing the solution and spreading it to the substrate is complicated.

The SWCNT can also be grown directly on the surface by Chemical Vapor Deposition (CVD). The advantage of CVD, is that one avoids the post growth processing of the nanotube material (dissolving the powder in a solution and processing it). The CVD process however must be optimized in order to get the wanted material, i.e. individual SWCNT, and there are many parameters to be optimized.

Both approaches have been tested in this work in order to obtain the “wonder material”. The material was spread or grown on SiO₂ substrate, i.e. the same surfaces as used for device fabrications, and the quality of the material check there.

4.2.1 Estimating the quality of the nanotube material

Visual characterization

The quality of the nanotube material was estimated by imaging the tubes on the surface using SEM and/or AFM. The shape of the tubes on the surface can tell a lot about their quality. Bundling manifest itself e.g. by branching, i.e. when tubes split into two or more tubes. Bendings are indication of bundling and/or structural defects and curved tubes are most probably ropes. By AFM one can measure the diameter of the tube. If the tube is 1 nm wide or less it is likely to be a single tube. (Some groups use 1.3 nm as limit). Individual SWCNT without structural defects should be straight with small diameter. For practical reasons, it was preferred to use SEM when estimated the quality of the material. Operating an AFM is very time consuming compared to using SEM. Even though one does not have the possibility of measuring the diameter of the tubes in the SEM one can learn much about the quality of the material from the shape of the tubes.

The electron microscope used was LEO Supra 35, which is equipped with an in-lens detector, which detects back-scattered electrons. When the sample is tilted ($\sim 30^\circ$ from horizontal) and the in-lens detector is used, the nanotubes appear clearly on the SEM images. The acceleration voltage is kept low or at 1 kV or lower.

An important question concerning the use of SEM for imaging such a narrow structures like SWCNT is, if the resolution of the SEM is high enough to resolve all tubes? In order to answer this question few samples were imaged with both AFM and SEM. Comparisons of SEM and AFM images of the same area have revealed that all tubes seen with AFM can also be seen

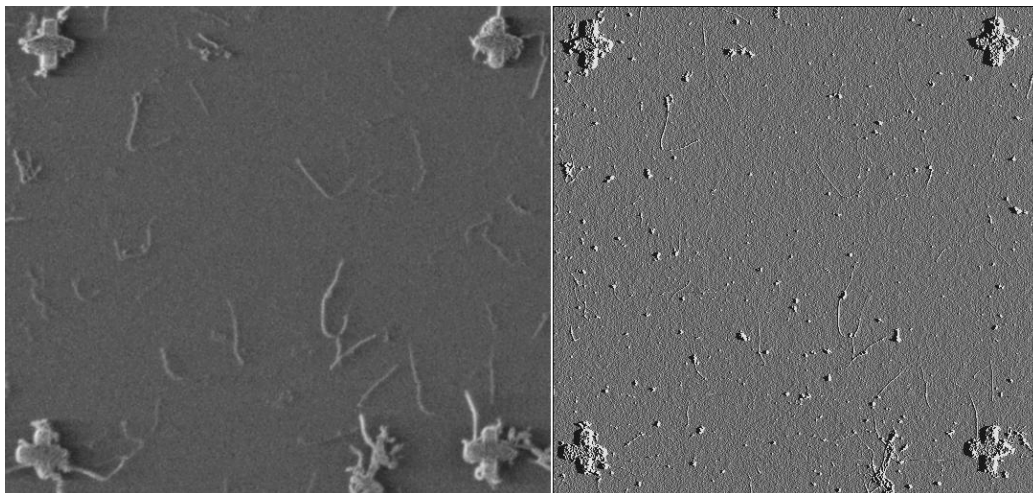


Figure 4.1: SEM picture (left) and AFM picture (right) of the same nanotubes compared. All nanotubes that can be seen in AFM can also be seen in SEM.

in SEM. An example of such comparison can be seen Fig.4.1. The tubes are even better visible in the SEM images than in the AFM, especially if the surface is rough.

Electrical characterization

When the density and the shape of the tubes has been optimized guided by visual characterization the next step is electrical characterization. For the electrical characterization the tubes are spread or grown on a highly p-doped Si substrate with thin SiO₂ cap layer. Electrical contact is made to individual tubes and to the p-doped Si substrate which is used to gate the device.

At room temperature the transport properties of the devices are measured as function of gate voltage. The methods used to produce and process the SWCNT's in this work, do not distinguish between metallic and semi-conducting tubes. 1/3 of the SWCNT's should thus be metallic and 2/3 semiconducting, as discussed in previous chapter (see Section 3.3).

At cryogenic temperatures quantum dot is normally formed in the SWCNT device. The linear response (conductance G as function of gate voltage (V_g) and grayscale measurements (differential conduction (dG/dV_{sd} , where V_{sd} is the source drain bias) as function of V_{sd}) and V_g) can give valuable information on the quality of the material as discussed in previous chapter (see Section 3.4)

4.2.2 Nanotubes from suspension solution

The nanotube material

Nanotubes from two producers were tested. Both materials came purified in suspension solution and had already been sonicated with ultrasound in order to separate the tubes. The material that were tested were:

- HiPCO tubes from *South Western NanoTechnologies – SWeNT*. The surfactant SDBS (Sodium dodecylbenzen sulfonate) was used to solve the material in water.
- Laser ablation material from University of Karlsruhe dissolved using SDS (Sodium Dodecyl Sulfonate) as surfactant.

The surfactants work like a soap. Their molecules have a polarized head that interacts with the water and long unpolarized tail that interacts with the nanotubes making it possible to dissolve the otherwise hydrophobic nanotube material in water[43]. Sonication helps separating the tubes, and the surfactant covers their surface when they are pulled from each other [44]. The SDBS is known to be very efficient in dissolving nanotubes in water [45].

The suspension solutions had already been purified and sonicated to separate the bundled tubes. It should be mentioned that the adhesion force acting between tubes is very strong. It has been estimated to be around $500 \text{ eV}/\mu\text{m}$ of tube's length [44].

Spreading the material directly

In the first test the nanotube material was spread directly from the suspension solution on an SiO_2 surface. The nanotubes where spread on the surface by spin coating. The sample was covered by suspension solution and the spun for 40 s at speed of 4000 rpm. Some of the nanotubes of the suspension anchor to the surface while the solution is spun off and it's remains dry on the surface. Some surfactant will also remain on the surface after spin coating. These surfactant residues make the surface pretty dirty looking when looked at in SEM and AFM. These remains are cleaned using methanol.

An AFM image of the laser ablation material from Karlsruhe, which was spread directly on the surface, is shown in Fig.4.2. The longest nanotube seen in this scan is $\sim 2 \mu\text{m}$ long. It can be seen that lot of tubes are branched which is, as said above, a clear indication of bundling. The length and the diameter of the tubes where measured in numerous AFM scans as shown in Fig.4.2. The diameter d is plotted as function of length l of 64 tubes is

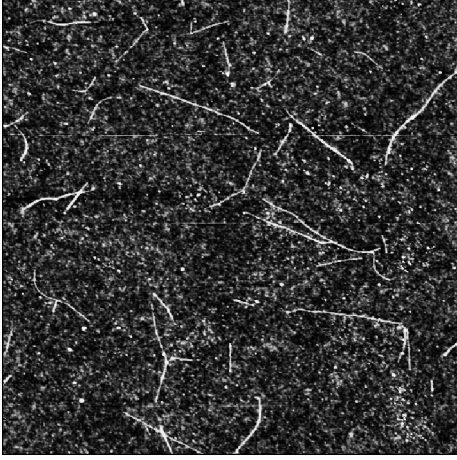


Figure 4.2: AFM picture of nanotubes which were spread directly from the solution on SiO_2 surface. The brighter areas are higher than the darker. The picture shows area of $5 \mu\text{m} \times 5 \mu\text{m}$

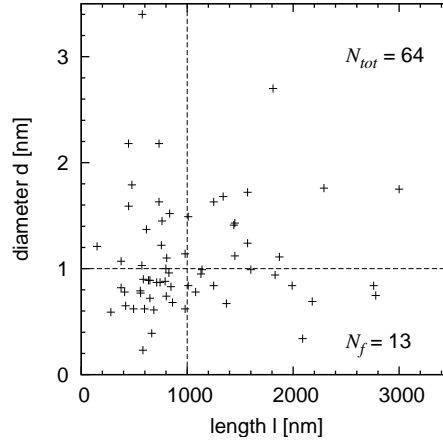


Figure 4.3: Diameter d plotted vs. length l for 64 nanotubes. d and l are uncorrelated. N_f is the number of feasible tubes i.e tubes with $l > 1000 \text{ nm}$ and $d < 1 \text{ nm}$.

shown in Fig.4.3. The correlation between l and d is 0.07, i.e. l and d are not correlated¹. The number of feasible tubes, i.e. tubes having $l > 1 \mu\text{m}$ and $d < 1 \text{ nm}$ is 13 or $\sim 20\%$. The density is a bit too high for making devices but ideal for making contacts blindly to the nanotubes.

The SWeNT material is however not suitable for making blind contacts. An SEM picture of SWeNT material, which was spread directly from the solution on a SiO_2 surface, is shown in Fig.4.4. This material looks like spaghetti and is clearly bundled. In order to use this material the solution has to be processed before spreading it.

The Karlsruhe material, which was spread directly from the solution was contacted blindly. That is done by spreading it on the standard wafer material which is highly p-doped Si with 400 nm SiO_2 cap layer. Electrodes are made blindly on the sample without looking at the surface, neither in an SEM nor in an AFM. The Electrical resistance between the electrodes is then checked in order to see if nanotube is in between. The highly doped

¹The correlation of data sets x and y , ρ_{xy} is defined as

$$\rho_{xy} = \frac{1}{\sigma_x \sigma_y N} \sum_i (x_i - \mu_x)(y_i - \mu_y),$$

where N is number of values, σ_x and σ_y are the standard deviation of x and y respectively and μ_x and μ_y their mean values. ρ_{xy} takes values between 1 for fully positive correlated data sets to -1 for fully negative correlated ones [46].

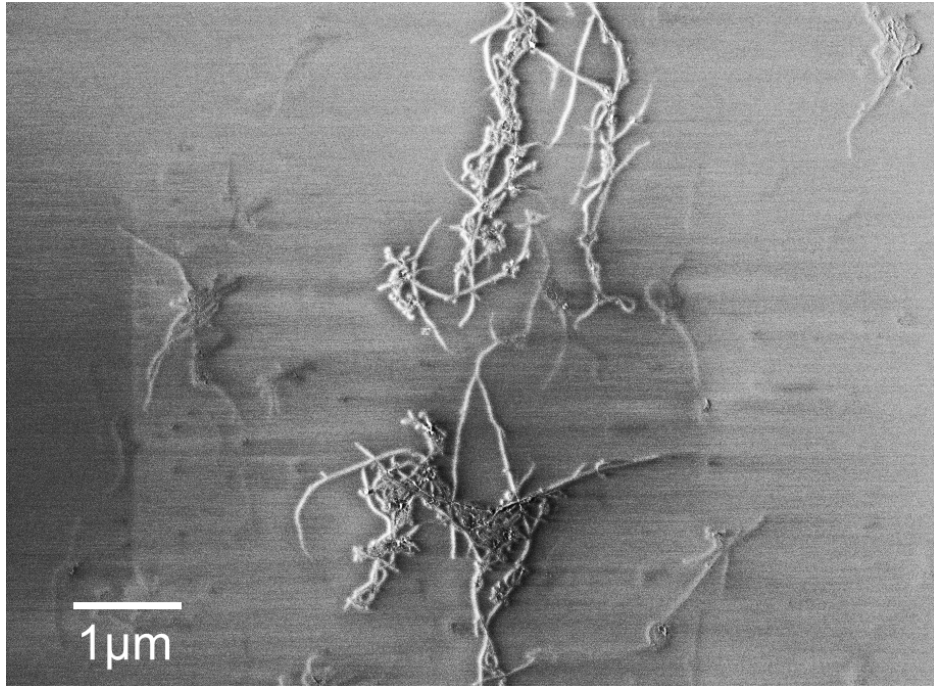


Figure 4.4: SEM picture of the HiPCO material spread directly from the solution on a SiO₂ surface. The nanotubes highly bundled

Si substrate can be used as a gate and by measuring the conductance G as function of applied gate voltage V_g one can check if the nanotubes are semiconducting or metallic. The gate dependences of two working devices are shown in Fig.4.5. The nanotube measured in Fig.4.5(a) is metallic. The resistance of the device is $R \sim 100 \text{ k}\Omega$ ($G/G_0 = 0.26$, where $G_0 = e^2/h$ is the conduction quantum) and does not practically change with gate voltage V_g .

The resistance of the other device is higher and it changes with V_g (see Fig.4.5(b)). It changes from $2 \text{ M}\Omega$ for $V_g = -10 \text{ V}$ to $4 \text{ M}\Omega$ for $V_g = 10 \text{ V}$. This device is most probably a rope containing both metal and semiconducting tubes. No devices made by blindly contacting the nanotubes were truly semiconducting, i.e. showing significant changes in the conductance. This can only mean that the nanotubes on the surface are bundled.

Diluting and sonicating the solution

From the initial characterization of the nanotube material it was concluded that the nanotubes, when spread directly on the surface, are not well sep-

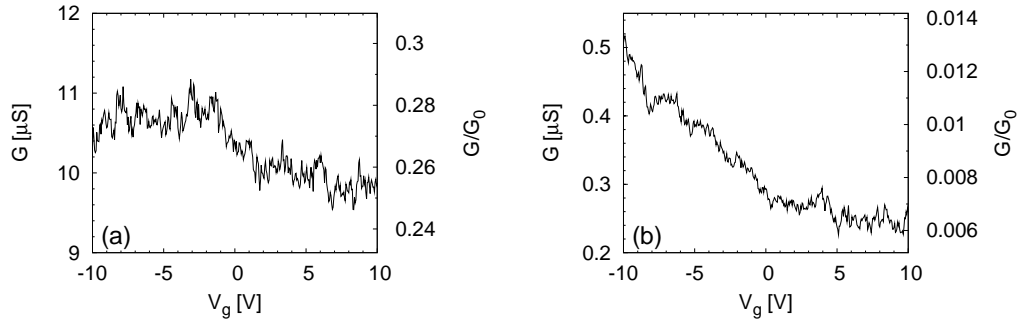


Figure 4.5: Conductance G of a blindly contacted Karlsruhe nanotube as function of applied gate voltage (V_g) at room temperature. The tube in (a) has a resistance of $\sim 100 \text{ k}\Omega$ and is metal conducting. The tube in (b) has resistance of $2 \text{ M}\Omega$ for $V_g = -10 \text{ V}$ to $4 \text{ M}\Omega$ for $V_g = 10 \text{ V}$. It is most probably a rope.

arated. It is not clear how well the nanotube material is separated in the suspension solution. Spectroscopy measurements done on suspension solution indicate that the tubes stay well separated in suspension for long time [45]. One can expect that the tube can bundle together in the process of spreading them on the surface. Diluting the solution should minimize the risk of bundling during spreading as well as lower the density of the tubes on the surface. The solutions were diluted with deionized water and the separation of nanotubes in them was improved by sonicating the diluted solution before spreading it to the surface. Some more surfactant (SDBS) was added to the solution before sonicating it to help with the separation.

First sonication experiments were done using normal table top sonicator (like can be found in all labs). The problem with such sonicators is that their power is relatively low and not well defined. The nanotubes first became sufficiently separated when high power sonicator was used. The sonicator used was Branson Digital Sonifier. Its maximal power is 400 W.

It is known that ultrasound brakes tubes. The tubes are most vulnerable where they have defects and it has been estimated that up to 5% of C atoms are localized at defects sites [47]. The tradeoff is, that with longer and more powerful sonication one gets better separated tubes but shorter.

Numerous methods have been suggested to optimize the separation process such as combination of short high power tip sonication and long sonication in normal table top sonication bath [48]. After playing around with the parameters of the sonication process the conclusion was the following recipe, where all the steps are done in the Digital Sonifier.

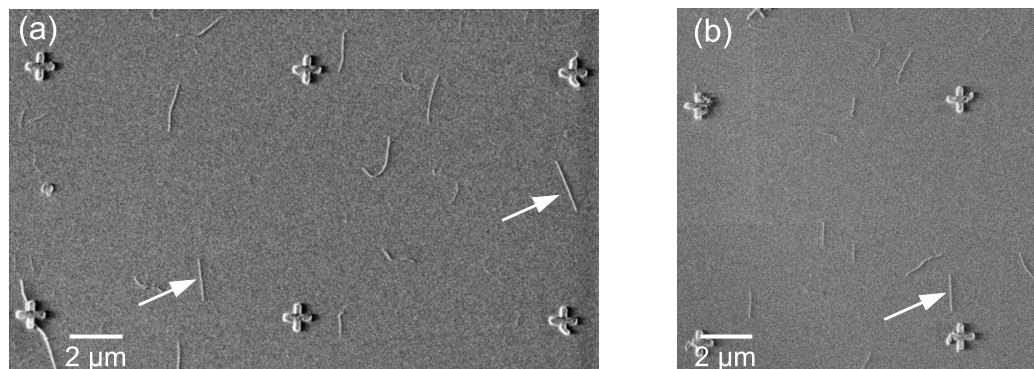


Figure 4.6: SEM figure of SWCNT that were spread on the surface after the suspension solution had been diluted and sonicated with high power sonicator. In (a) SWeNT material is shown and in (b) Karlsruhe material. The arrow point at tubes that look good for contacting.

200 W Continuously for 10 minues,
 200 W in 0.5 s pulses with 0.5 s intervals for 20 minutes
 40 W Continuously for 20 minues

The spreading procedure can also influence how well separated the tubes are on the surface. Instead of spinning the samples dry when they had been covered with processed solution they where blown dry with Nitrogen. The solution was left on the samples for 10 minutes before blowing them dry. The samples were then cleaned in methanol and deionized water to get rid of the surfactant residues.

The properties of the surface on which, the nanotubes are spread, do also influence how well they anchor to the surface and thus to what extent they will bundle together. It was tested to treat the surface using (3-Aminopropy)triethoxysilane (APTS) This treatment is supposed to enhance the adhesion of the nanotubes to the surface. No difference was found between APTS treated samples and other samples, except that the APTS samples looked dirtier in SEM.

An SEM image of nanotubes, which were spread from solution treated with the standard sonication recipe can be seen in Fig.4.6, in (a) SWeNT material is shown and in (b) Karlsruhe material. Not all tubes are good but one can most of the time find tubes suitable for contacting. Good tubes are marked with white arrow in Fig.4.6. Few tubes are longer than $1.5 \mu\text{m}$ which makes it difficult to use them for making electrical devices.

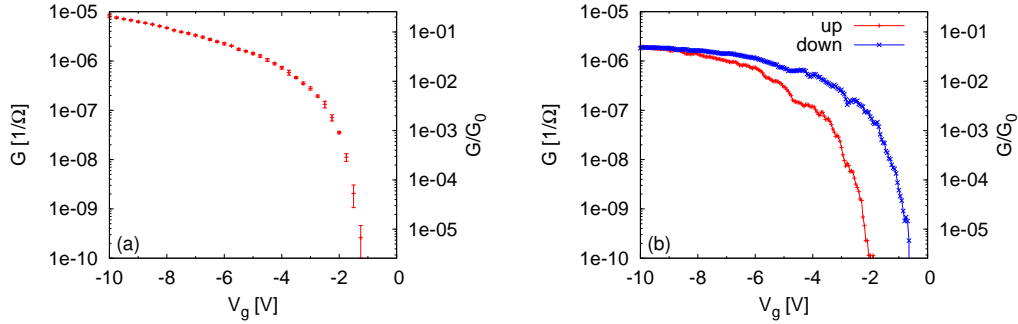


Figure 4.7: Gate response of two semiconducting nanotubes. A changes of four order of magnitude in the conductance (G) could be resolved in both devices while sweeping the gate voltage (V_g). (a) Gate response of SWeNT nanotube. (b) Gate response of a Karlsruhe nanotube. V_g was ramped subsequently up and down in (b). Both devices were not conducting when $V_g = 0$.

Electrical properties of connected tubes

When the spreading process had been optimized some tubes were connected to check their electrical properties. The material was spread on the standard wafer material (highly p-doped Si with 400 nm thick cap layer). The tubes where localized using the SEM and contacted using E-beam lithography as will be described in Section 4.3 with electrodes of Pd.

The yield of working devices is relatively poor. Out of 57 devices made, only 16 of them or 28% had any conductance through the tube. 9 of the working devices were semiconducting and 7 metallic, which is a clear indication that the separation of the nanotubes has been improved by diluting of the solution and the sonication treatment.

Working devices were normally high-Ohmic having resistance $R \geq 200$ kΩ ($G/G_0 \leq 0.13$) at room temperature. Conductance (G) was measured as function of gate voltage V_g at room temperature for the best devices. An example of such measurements can be seen in Fig.4.7. V_g was ramped subsequently up and down when measuring one of the devices (Fig.4.7(b)). The hysteresis of the subsequent sweeps was 1.5 V in G as function of V_g . This hysteresis is due charges, which are trapped in the vicinity of the nanotube and do thereby affect the gate potential [49]. Most of the traps are due to water molecules around the tube [50]. Another source of hysteresis are traps in the gate oxide, i.e. the cap layer of the wafer.

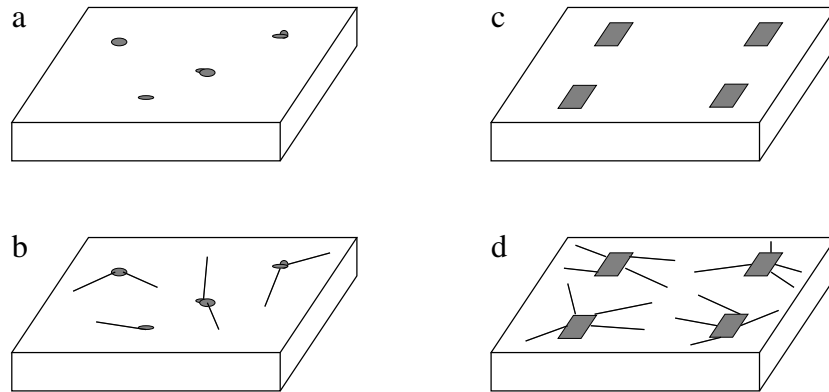


Figure 4.8: Two methods of spreading catalyst on the sample. In a the catalyst is spread evenly on the surface. The nanotubes then grow everywhere on the surface as shown in b. In c the catalyst is spread on predefined pads. The nanotubes then grow from the pads as shown in d.

4.2.3 Nanotubes grown by Chemical Vapor Deposition – CVD

CVD is a physicochemical process where hydrocarbon gases are used as carbon source. The gases are broken up in the presence of catalyst particles at high temperatures. Carbon nanotubes growth is nucleated at the particles and the tubes grow from them. The main advantage of the CVD is that the nanotubes are grown directly on the surface and one does not need to process the material any further. There are however many parameters that have to be optimized in the CVD process. More details on the CVD process, recipes and equipment can be found in Appendix A

The catalyst

There are mainly two ways of spreading the catalyst on the surface of the sample. The approach used in this work was to spread the catalyst particles evenly over the entire sample. The nanotubes then grow from the catalyst particles homogeneously over the sample. The other approach is to deposit the catalyst on predefined areas. The nanotubes then grow from these pads. Both methods are shown schematically in Fig.4.8. Using predefined catalyst pads or islands is useful when one uses AFM to localize nanotubes. A relatively small area in the vicinity of the pads needs to be scanned which is convenient because operating an AFM is very time consuming.

The composition of the catalyst is an important factor in the growing

process. In the lab's standard recipe three types of catalyst are used: Al_2O_3 4 nm nanopowder, $\text{Fe}(\text{NO}_3)_3$, and MoO_2Cl_2 . These catalysts components were dissolved in 2-propanol [13]. More information on the composition of the catalyst solution can be found in Appendix A.1

The catalyst solution was spread on the samples by spin coating. The catalyst particles form clusters on the surface of the sample from which the nanotubes grow. In Fig.4.9(a) an SEM image of such clusters and nanotubes, that have grown from them, are shown. The diameter of the nanotubes is dependent on the size of the catalyst particles. Thus, it is preferable to have these clusters small. Fewer tubes also grow from smaller catalyst island, which lowers the risk of having the tubes bundled. In order to separate the catalyst particles, the catalyst solution was sonicated with a high power sonicator ($P \approx 200$ W) for 15 min before spreading them on the surface. The size of the samples, which are covered by the catalyst particles were $\sim 1 \times 1$ cm. The samples were rotated at the speed of 4000 rpm and one drop of catalyst solution was put on it when it had reach full speed. This is a rough but reliable way of obtaining the optimal density of small catalyst particles on the surface of the samples.

The growing process

Three gases are used in the system; Argon (Ar) which serves as an inert gas the processing gases Hydrogen (H_2) and Methane (CH_4). CH_4 serves as a carbon source and the hydrogen is supposed to prevent deposition of amorphous carbon on the surface. The samples are heated up to growing temperature of $T = 950^\circ\text{C}$ in Ar flow. When the oven has stabilized at that temperature the processing gases where let though the furnace. First the H_2 flow is turned on, the Ar flow is stopped and finally the CH_4 flow was tuned on to start the growth. The growing time is 10 min and then the CH_4 flow is turned off and the Ar flow on. The Hydrogen is kept flowing when the oven is cooling down until it has reached temperatures of $T \leq 550^\circ\text{C}$. H_2 is supposed to clean the surface of amorphous carbon that may have be deposited during the methane flow. Further details on the cvd system and the growing recipe can be found in Appendix A.

The quality of the CVD material

Visual characterization is the simplest way of checking the quality of the CVD grown material. Four examples of CVD grown nanotubes, imaged using SEM, are shown in Fig.4.9. A catalyst cluster and nanotubes that have grown from them can be seen in Fig.4.9(a). These catalyst clusters are

relatively big and the tubes grow from them as ropes. The catalyst clusters are no longer visible Fig.4.9(b) because the catalyst was sonicated at high power before spreading it. The density is far too high and part of the tubes seem to glow. The “glowing” tubes are interconnected and this network has most probably electrical contact to metal structures (the big pad structure) in the vicinity. Such nanotube networks have been used for sensing experiments (see e.g. [51]).

Two examples of a good growth are shown in Fig.4.9(c) and (d). In Fig.4.9(c) a 12 μm long more or less straight tube can be seen. The tube is totally straight for at least 8 μm making it ideal for device fabrication. Above this straight tube one can see a slalom shaped tube that most probably is a rope. Another good tube can be seen in Fig.4.9(d). On both of these tubes one can see a kink (pointed at). This kink is often seen in straight tubes, normally near the end.

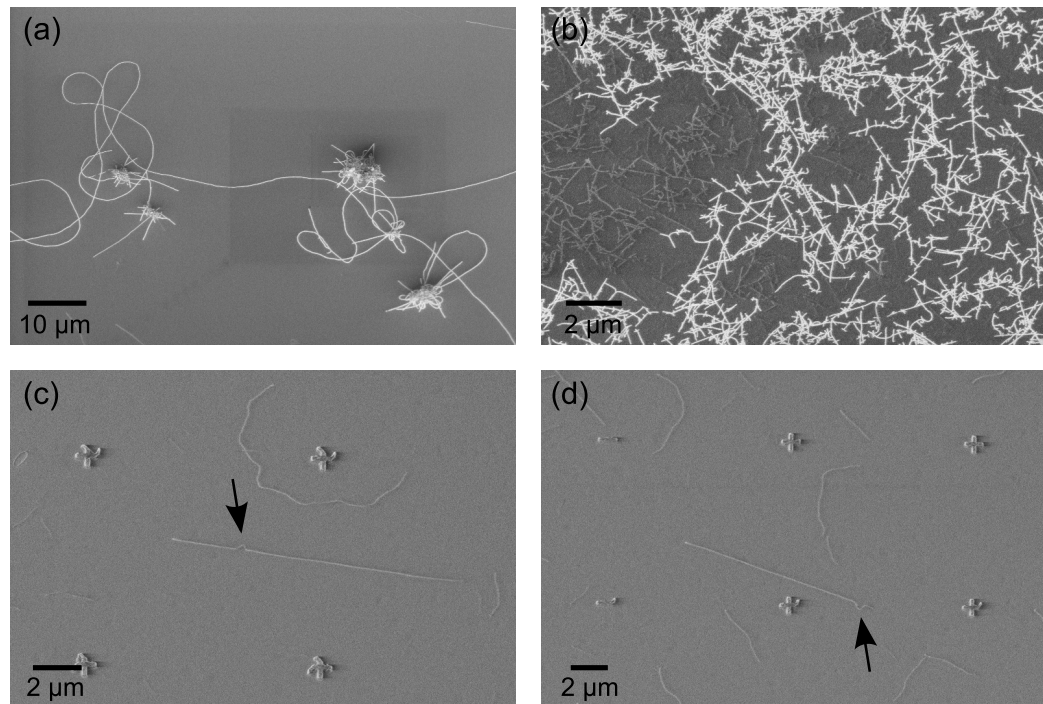


Figure 4.9: SEM picture of CVD grown nanotubes. (a) Big catalyst clusters and nanotubes that have grown from them. (b) Beautiful but useless for this work. Too densely grown tubes. The “glowing” tubes are interconnected. (c)-(d) two examples of successful growth. The density of the tubes is optimal and one can find feasible tubes to contact.

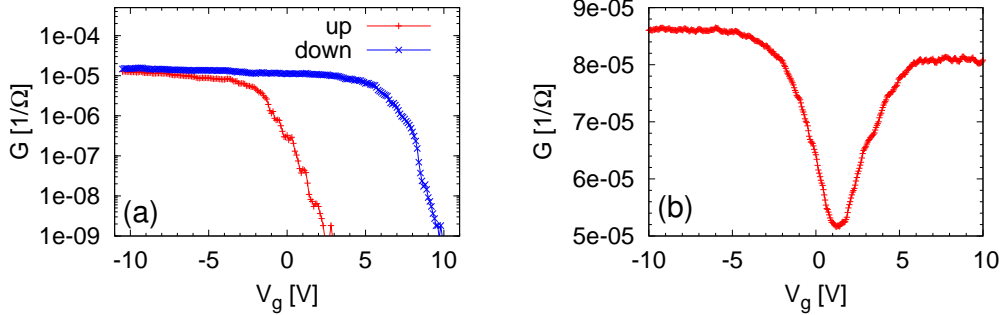


Figure 4.10: Conductance (G) measured at room temperature as function of gate voltage (V_g) in two CVD grown nanotube devices. In (a) a typical curve for semiconducting device is shown. G changes more than four orders of magnitude with V_g . In (b) the device is a short bandgap tube. Both devices are positive doped.

Electrical properties of the CVD material

The electrical properties of the nanotubes are probably the best way to control their quality. SWCNT were grown in the standard wafer (highly p-doped Si with 400 nm thick SiO_2 cap layer). Promising looking tubes were localized and contacted using E-beam lithography (as will be described in Section 4.3). The yield of working devices is much higher for the CVD grown tubes than for the tubes from the suspension solution. More than 50% devices work and their resistance are lower than of the suspension tubes.

The conductance (G) of two CVD devices, measured as a function of gate voltage (V_g) at room temperature is plotted in Fig.4.10. The device in Fig.4.10(a) is clearly semi conducting. The two curves shown are when V_g was ramped subsequently up and down. The hysteresis in G as function of V_g is ~ 7 V when sweeping between ± 10 V. As mentioned in Section 4.2.2 the hysteresis is due to charges trapped on and around the nanotube.

The curve shown in Fig.4.10(c) is typical for so called small band gap nanotubes. A dip appears in G when $V_g \approx 1.3$ V, i.e. when the Fermi energy is in the small bandgap. It is noteworthy that all CVD devices are hole doped, i.e. the dip in G in short bandgap tubes and the pinchoff in the semiconducting ones are at positive V_g . The working semiconducting devices made from the nanotubes obtained from suspension solution, however had all pinchoff at negative V_g .

Better insight in the quality of the nanotube material can be obtained by measuring their properties at cryogenic temperatures. In Fig.4.11 a grayscale measurement of a metallic nanotube measured at 1.9 K is shown. The dif-

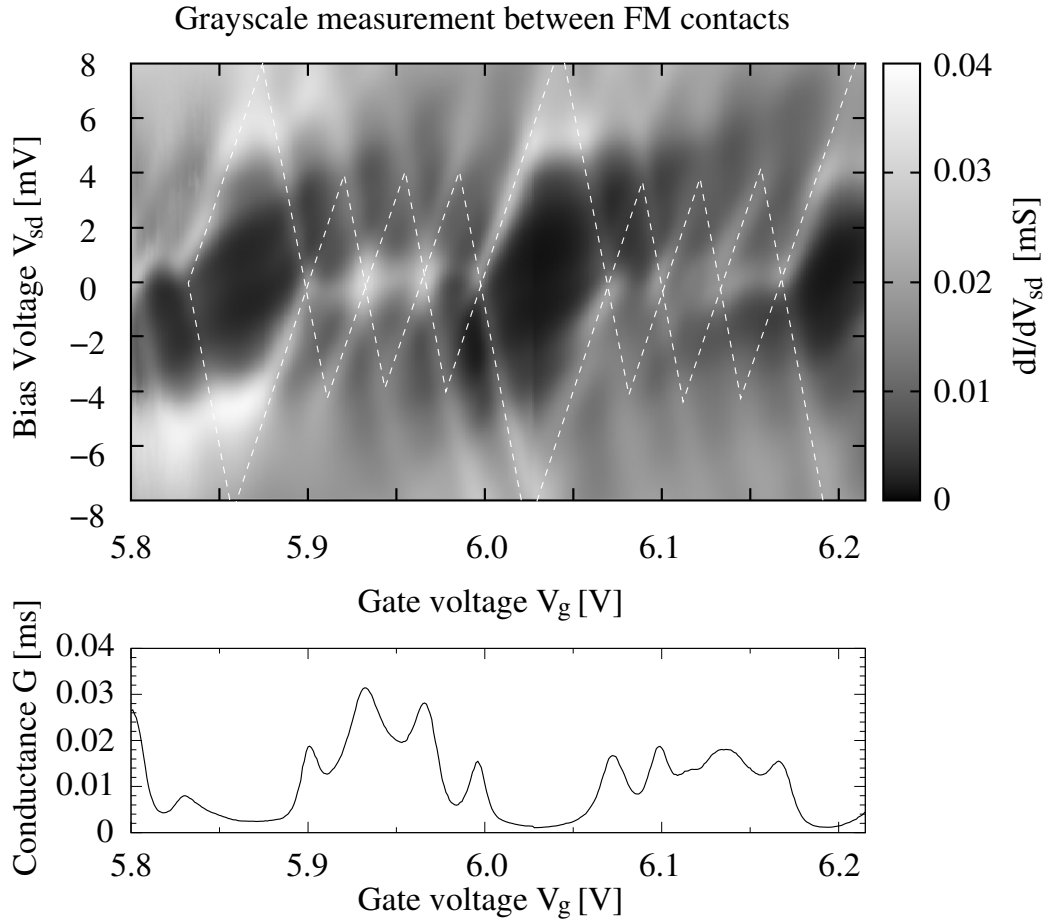


Figure 4.11: Fourfold symmetry in SWCNT quantum dot. A Metallic tube was connected with PdNi electrodes. The upper part shows a grayscale plot (differential conductance vs. gate voltage (V_g) and bias voltage (V_{sd})). The lower part show the linear response ($V_{sd} = 0$) in the same interval. The fourfold pattern of one big Coulomb diamond and subsequent three small diamond can clearly be seen.

ferential conductance (dG/dV_{sd}) is measured as function of bias bias voltage (V_{sd}) and gate voltage (V_g). The linear response (the differential conductance for $V_{sd} = 0$ is also shown). A four fold symmetry can clearly be seen in this measurement, which is, as discussed in Chapter 3, the hallmark of good metallic individual SWCNT. Such a four fold symmetry has been seen in numerous samples, which is a clear indication of a good quality of the CVD grown material.

4.2.4 Which material to choose

The CVD material is better suited for making electrical devices than material spread from suspension solution. The CVD tubes are longer, the success rate, when contacting them, is much higher, and the resistance of the devices is generally lower. The high resistance of the suspension tubes could be due to the surfactant that is sitting in between the tubes and the metal electrodes. HiPCO and laser ablation nanotubes do also have very small diameter that could make it more difficult to contact them.

After the growing parameters had been optimized the CVD procedure was relatively reliable way of obtaining “the wonder material”². This optimization was however not a straight forward task and any changes to the system, even minor changes such as changing gas bottle, can cause problems in the growing process.

4.3 Making of a SWCNT devices

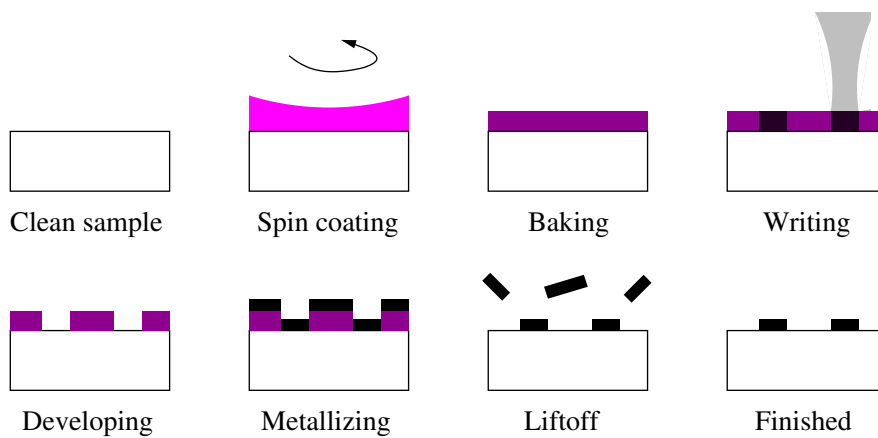


Figure 4.12: Electron beam lithography shown schematically. The cleaned sample is covered by PMMA solution by spinning it on. The sample is baked to harden the PMMA. The pattern is written into the PMMA layer by electron beam. The sample is developed and the exposed PMMA is dissolved. The sample is covered by metallic film. Liftoff: The sample is bathed in acetone and the metal that was deposited on PMMA is washed off.

²The optimization of the CVD growing process was mainly done by Jürg Furer, Dino Keller and Soufiane Ifadir

In order to make Single Wall Carbon Nanotube (SWCNT) one needs nanotubes of the right density and quality on the surface of the sample. It is described in Section 4.2 how to get that material and that is done by Chemical Vapour Deposition (CVD). The nanotubes are grown on a 1×1 cm piece of our standard wafer material, which is a highly p-doped Si with a 400 nm thick oxide layer on top. The density of tubes should be such that one can easily find suitable tubes and contact them individually without having unwanted shorts due to other tubes in the vicinity.

The samples are processed by means of standard Electron beam (E-beam) lithography. The E-beam lithography process, which is shown schematically in Fig.4.12 is done in following steps. The sample is cleaned carefully and covered with PMMA layer. A PMMA solution thinned with chlorobenzene is spun on the surface at the speed of 4000 rpm. In order to get rid of the solvents from the PMMA layer and harden it, the sample is baked for ~ 30 min at $\sim 175^\circ\text{C}$. The thickness of the PMMA layer after baking was 450 – 500 nm. The wanted pattern is written into the resist using electron beam. That is done in LEO Supra 35 scanning electron beam microscope and the process is controlled using Elphy Raith software. The sample is developed by soaking it in MIBK thinned with isopropanol (1:3) for 60 s. The PMMA film is dissolved where it was exposed by the electron beam. The sample is metallized in evaporation chamber equipped with electron gun to heat the target. During metal deposition the samples were cooled below 0°C . Normally the base pressure of evaporation is around 1×10^{-6} mbar, which is low enough for making cruder structures. It is possible to reach pressures of the order of 1×10^{-8} mbar. That is done by pumping longer and by so-called Meissner cooling, when the inner walls of the chamber are cooled with liquid nitrogen. Titanium is finally melted shortly before metallizing the sample. The minimal evaporation pressure reached with this system is $\sim 4 \times 10^{-8}$. In this work such a low pressure was only necessary when evaporating ferromagnetic metals, where oxidation is of great concern. After metallization, the final liftoff process is made, where the samples are treated in acetone. The PMMA is dissolved and the metal film that was deposited on the PMMA is washed away.

The samples were made using three steps of E-beam lithography. In first step the connection pads, the big pads, and markers were made. In second step normal contacts to the SWCNT's and leads were made. When making more complicated devices such as spin valves or hybrid devices with different types of contacts materials, the third lithography step is needed. Making of more complicated devices can sometimes also be solved using shadow evaporation technique, but that was not used in this work. The processing steps of the samples are shown in Fig.4.13.

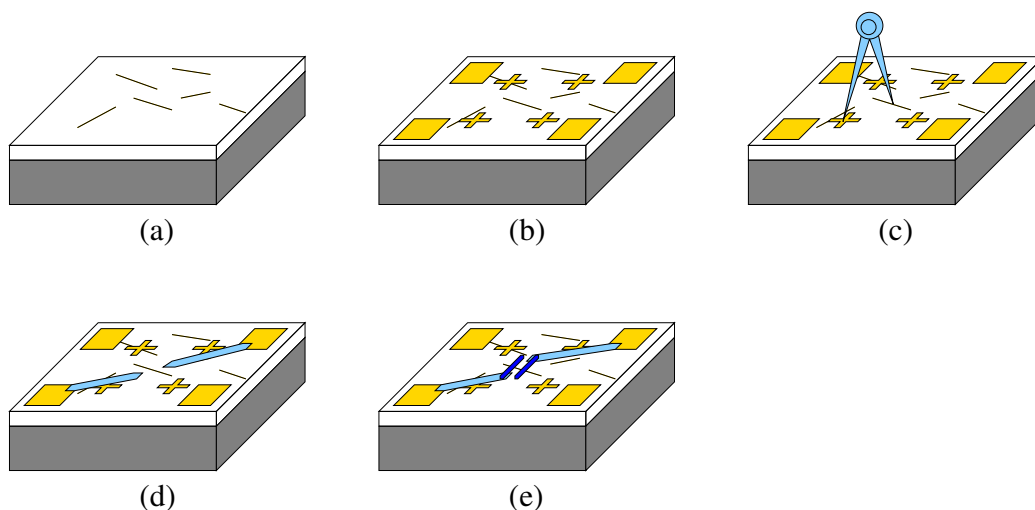


Figure 4.13: The processing of spin valves shown schematically. (a) Nanotubes on the wafer material. (b) contact pads (squares) and markers defining a coordinate system made by E-beam lithography. (c) feasible nanotube localized in the coordinate system. (d) lead from the big pads to the nanotube and normal contacts made. (e) Electrodes of other material, such as ferromagnetic metals, made on to the nanotube.

4.3.1 Big pads and markers

The shape of the big pads is shown in Fig.4.14(a). The size of the bigpad pattern is 2 mm and it's orientation can be seen with naked eyes, which is important for later processing steps. The contacting area (See Fig.4.14(b)) has markers that make up a coded pattern, which defines a coordinate system. This pattern is essential when suitable SWCNT's are localized and in finding the again in later processing steps.

The Bigpads and the markers which are usually made in the same lithography step, are normally made up of three layers: First comes 10 nm thick SiO_2 layer, which is supposed to isolate the bigpads from the nanotubes on the surface and thus prevent shorts. Next comes 40 nm thick layer of Ti for mechanical stability of the bigpads and finally a 50 nm thick gold layer.

The total thickness of the bigpad and the markers is 100 nm. Such a thick markers can make it difficult to localize the nanotubes using Atomic Force Microscopy (AFM). If AFM is to be used to localize the nanotubes one can either make thinner markers in another lithography step, which is quite time consuming, or make the big pads and the markers thinner, hoping that no tubes will short the bigpadstructure. It has been tested to use 40 nm thick Pd for markers and big pads. Pd makes smooth films when evaporated and

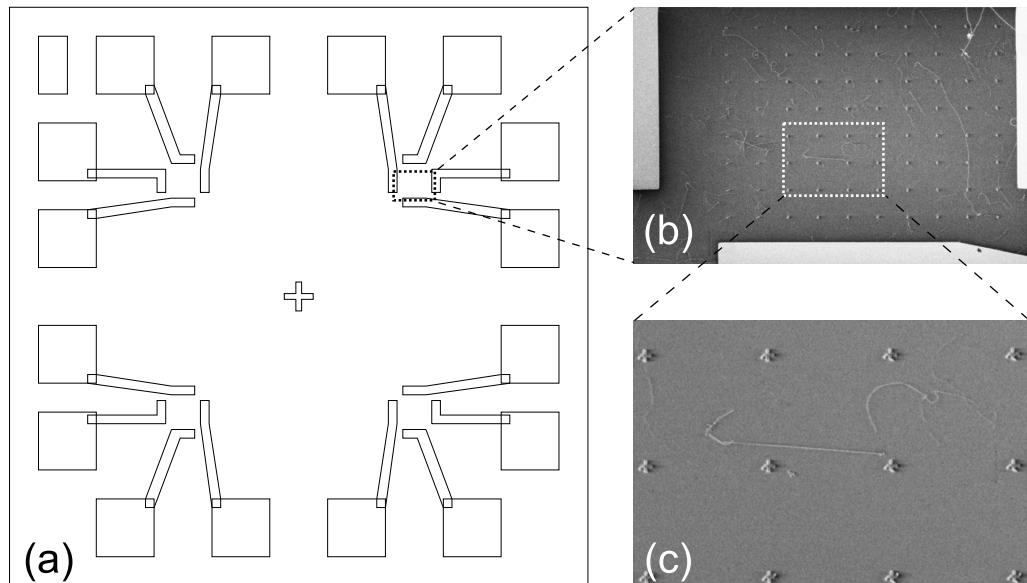


Figure 4.14: (a) Schematics of the bigpads. The structure is 2 mm in diameter and has four devices. (b) SEM image of one of the devices, the markers can be seen. (c) Zoomed in to a Nanotube. It is localized in the marker coordinate system.

such a layer is dense enough to be visible with SEM through a 500 nm thick PMMA layer.

4.3.2 Localizing suitable nanotubes for contacting

The tubes were localized according to the coordinate system set up by the markers (see Fig.4.14(b) and (c)). That can be done by using either an SEM or AFM. As discussed in Section 4.2.1 using SEM is much quicker than using AFM and one can see all tubes with the SEM. By using SEM one can easily make an overview of the whole contacting area and zoom in to make a more accurate picture to localize the tube.

The maneuverability of the AFM is much more limited but as, discussed in Section 4.2.1 the advantage, that it is possible to measure the height of the tubes, i.e. their diameter, which is an important parameter when estimating if the tube is an individual one or a rope of many tubes. The main advantage of AFM is the high resolution and it is not believed to have minimal effects on the tubes.

The main problem of using SEM for localizing tube is that one does not exactly know, which effect the SEM has on the nanotubes. Long exposure

with electron beam changes the material. One can see that clearly when imaging nanotubes with SEM. Amorphous carbon is deposited on the surface and the structure of the nanotubes can be changed. It is not fully known, how significant the effects a short exposure, like what was needed to make the snapshots shown in Fig.4.14(b) and (c), is. We tried to compare nanotubes that had been localized either by AFM or SEM. The tubes were grown in the same growing process to avoid run to run variation. This comparison was not conclusive, but it seemed that there was no significant difference³.

SEM was used to localize the nanotubes for the devices of this work. It was concluded that the quality of the nanotube material could be determined good enough by the shape of the tubes. The importance of the diameter information, which one can get from the AFM measurements, were not considered to be worth the time invested in doing the AFM imaging. The exposure time was kept at minimum to minimize damage to the nanotubes from the electron beam and straight tubes were searched in the contacting area. The fact that the four fold symmetry can be seen in numerous SWCNT devices where SEM had been used to localize the nanotubes is a clear indication that the SEM localization does not destroy the unique electronic properties of SWCNT's.

4.3.3 Making the contacts

Two lithography steps were used to make ferromagnetic contacts to the nanotubes in this work. First leads of normal metal from the bigpad to the nanotubes are made (see Fig.4.13 (d)). The leads are made of 40 nm thick Pd. Palladium is known to make good films and good contact to nanotubes both metallic and semiconducting [52, 53]. The bigpad structure is ~ 100 nm high and the 40 nm thick Palladium film bridges this height difference easily. When only normal contacts are made to the nanotubes it is done in this one step.

In the second lithography step the FM contacts are made (see Fig.4.13 (e)). The ferromagnetic material normally used is Pd_{0.3}Ni_{0.7}. Other FM materials have also been tried and combination of different FM layers. The FM materials will be discussed further in Chapter 5. The FM layer(s) is usually covered by 10 nm thick Pd cap layer to prevent oxidation.

The sample is now ready for measurements. It is glued on a standard chip carrier and when doing that it is good to be able to see the orientation of the sample with naked eyes. The samples are bonded using KS 4523 Digital

³These experiments were done in a blockcourse on Carbon nanotube. Markus Weiss and I taught in this block course.

bonder to contact the bigpads to the chip carrier with an Al wire. The Back gate is contacted by scratching through the SiO_2 cap layer of the wafer near one corner of the sample and covering the scratch with silverpaste. The silver paste is smeared over the edge of the sample in order to ensure good contact to the highly doped Si substrate. Finally the silver paste is contacted by bonding on it.

Chapter 5

Measurements on SWCNT spin-valves

5.1 The basic idea

Single wall carbon nanotubes (SWCNTs) are an interesting material for spintronics, because they are quasi one-dimensional electron systems and the spin coherence length is believed to be long in them. The reason for this long spin coherence length is low spin-orbit coupling in carbon and that the main isotope of carbon, ^{12}C , which makes up $\sim 99\%$ of natural carbon has no nuclear spin [54, 55].

In Fig.5.1 a SWCNT spin valve is shown schematically. A SWCNT is contacted by two ferromagnetic (F) electrodes. In between the electrodes a quantum dot is formed within the SWCNT. The electrostatic energy of the dot can be tuned by using a gate, which is in Fig.5.1 depicted as a side gate but normally back gates are used. The shape of the electrodes should define their easy axis of magnetization and their coercive field (H_c). If the F material is magnetically soft the easy axis should be along the elongated structure. The coercive field should also be dependent on the shape of the electrodes and different shape should give different coercive fields ($H_{c1} \neq H_{c2}$).

By applying a magnetic field along the electrodes one should be able to switch the magnetization from parallel to antiparallel mutual orientation, and thus measure R_P and R_A (the parallel and antiparallel resistances) and calculate the TMR

$$TMR = \frac{R_A - R_P}{R_P}. \quad (5.1)$$

The resistance (R) as function of applied magnetic field (H) of an ideal device is sketched in Fig.5.1.

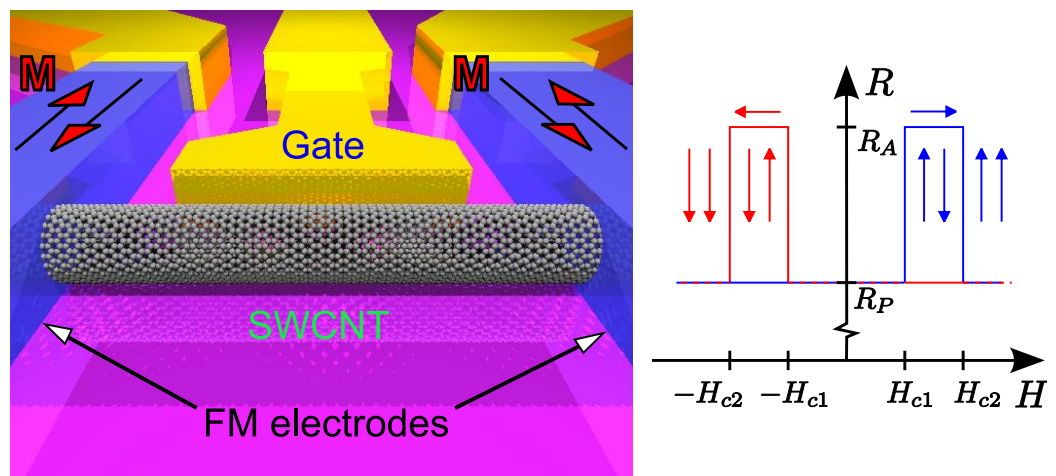


Figure 5.1: SWCNT spin device and TMR curves shown schematically. SWCNT is connected by two F electrodes. A quantum dot is formed within the SWCNT in between the electrodes, which can be tuned by a gate (here depicted as side gate). The shape of the electrodes define the easy axis of magnetization and their coercive fields (H_{c1} and H_{c2}). To the left the resistance of the device (R) as function of magnetic field (H) applied along the F electrodes is sketched. When the field is ramped up and down, R changes due to the electrodes switching between parallel and antiparallel magnetizations.

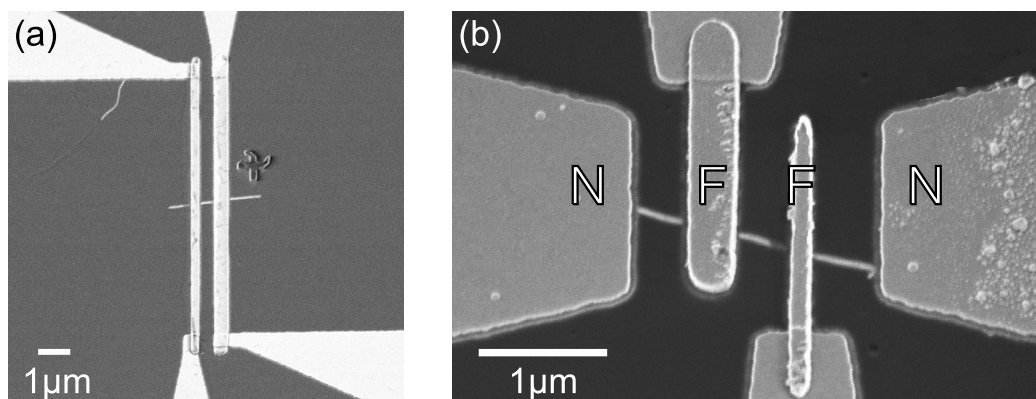


Figure 5.2: SEM pictures of two types of CNT spin devices. (a) a two terminal device. The SWCNT is connected by 10 μm long electrodes that are connected on both ends. One can monitor the magnetic switching of the electrode using anisotropic magneto resistance (AMR). (b) A four terminal device. The nanotube is contacted by two normal (N) electrodes and two ferromagnetic (F) electrodes.

5.2 Spin-valve devices

The devices were made as described in the previous chapter. SWCNTs were grown on a highly doped Si wafer with a 400 nm thick SiO_2 cap layer and contacted using E-beam lithography. The samples were glued on a standard chip carrier, bonded and contact made to the highly doped, Si which was used as a back-gate.

Mainly two types of devices have been made, a normal spin-valve device where the nanotube is contacted by two F electrodes. An SEM image of the spin-valve device is shown in Fig.5.2(a). The F electrodes are 10 μm long and 200 nm and 400 nm wide, with contacts on both ends. This makes it possible to measure the resistance of the electrodes as a function of magnetic field and thus monitor how their magnetization switches using anisotropic magnetoresistance (AMR) described in Chapter 2.

The other type of device was a four terminal device, of which an SEM image can be seen in Fig.5.2(b). The nanotube is connected by two normal (N) electrodes on the ends and two F electrodes between the N electrodes. This type of device can be used on the one hand for normal spin valve measurements and on the other hand for control measurements where the conductance between adjacent N and F electrodes is measured while sweeping the magnetic field. Furthermore it is possible to do non-local measurements in this devices, as will be described in Chapter 6.

5.3 Ferromagnetic Contact materials

5.3.1 The ideal contact material

The ideal contact material for making SWCNT based spin devices has to fulfill two conditions. It has to make a good contact to SWCNTs and it has to have the appropriate magnetic properties.

Ever since the discovery of carbon nanotubes one of the major issues in their characterization was the contacting with metal electrodes. There are relatively few metals that make a contact to SWCNT. In earlier experiment with SWCNT they were contacted using metals with high work function such as Pt and Au [56]. Later, it was discovered that Pd makes good contact to both metallic and semiconducting SWCNT [52, 53].

The magnetic contact material should be a soft magnet in order to be able to control the easy axis of magnetization and the coercive field by the shape of the electrodes. Additionally the spin polarization of conduction electrons must be high enough to obtain a measurable TMR signal. An electrode of a single magnetic domain would be the ideal electrode, since moving domain walls in the contact region with the SWCNT can introduce additional complication to the device.

5.3.2 PdNi alloy

There are indeed very few materials that have the wanted properties described above. In previous works done in the group, PdNi alloy has been used as F contact material in the composition $\text{Pd}_{0.3}\text{Ni}_{0.7}$ [11, 12, 14]. The idea is to combine the ferromagnetic properties of Ni with the contacting properties of Pd. The magnetic moment of the $\text{Pd}_x\text{Ni}_{1-x}$ (m_{PdNi}) is plotted as function of x in Fig.5.3. The m_{PdNi} is relatively high for concentration of Pd up to $\sim 50\%$ and for 30% Pd concentration, as was used in the CNT spin-valves, the m_{PdNi} is more than 95% of the pure Ni value [57]. The spin polarization of the $\text{Pd}_{0.3}\text{Ni}_{0.7}$ alloy was estimated to be $\sim 10\%$ [12], which according to Jullière's model would yield TMR signal of $\sim 1.9\%$ [18]

The $\text{Pd}_{0.3}\text{Ni}_{0.7}$ alloy makes a stable contact to SWCNTs. The grayscale measurement shown in Fig.4.11 is from a sample that was contacted with $\text{Pd}_{0.3}\text{Ni}_{0.7}$. The tube was metallic and one can clearly see the four fold symmetry, which is, as discussed in section3.4, the hallmark of good metallic tubes.

The magnetic properties of PdNi alloy are however not optimal. Variety of the switching behavior in previous work points to the conclusion that the PdNi electrodes are multidomain. For different gate voltages curves switch-

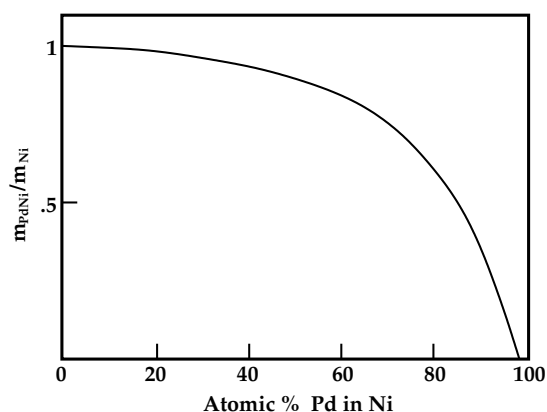


Figure 5.3: Magnetic moment of $\text{Pd}_x\text{Ni}_{1-x}$ alloy scaled with the magnetization of pure Ni ($m_{\text{PdNi}}/m_{\text{Ni}}$) as function of Pd concentration (x). When $x \approx 0.3$ the m_{PdNi} is almost the same as for pure Ni $m_{\text{PdNi}}/m_{\text{Ni}} > 95\%$. (Adapted from [57].)

ing varied with gate voltage from nice step like switching to triangular forms as one should see due to magneto coulomb effect in quatnum dots connected by ferromagnetic leads [15]. It was also noted that there was no qualitative difference, when applying the magnetic field in plane, if it is parallel or perpendicular to the electrodes [12].

In order to study the magnetic properties of the PdNi further the magnetization of a control sample was measured using vibrating sample magnetometry (VSM)¹. The control sample is from the same wafer material as used in the sample fabrication (highly p-doped Si with 400 nm thick SiO_2 cap layer). Its size is 5×5 mm and it was placed into the evaporation chamber when evaporating on the spin-valve samples. The magnetization was measured at a temperature of 5 K applying the field both in and out of the plane of the film. The magnetization of the film (M) as function of applied magnetic field (H) is plotted for both orientations in Fig.5.4.

The easy axis of the magnetization is not well defined. Hysteresis curves are measured for both directions of applied field and they look complicated, especially with the field applied out of plane. From the two measurements it looks like the easy axis is even more out of plane than in plane of the film.

In this context it is interesting to compare spin-valve measurements of PdNi device when applying the field in and out of plane of the samples. This is shown in Fig.5.5. In Fig.5.5(a) the field is applied in plane of the sample. The measurements were done at a temperature of $T = 1.85$ K and the resistance was 41 k Ω at high fields, when the magnetization of both electrodes are parallel (R_P)². The resistance for antiparallel magnetization of the electrodes (R_A) is 39 k Ω , which gives TMR signal of -4.9% . The R_A

¹The VSM measurements were done in the group of Dr. Christoph Sürgers at the University of Karlsruhe.

²It is assumed that the magnetization of both electrodes is parallel at fields higher than 200 mT

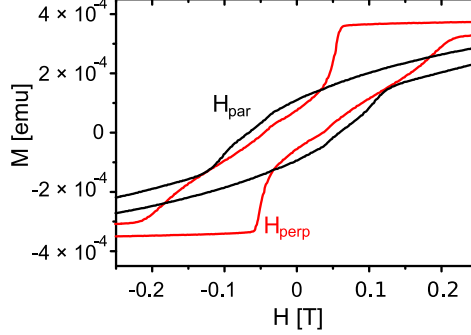


Figure 5.4: Magnetic properties of PdNi/Pd film. The magnetization of the film measured with VSM with field applied in-plane of the sample (black) and perpendicular to it (red).

was taken as the mean value of the resistances in the switching minimum for each sweeping direction. The spin polarization, estimated from the TMR value is according to Jullière's model 15% [18].

Comparing the switching to the ideal switching shown in Fig.5.1 we see that in the case of PdNi electrodes the switching is much more complicated. Some pre switching can be seen, i.e. it looks like the magnetization of the electrodes start to change before the field is ramped through zero. The main switchings however take place when the field has been ramped through zero. Even though these main switching events are not totally clear (like shown in Fig.5.1), these data indicate that the easy axis of magnetization is partly in plane of the sample.

In Fig.5.5(b) H is applied out of the sample's plane. The switching behavior in this case is much more complicated, and it looks like there are multiple switchings taking place. The signal can be described as a strong background in the range $|H| < 300$ mT, with a maximum at $H = 0$. On this background signatures of multiple switching events can be seen. If the easy axis of the F electrodes were in-plane of the sample there should be negligible difference in the up swept and down sweep curves. The magnetizations (\mathbf{M}) of the electrodes should rotate gradually from an easy orientation in the plane of the sample and align with \mathbf{H} when H increases.

To estimate the shape of the R curve as function of H when it is applied out of plane of the sample, we need to know how \mathbf{M} rotates as function of H . This situation is shown schematically in Fig.5.6(a). It is assumed that the easy axis of magnetization is along the electrode. The energy of the

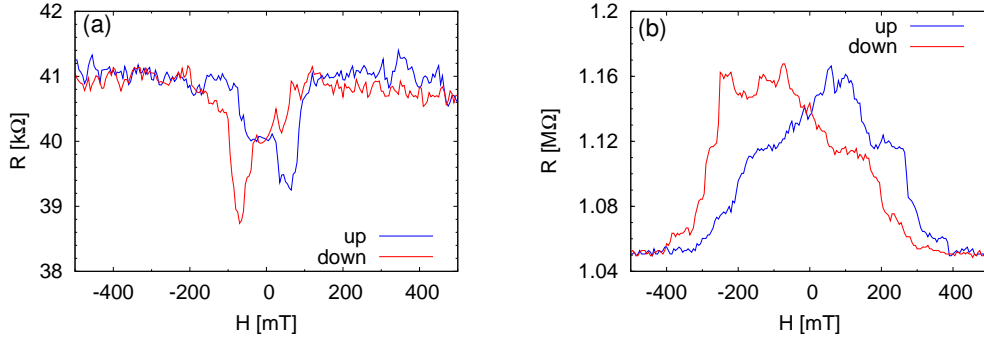


Figure 5.5: Spin-valve measurements where PdNi is used as a ferromagnet as contact material. (a) The field is applied in plane of the sample. (b) Field applied out of plane of the sample.

Magnetization is then given by

$$\begin{aligned} E_M &= -\mathbf{M} \cdot \mathbf{H} - K \cos^2 \theta \\ &= -MH \sin \theta - K \cos^2 \theta, \end{aligned} \quad (5.2)$$

where K is the magnetic anisotropy of the electrode [20]. Minimizing this energy by setting $\partial E_M / \partial \theta = 0$ gives the orientation of \mathbf{M} as function of H , i.e. $\theta(H)$.

$$\theta(H) = \begin{cases} -\pi/2 & \text{if } MH < -K \\ \arcsin\left(\frac{MH}{K}\right) & \text{if } -K \leq MH \leq K \\ \pi/2 & \text{if } MH > K \end{cases} \quad (5.3)$$

At zero field the magnetization of the electrodes are assumed to be antiparallel. Due to the field from the electrodes this orientation is lower in energy than the parallel one. When H is applied perpendicular to the plane of the sample the magnetizations of the electrodes rotate from the antiparallel orientations (see Fig.5.6(b) and (c)) until the magnetizations are parallel aligned with \mathbf{H} .

The conductance of the device as a function of the angle between the magnetizations of the electrodes (ϕ) is given by [35]:

$$G(\phi) = G_P + G_\Delta \sin^2(\phi/2), \quad (5.4)$$

where $G_\Delta = G_A - G_P$. Lets assume that the anisotropy energy (K) of the electrodes are the same. From Fig.5.6 and Eq.(5.3) it can be seen that $\phi = \pi - 2 \arcsin(MH/K)$ if $|MH| < K$, but 0 otherwise. By substituting that

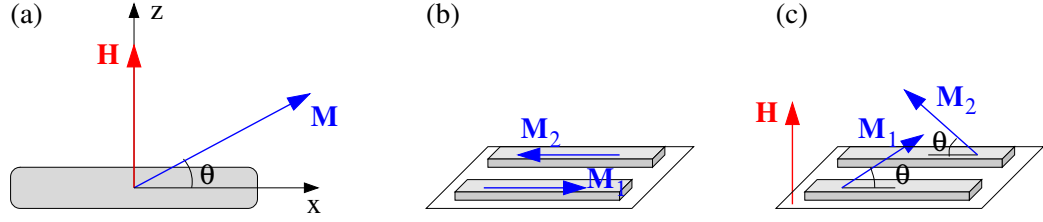


Figure 5.6: (a) An electrode with easy axis of magnetization along x -axis. When magnetic field (\mathbf{H}) is applied perpendicular to it the Magnetization (\mathbf{M}) rotates. (b) Electrodes that are magnetized in opposite direction at zero field. (c) \mathbf{H} applied out of plane of the sample. The magnetization of each electrode (\mathbf{M}_1 and \mathbf{M}_2) rotates out of plane.

into Eq.(5.4) the conduction as function of applied field $G(H)$ is obtained:

$$G(H) = \begin{cases} G_P & \text{if } |MH| > K \\ G_P + G_\Delta \left[1 - \left(\frac{MH}{K} \right)^2 \right] & \text{if } |MH| \leq K \end{cases} \quad (5.5)$$

The shape of G as function of H is parabolic according to Eq.(5.5). The resistance (R) as function of H is given by

$$R(H) = \begin{cases} R_P & \text{if } |MH| > K \\ \frac{R_P R_A}{R_A - (R_P - R_A) \left[1 - \left(\frac{MH}{K} \right)^2 \right]} & \text{if } |MH| \leq K \end{cases} \quad (5.6)$$

R as function of H has Lorentzian shape according to Eq.(5.6). When $\Delta R = R_A - R_P$ is small it is in a good approximation parabolic. The background in the measurements in Fig.5.4(b), when the field is applied out of plane of the sample is in the first approximation parabolic. In Fig.5.7 The R as function of H is fitted using Eq.(5.6) using data from two measurements. The measurements were done at two different values of V_g giving very different resistances. In both cases the parabola ends at the applied field of ± 300 mT.

A Lorentzian R as function of H is something that one expects for the field applied out of plane of the sample, if the easy axis is in plane. The other parts of the signal plotted in Fig.5.5, i.e. the difference between the curves when the field is swept up and down is however something that should not be there in that case.

The comparison of the TMR measurements when the field is applied in and out of the plane of the sample, confirm what can be seen in the VSM measurements that the easy axis of magnetization is not well defined. The deviations from the parabolic background when H is applied out of plane

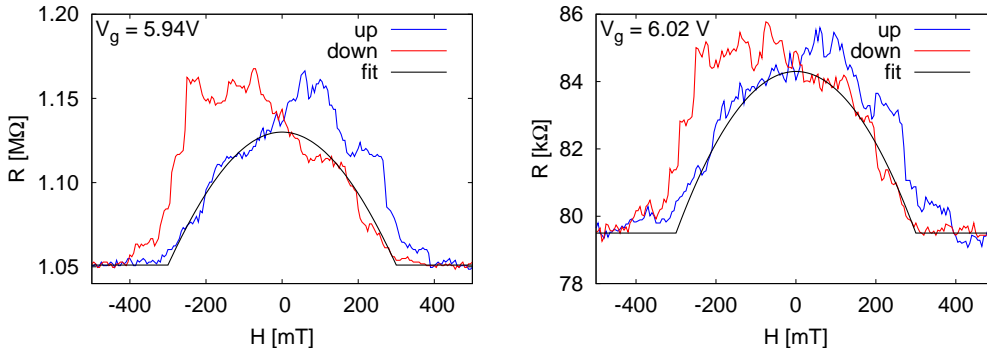


Figure 5.7: Two examples of the spin signal for different gate voltages when field is applied out of plane of the sample.

and the pre switching, when the magnetic field is applied in-plane, points to the same conclusion as can be drawn from previous measurements: The electrodes are not single magnetic domain.

Ferromagnetic domains can be imaged by magnetic force microscopy (MFM). In order to investigate this further MFM imaging was done on one of our samples³. In Fig.5.8 an MFM scans of one electrode 300 nm wide and 2 μm long can be seen. The scans were made at temperatures of 7 K applying magnetic field out of plane of the samples. In this MFM setup the out of plane component of the magnetic field is measured using a cantilever with a magnetic tip of single domain. At zero applied magnetic field some magnetic landscape can be seen. It looks like that the electrode is divided into domains by zig-zag domain walls. When the field is applied the magnetic contrasts get weaker and at field of 300 mT the domains have disappeared and the electrode is magnetized along the applied field. The dark spot in the middle and the end are due to topological features of the electrode.

5.3.3 Co and NiFe

In addition to working with PdNi electrodes, encouraged by already published work we decided to use other F materials, Co and $\text{Ni}_{81}\text{Fe}_{19}$ (permalloy), which have better controlled magnetic properties.

Cobalt

Co is often used, both in research and in industrial applications and thus its magnetic properties are well known. Co has spin polarization of 36 – 52%

³MFM measurements were done by the group of Prof. Hans Hug at University of Basel.

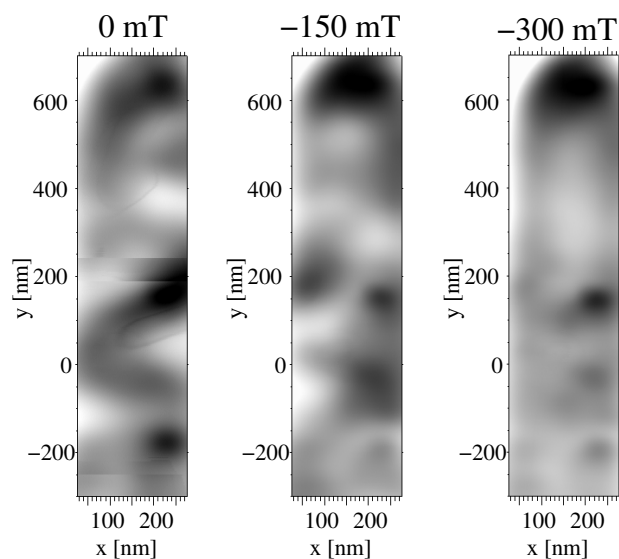


Figure 5.8: MFM images of one electrode of PdNi. The MFM images are taken for three different strength of magnetic field applied out of plane of the sample. The color scale represents the strength of the out of plane component of the magnetization of the electrode.

[58], which is higher than of PdNi, and it has already been used to make carbon nanotube spin devices [7–9, 16]. Co is known to make a reasonably good contact to multiwall carbon nanotubes (MWCNT) [7–9] and it has also been used to contact to SWCNT (see e.g. [16] but in this work it was not clear if ropes of individual tubes were contacted).

SWCNT were contacted with 40 nm thick Co electrodes, which were covered with 10 nm Pd cap layer in order to prevent oxidation of the Co. The Co was evaporated on the sample with E-gun evaporation at pressure of 4.3×10^{-8} mbar and rate of 0.4 \AA/s . The SWCNTs were contacted by four identical electrodes, that were $3 \mu\text{m}$ long and 200 nm wide (see Fig.5.9(a)).

We have found during characterization that Co does not make good contacts to SWCNT. The yield of working devices was low and their resistances at room temperature high, especially if the nanotubes are semiconducting. The lowest value of room temperature resistance was $\sim 200 \text{ k}\Omega$ for metallic tube and $1 \text{ M}\Omega$ for semiconducting tubes. Normally the resistances were higher or of the order of few $\text{M}\Omega$.

Sample with lowest resistances were cooled down to low temperatures ($T = 1.8 \text{ K}$) where magnetic sweeps were made. It sometimes happens that contact to the SWCNT is lost when the sample is cooled down. Two examples

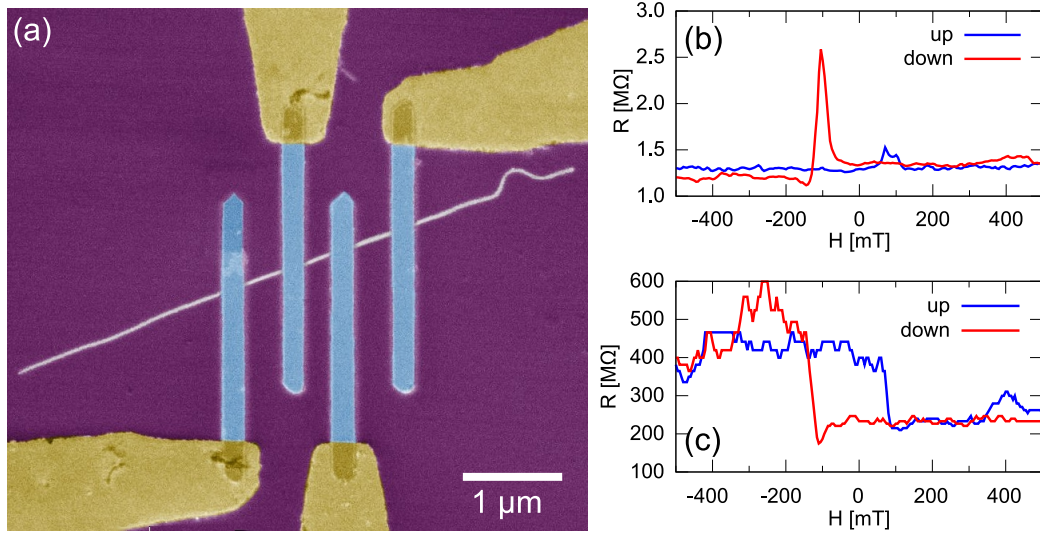


Figure 5.9: (a) The device used when testing Co as a contact material. A SWCNT is contacted by 3 μm long, 200 nm wide and 40 nm thick Co electrodes. The electrodes were covered by 10 nm thick cap layer to prevent oxidation. (a) TMR measurements on the device. These curves were measured over the central segment of the device. (b) TMR measurement on the right segment of the same device. The resistance is much higher on this segment even though the same tube is contacted.

of magnetic sweeps are shown in Fig.5.9(b) and (c). Both measurements were done on the same device. The measurement in (b) was done on the middle segment of the device while the measurement in (c) was done on the right segment. The resistance of the right segment is $100\times$ higher than of the middle segment. This huge difference in the transparencies of identical contacts to the same nanotube shows that the process of contacting SWCNT with Co is not a reliable one.

The resistance (R) as a function of applied magnetic field (H) has somewhat the expected characteristics in the sweep shown in Fig.5.9(b). The peak in R when the field is swept up is, however, much lower than the peak when sweeping down, but these peaks are expected to be more or less of the same height.

The curves in Fig.5.9(c), when the right segment of the device is measured, are quite different from what to expect from a spin device. Such a behavior has been reported before and has been explained by pinning of the magnetization of one of the electrodes [59].

This pinning has been dominant in the samples contacted by Co. A

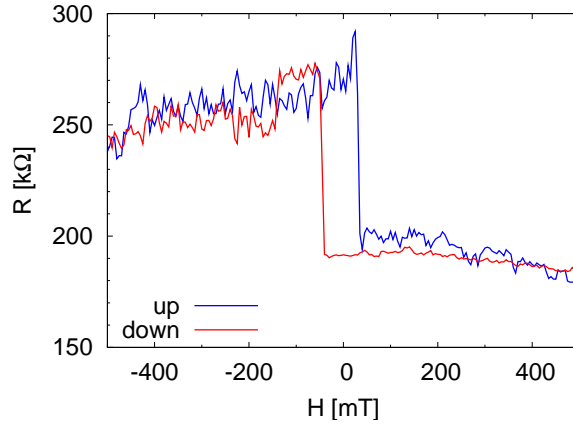


Figure 5.10: Resistance (R) as function of applied magnetic field H of a SWCNT device, which was contacted using permalloy.

pinning of one electrode is not a likely explanation. First of all the electrodes used in the measurements are identical (see Fig.5.9) and there is no reason for only one electrode to be pinned. The mechanism responsible for pinning magnetic layers is exchange bias between ferromagnetic and antiferromagnetic layers. The exchange bias is a small effect seen in thin ferromagnetic/antiferromagnetic (F/A) bilayers. It originates from the exchange over the F/A interfaces. So called field cooling, when the bilayer is cooled below the Néel temperature of the A layer in the presence of magnetic field is used to establish the exchange bias [60, 61]. CoO in the electrodes could cause some exchange bias. However the sample was cooled down in the absence of magnetic field and such bias should only shift the switching a few mT.

Permalloy

Permalloy (Py, $\text{Ni}_{81}\text{Fe}_{19}$) has a high spin polarization of 46 – 65% [58] and if it makes good contact to SWCNT its high spin polarization should induce a high TMR signal in Py-based SWCNT devices. It is a soft magnet, which means that the shape of the FM electrodes should control the easy axis and the switching field of the electrodes. Py makes much better contact to SWCNT than Co and the contacts are not lost, when cooling down to cryogenic temperatures, like it often happens with the Co devices.

The TMR signal is however not optimal. An example of such measurement is Fig.5.10 and it can be seen that it has this same “pinning” as seen in the Co devices. As in the Co devices, one electrode doesn’t seem to switch

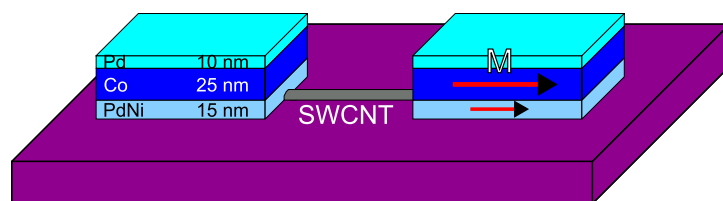


Figure 5.11: Electrodes of a PdNi/Co bilayer shown schematically. The tube is contacted with a thin 15 nm thick PdNi layer. On that a 25 nm thick cobalt layer is evaporated. The Co is supposed to control the magnetic properties of the sandwich. A 10 nm thick cap layer of Pd is for preventing oxidation.

even at magnetic fields of 1 T.

5.3.4 PdNi/Co bilayer

The results of experiments with contact materials are that PdNi makes a good contact to SWCNT and the spin-valves work quite well but there are some problems with the switching. The SWCNT spin-valves where the “good” magnetic materials Co and Py are used show a strange switching behavior. The Py makes a reasonably good contact to SWCNT and the characteristics of the SWCNT at low temperatures look normal. It is however harder to make stable Co contacts to SWCNT, that work at cryogenic temperatures.

The question is: Is it possible to combine the magnetic properties of, e.g. Co and the contacting properties of Pd or PdNi. One approach to that problem is to try a new alloy as contact material, like PdCo or even PdNiCo. The approach used in this work was to use a PdNi/Co bilayer. This bilayer consist of 15 nm thick PdNi that contacts the tube and a 25 nm thick Co layer grown on top. To prevent oxidation, of the bilayer, it is capped with a 10 nm thick Pd layer. This structure is shown schematically in Fig.5.11. Such a thick Co layer is magnetized in plane of the sample and the Co layer should thus fix the magnetization of the contacting PdNi layer in plane of the sample.

The magnetization of a PdNi/Co/Pd control film was measured by vibrating sample magnetometry (VSM) as function of applied magnetic field is shown in Fig.5.12⁴. The field was applied both in plane of the film and out of plane. The magnetic properties look much better than the properties of

⁴VMS measurements were done by group of Dr. Christoph Sürgens at the University of Karlsruhe.

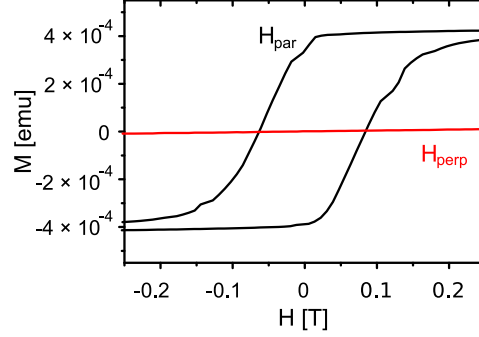


Figure 5.12: Magnetic properties of PdNi/Co/Pd film. The magnetization of the film measured with VSM with field applied in-plane of the sample (black) and perpendicular to it (red).

the PdNi (see Fig.5.4). A switching can be seen in the magnetization when the field is applied in plane but no switching is seen when it is applied out of plane. This is a strong indication that the easy axis of the PdNi/Co/Pd film is in plane.

Anisotropic magnetoresistance (AMR) measurements were done on PdNi/Co/Pd electrodes of a spin-valve device of the type shown in Fig.5.2(a). These measurements are shown in Fig.5.13. The Resistance (R) of the electrodes was measured as function of magnetic field (H), applied out of plane of the sample and in plane of the sample, parallel to the electrodes.

If the easy axis of magnetization of the electrode is along its elongated structure, the shape of the $R(H)$ curve should be parabolic, when H is applied perpendicular to it. As mentioned in Section 2.2.5 the resistance of a ferromagnet as function of the angle between current \mathbf{I} and magnetization \mathbf{M} (θ) is given by

$$\rho(\theta) = \rho_{\parallel} + \rho_{\Delta} \cos^2 \theta, \quad (5.7)$$

where ρ_{\parallel} is the resistivity, when \mathbf{I} and \mathbf{M} are parallel, and $\rho_{\Delta} = \rho_{\perp} - \rho_{\parallel}$, where ρ_{\perp} is the resistivity when \mathbf{I} and \mathbf{M} are perpendicular [27]. The situation can be described by Fig.5.6. The easy axis of magnetization and the current flow are along the x -axis and the magnetic field \mathbf{H} is along the y -axis is pulling \mathbf{M} out of the plane. As above, the angle θ is given by Eq.(5.3) and by substituting for θ in Eq.(5.7) from Eq.(5.3) the following relation of ρ as

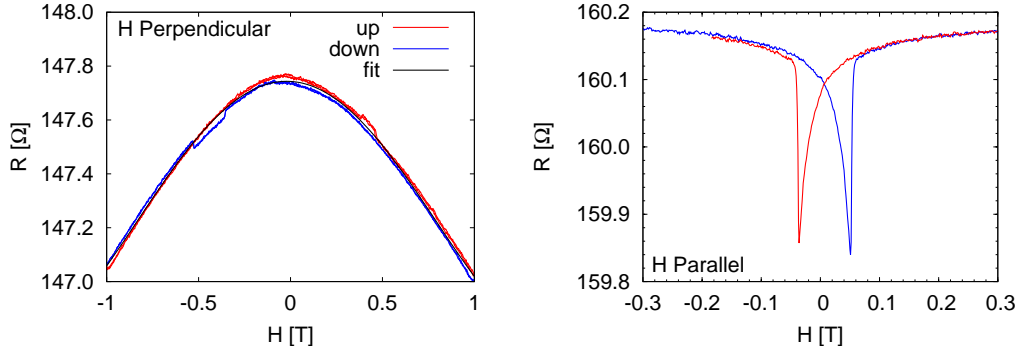


Figure 5.13: AMR measurement of PdNi/Co/Pd electrodes. The resistance of the electrodes (R) is measured as function of field (H) applied out of plane (left) of the sample and in plane (right) of the sample along the electrode. The measurements were done on a device of the type shown in Fig.5.2(a).

function of H is obtained

$$\rho(H) = \begin{cases} \rho_{\parallel} + \rho_{\Delta} \left[1 - \left(\frac{MH}{K} \right)^2 \right] & \text{if } |MH| \leq K \\ \rho_{\parallel} & \text{if } |MH| > K, \end{cases} \quad (5.8)$$

which is parabolic for $|H| < K/M$. The measurement shown in Fig.5.13 indicate that \mathbf{M} of both electrodes is not fully aligned with \mathbf{H} , when $H = 1$ T, since no end of the parabolic structure can be seen as predicted by Eq.(5.8). That is an indication that the anisotropy energy is much higher than that of PdNi.

AMR measurements of PdNi/Co/Pd electrodes when the magnetic field is applied along the F electrodes indicate that the electrodes have a polycrystalline structure. The net magnetization of the electrode is along the elongated structure of the electrode. High H aligns the magnetizations of the domains. When the field is lowered and reversed the magnetization of individual crystals turn slowly a bit out of the alignment with the axis of the electrode until they flip over to reverse magnetization. With higher H in the opposite direction they align again with the field.

The TMR signal of a SWCNT spin-valve with PdNi/Co/Pd electrodes, when the magnetic field (H) is applied along the electrodes, is shown in Fig.5.14. The switching is sharp and much sharper than seen in PdNi contacts. This is what is expected from the spin-valve, given the results of the VSM and the AMR measurements of the PdNi/Co/Pd.

One should however be aware that the spin-valve does not always behave so well as shown in Fig.5.14. The spin-valve characteristics have improved as

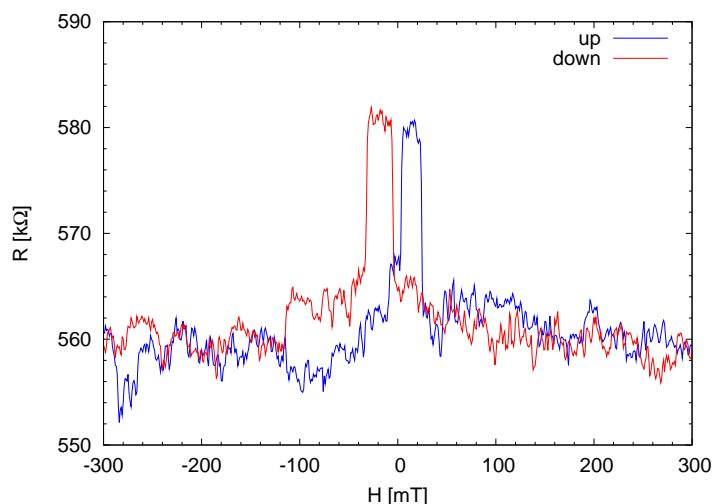


Figure 5.14: The resistance of SWCNT contacted with PdNi/Co electrodes plotted as function of applied magnetic field H , which is applied along the electrodes. The switching looks more regular than in devices contacted with PdNi.

predicted by the TMR and the AMR measurements but there are two things that one should bear in mind:

- Both the VSM and the AMR measurement depend on the total magnetization of the PdNi/Co/Pd sandwich. It is the PdNi layer alone that contacts the nanotube and it is hard to tell from the measurements what that layer is doing in detail.
- The Co layer has higher magnetic moment and higher anisotropy energy than the PdNi layer. Spurious effects on the edge of the electrodes due to stray fields could cause domains with different magnetization to be located where the nanotube is contacted.

Measuring the TMR of the spin-valve, as shown in Fig.5.14, is thus the only way to check if the Co layer makes the characteristics better.

5.4 Temperature dependence of TMR

The temperature dependence of the TMR has also been measured. These measurements were done in a valley between two coulomb peaks in the linear response (G as function of V_g) as shown in the inset in Fig.5.15. The TMR

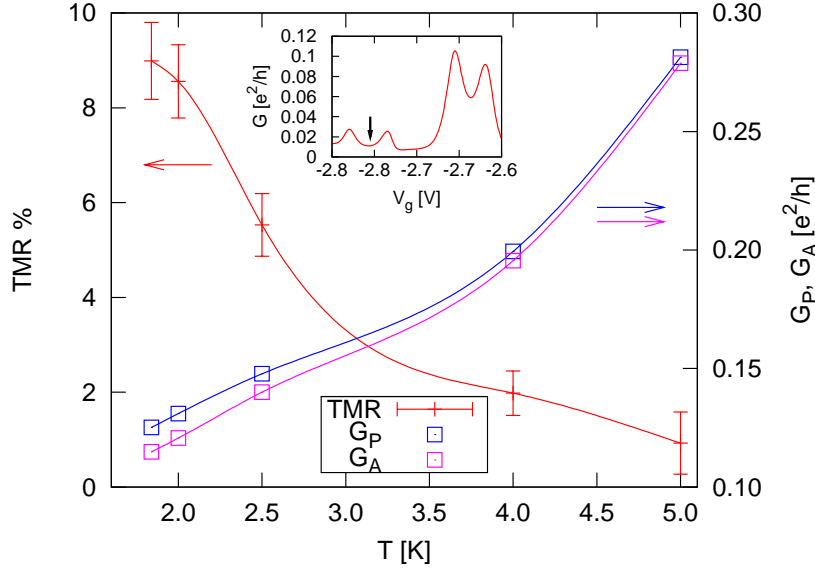


Figure 5.15: Temperature dependence of TMR and the conduction both for parallel and antiparallel magnetization of the electrodes (G_P and G_A respectively). The interpolation curves are put as a guide to the eye. The inset shows linear response (G as function of V_G). The arrow shows at which gate voltage the TMR measurements were done

signal was measured at few different temperatures between 1.8 K and 5.0 K. The TMR and the conductances for parallel and perpendicular magnetization of the electrodes (G_P and G_A respectively) are plotted as function of temperature in Fig.5.15. Both the TMR signal and G_P and G_A are strongly dependent on the temperature in this temperature range.

In order to check if the temperature dependence of the TMR is coming from changing magnetic moment of the electrodes, AMR measurements were done. The measurements were done on the devices shown in figure Fig.5.1(a) at temperature of $T = 1.8$ K and $T = 10$ K. The difference in the AMR signal between these temperatures is negligible. In Fig.5.16 the measurements are shown and the curve representing the resistance of the electrode (R) when $T = 1.8$ K has been shifted up 40 m Ω to match the curves. After this shift the curves fall together indicating that there are no significant changes in the magnetization of the electrodes in this temperature range and therefore the observed T dependence can not be explained by that.

From Fig.5.15 it can be seen that TMR decreases as the conductances (G_A and G_P) increases with temperature. That indicates that the T -dependence

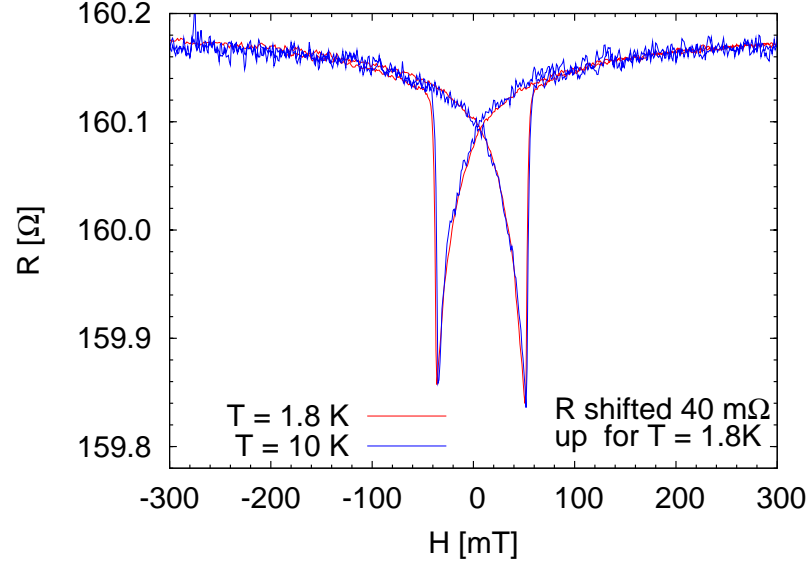


Figure 5.16: AMR measurements on FM electrodes at temperatures (T) of 1.8 K and 10 K. The resistance of the electrodes was measured as function of applied magnetic field (H) while sweeping it subsequently up and down. Curve for the $T = 1.8$ K is shifted upwards by 40 m Ω to match the curves.

of the TMR could originate from relative changes in spin dependent and spin independent resistance in the spin-valve. A simple resistor model of the device is shown in the inset of Fig.5.17. According to Mott's two current model the flow of spin up and spin down electrons can be treated separately [33]. The device is modelled as two channels in parallel, one for spin up and one for spin down electrons. The spin quantization axis is along the electrodes in the same direction as the external field is applied. The spin dependent resistances $R_{\uparrow(\downarrow)}$ represent the contact resistances of the F electrode to the nanotube and R is a spin independent resistance, the inner resistances of the nanotube device. The spin dependent resistance are given by

$$R_{\uparrow(\downarrow)} = \frac{R'}{2}(1 \pm P), \quad (5.9)$$

where R' is the spin independent contact resistance and P is the polarization of the electrodes. The sign is *positive* if the spin and the magnetization of the electrode are *antiparallel* and *negative* if the spin and the magnetization of the electrode are *parallel*.

For parallel magnetization of the electrodes the resistance of the circuit

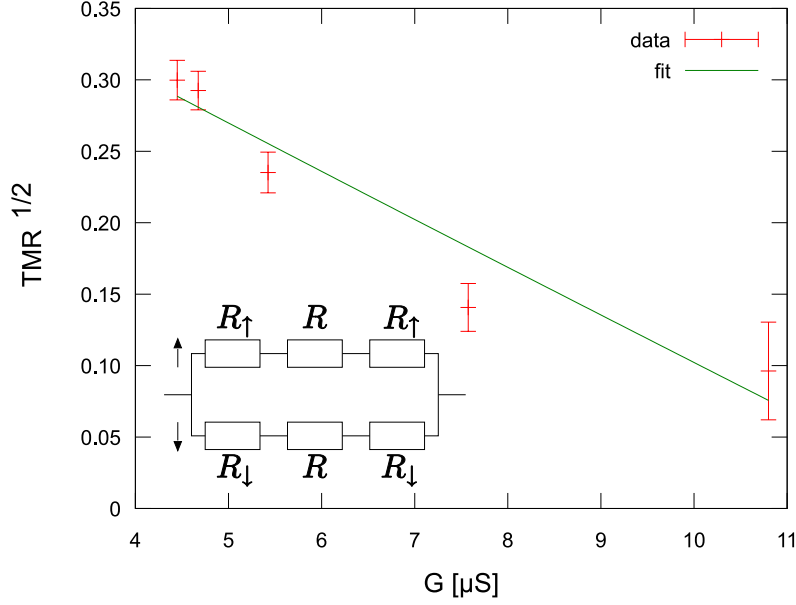


Figure 5.17: Inset: A resistor model of the spin-valve. The contacts to the electrodes are modelled using spin dependent resistors ($R_{\uparrow(\downarrow)}$). The inner resistance of the device (R) is spin independent. Main panel: The square root of the T dependent TMR signal plotted as function of simultaneously measured conductance G_A . Data are fitted using Eq.(5.13).

is given by

$$R_P = \frac{(R + R'(1 + P))(R + R'(1 - P))}{2(R + R')} \quad (5.10)$$

and for antiparallel magnetization it is

$$R_A = \frac{R' + R}{2}. \quad (5.11)$$

The TMR signal of the circuit is thus given by

$$TMR = \frac{P^2 R'^2}{((1 - P)R' + R)((1 + P)R' + R)} \approx \frac{P^2 R'^2}{(R' + R)^2} \quad (5.12)$$

The device is a quantum dot at these temperatures and its resistance obeys the Breit-Wigner relation [62]. As said above the measurements were done at high resistance in a valley between coulomb peaks in the linear response (i.e. in G as function of V_g). When the temperature gets higher the peaks in the linear response get broader resulting in lower resistance in the

valleys between the conduction peaks [63]. In the resistor model we model this by assuming that the contact resistance of the nanotubes R' decreases with higher temperature, but the spin independent resistance (R) is constant.

A simple relation between TMR and $R_A = 1/G_A$ (both parameters measured as function of T) can be obtained by substituting for R' in Eq.(5.12) using Eq.(5.11) and taking the square root of both sides:

$$\sqrt{TMR} \approx P \frac{2R_A - R}{2R_A} = P \left(1 - \frac{1}{2} \frac{R}{R_A}\right) = P \left(1 - \frac{1}{2} R G_A\right). \quad (5.13)$$

In Fig.5.17 the square of the TMR is plotted as function of G_A with a fitting line obtained using Eq.(5.13), where P and R are fitting parameters. The obtained values of the fitting parameters are $P \sim 0.2$, which is higher than one expects for PdNi⁵, and $R = 150 \text{ k}\Omega$, which is too high. For vanishing R' , which is what one can expect for high temperatures, the resistance of the device according to Eq.(5.11) becomes $R/2 = 75 \text{ k}\Omega$. This is much higher than the expected inner resistance of SWCNT ($h/4e^2 = 6.45 \text{ k}\Omega$) and significantly higher than the room temperature resistance of the device, which was $\sim 30 \text{ k}\Omega$.

The relative changes in spin dependent and spin independent resistances in the device with temperature are thus not sufficient for explaining the temperature dependence of TMR . There must be some spin relaxing mechanism taking place in the system. As mentioned in the beginning of the chapter the spin orbit-coupling and the hyperfine interaction are very weak in carbon, which should provide a long spin coherence length. It is after all that, what makes SWCNT interesting for spin transport experiments.

The source of the spin relaxation could originate from the coupling to the ferromagnetic contacts. There are always some irregularities in the magnetization of the F electrode on the contact point to the SWCNT. Such irregularities could mix the spin up and spin down eigenstates of the electrons in the nanotube quantum dot and thus cause spin relaxation. The coupling is dependent on temperature and at higher temperatures it is higher, which should result in higher spin relaxation.

⁵In previous work the polarization has been estimated to be $\sim 10\%$ [11]

Chapter 6

Non-local measurements

6.1 Introduction

Recent realization of the spin field effect transistor in carbon nanotubes (CNT)s three-terminal device [11, 12], where a back-gate modulates the transport of a two terminal spin-valve, demonstrated the ability to control spin transport in a quantum dot (QD), which is formed in this system [64, 65]. Single wall CNTs (SWCNT)s are interesting from fundamental point of view since they are truly one dimensional (two channels per SWCNT) with ballistic transport characteristics [66]. However, additional effects can contribute to the observed signals in two terminal spin-valves. These effects are mainly found to be dominant by the contacts in the device [67] [68] It seems clear, that despite a number of large responses seen in the CNT-based two terminal devices [11, 12, 69–71], one needs to go beyond the two terminal structures by realizing a multi-terminal device where non-local measurements are feasible [16]. The non-local measurement technique separates spin from charge effects by passing the current through the injection branch of the device and detects the non-local voltage due to propagation of spin in the part of the device which does not lie in the charge current path. This makes the detection part sensitive only to the chemical potentials of the propagating spin up and spin down channels. If the charge current is zero and the spin up and spin down channels are at the same chemical potential, the resulting non-local voltage is expected to be zero. The non-local measurements have been pioneered by Johnson and Silsbee [72] in metallic spin-valves and further applied to various other metallic systems [73], as well as in bulk GaAs [74] and graphene [75]. Recent application of the non-local spin technique in CNTs [16] demonstrated the plausibility of performing such measurements in a low dimensional mesoscopic systems. The hallmark of these measurements

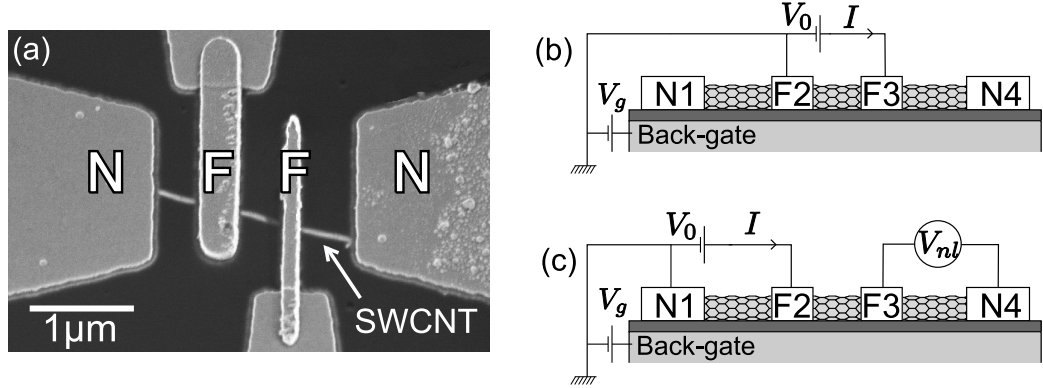


Figure 6.1: (a) SEM-image of the device. SWCNT is contacted with two ferromagnetic contacts (F) and two Normal contacts (N). (b) 2-point measurement shown schematically. (c) Non-local measurement. Current driven through one arm of the sample and voltage measured on the other.

is that positive voltage is measured when the injector and detector electrodes are parallel and negative *only* when they are antiparallel. However, it has been reported recently that the four point measurements with non-magnetic probes in SWCNTs can yield a negative resistance due to the interference effects [76]. This suggests that the measurement of the non-local spin transport in the mesoscopic systems like CNTs might be influenced by additional, novel, effects.

6.2 Measurements

The samples and the measurement setups are shown schematically in Fig.6.1. Samples were cooled in He4 cryostat to 1.8 K where the differential conductance ($G = dI/dV_0$) was measured using standard low frequency lock-in technique, with excitation voltage $V_0 = 100 \mu V$ (see Fig.6.1(b)). Measurements were made across all three segments of the sample (see Fig.6.2) in the gate voltage V_g range $V_g \in [-3.1 \text{ V}, -2.6 \text{ V}]$. With this kind of measurements transport characteristics of each segment is obtained in the linear regime. In addition, by sweeping the source-drain (DC) voltage between $(-6mV, 6mV)$, we obtain a gray scale plot, as shown in the inset of Fig.6.2(c).

The three segments of the SWCNT have different conductance characteristics in this voltage range. This shows that the charge and spin transport in one such system strongly depends on the coupling of each contact as well as the mutual position of the energy levels of the QDs. In the same back-gate voltage range and zero applied magnetic field, we characterize the non-local

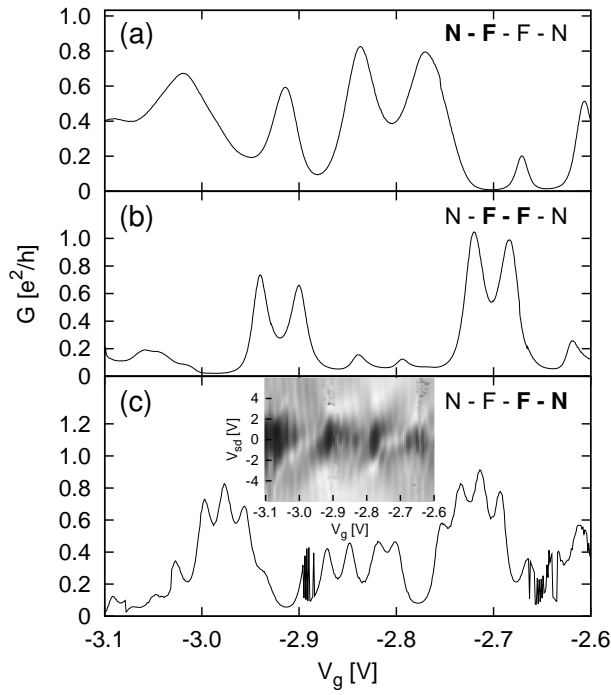


Figure 6.2: Linear conductance (G) of each segment of the device as function of gate voltage (V_g). In (a) the conductance of the left segment; between the left F and N contacts, in (b) of the middle segment; between the F contacts, and in (c) of the right segment; between the right F and N contacts. The inset in (c) shows the grayscale measurement (dI/dV as function of V_g and source-drain bias, V_{sd}) of the right segment in the same range of V_g . V_{sd} is between ± 6 mV.

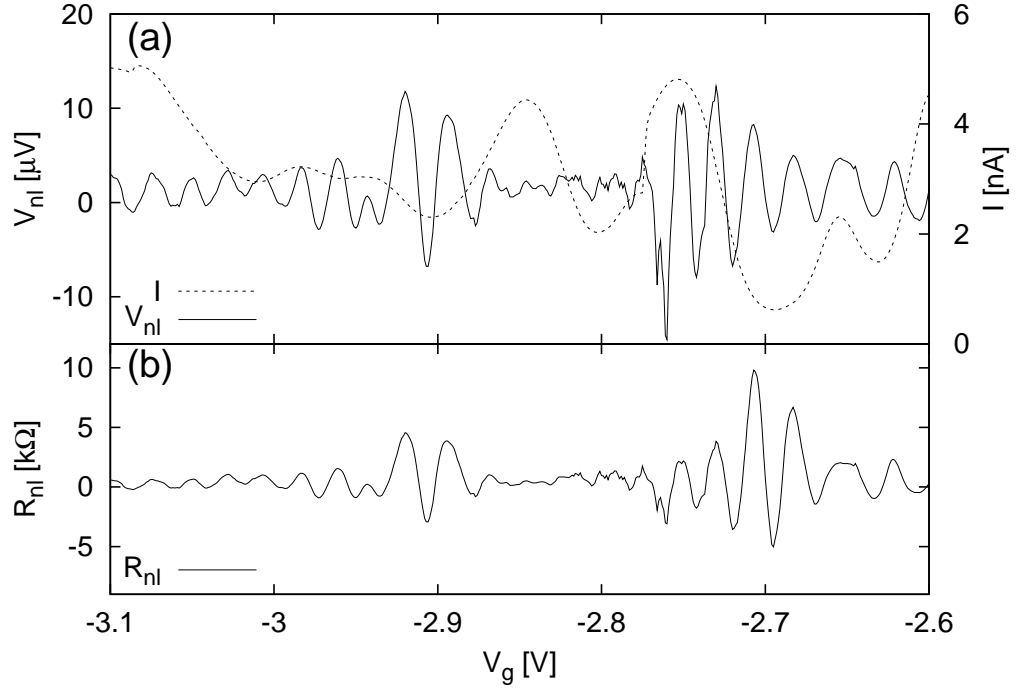


Figure 6.3: Non-local measurement as function of gate voltage (V_g). (a) the current between N1 and F2 electrode (I) is plotted with the non-local voltage measured between F3 and right N4 electrodes (V_{nl}). (b) calculated non-local resistance ($R = V_{nl}/I$) as a function of the gate voltage.

resistance response of the device. The current, I , is injected through the segment N1-F2 driven by a constant voltage V_0 of $200 \mu\text{V}$, and the non-local voltage drop is measured across segment F3-N4 (see Fig.6.1(c)). The results are presented in the Fig.6.3. The top graph shows measured current (dashed line) and non-local voltage as a function of the back gate voltage. The lower graph of Fig.6.3 shows calculated non-local resistance $R_{nl} = V_{nl}/I$.

In the measurements we see oscillating non-local voltage V_{nl} and resistance R_{nl} , which change sign and magnitude as the back-gate voltage is swept. The V_{nl} and R_{nl} are modulated by the QD characteristics of the detection segment of the circuit (see Fig.6.2(c)), which is in contrast with the expected constant background for the fixed magnetic field.

The modulation of the V_{nl} by the QD characteristics of the detection segment can be seen even clearer in another device (see Fig.6.4). The measurements are done in the same way, I , is injected through the segment N1-F2 driven by $V_0 = 200 \mu\text{V}$, and V_{nl} is measured across segment F3-N4 (see

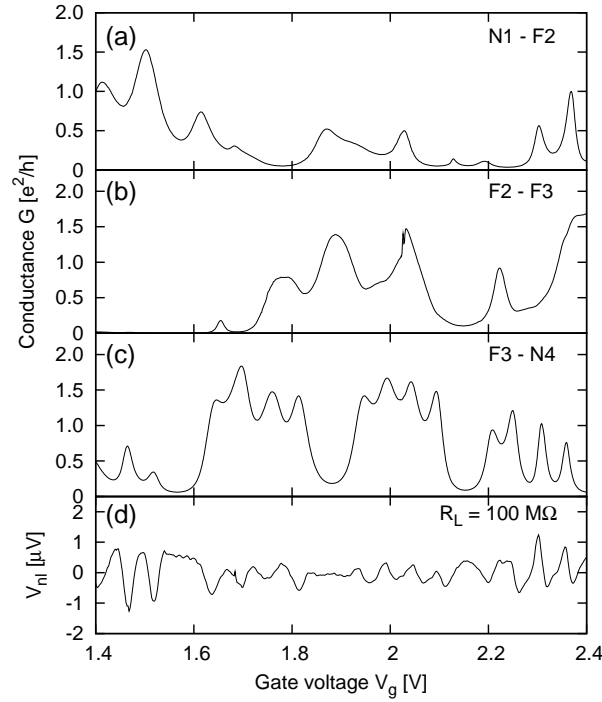


Figure 6.4: The linear conductance (G) of each segment of another device. In (a) the conductance of the left segment; between the F1 and N2 contacts, in (b) of the middle segment; between the F contacts, and in (c) of the right segment; between the F3 and N4 contacts. (d) Shows the non local voltage (V_{nl}) when the F3-N4 segment is used as a detector and the N1-F2 as an injector.

Fig.6.1(c)). The difference here is that the input resistance of the voltage probes was $100\text{ M}\Omega$ instead of $10\text{ M}\Omega$ in the measurements in Fig.6.3. It can be seen that the G as a function of V_g in the detection segment has the four fold symmetry, which is the hallmark of good metallic SWCNT quantum dots. The V_{nl} is modulated in the way, that a valley appears in $V_{nl}(V_g)$ when there is a peak in G_{F3-N4} .

6.3 Resistor model

We model our device as a network of resistors, Fig.6.5. The normal terminals N1 and N4 are characterized with contact resistance of $R_i, i = 1, 4$ and an additional contact resistance r_i . The ferromagnetic terminals F2 and F3 are

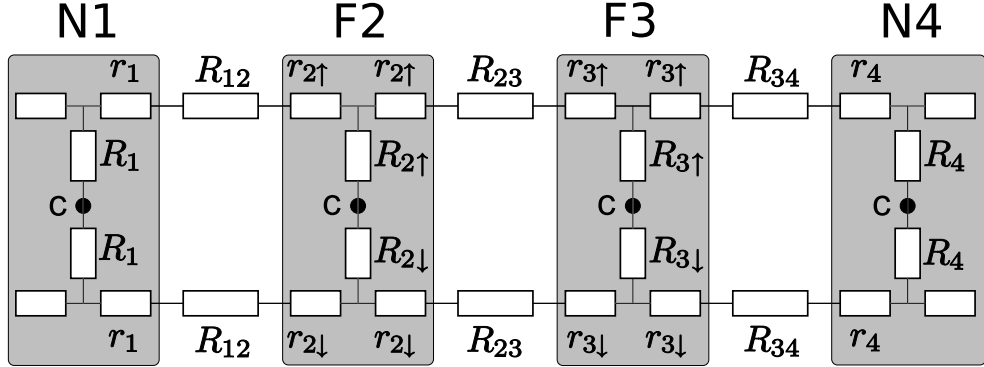


Figure 6.5: The resistor model shown schematically. Connection points are marked with **c**. The terminals are characterized by a contact resistance R_i and an additional contact resistances r_i evenly distributed to the left and the right of the contact. There are separate channels for spin up and spin down electrons.

characterized with spin dependent contact resistance $R_{i\uparrow(\downarrow)}$ and spin dependent additional contact resistance $r_{i\uparrow(\downarrow)}$, evenly distributed to the left and the right of each terminal. The spin dependent resistance are given by

$$\begin{aligned} R_{i\uparrow(\downarrow)} &= (1 \pm P)R_i \quad i = 2, 3 \\ r_{i\uparrow(\downarrow)} &= (1 \pm P)r_i \quad i = 2, 3, \end{aligned} \quad (6.1)$$

where P is the spin polarization of the electrodes the sign is negative for majority spins and positive for minority spins¹. The SWCNT sections between terminals i and j have resistances R_{ij} . The circuit is branched into spin up and spin down parts once we consider the ferromagnetic nature of the middle electrodes within the Mott two current model [32].

The TMR signal is defined as

$$TMR = (R_A - R_P)/R_P,$$

where $R_{P(A)}$ is the resistance when electrodes are magnetized in (anti)parallel directions. The local TMR signal between the F electrodes estimated from the model is

$$TMR = \frac{4P^2 R'_2 R'_3}{((1 - P)(R'_2 + R'_3) + R_{23})((1 + P)(R'_2 + R'_3) + R_{23})} \quad (6.2)$$

¹Majority spins are parallel to the magnetization of the electrode and minority spins are antiparallel [17]

where $R'_i = R_i + r_i$, i.e. the sum of the both contact resistances. The estimated local TMR signal in the case of ballistic transport through the tube ($R_{23} = 0$) is maximized for the symmetric contacts ($R'_2 = R'_3$) giving

$$TMR_{i,max} = \frac{P^2}{1 - P^2} \quad (6.3)$$

In this estimate we have neglected the outer N electrodes. They mix the spin up and spin down channels and can be taken into account as a resistor R_L in parallel to the contact resistances. The local TMR signal assuming ballistic transport ($R_{23} = 0$) is then given by

$$TMR = \frac{4P^2 R'_2 R'_3 R_L}{(1 - P^2)(R'_2 + R'_3)(R_L(R'_2 + R'_3) + 4R'_2 R'_3)}, \quad (6.4)$$

(where $R'_i = R_i + r_i$) In ballistic regime this can significantly lower the TMR signal, when R_L is low. If all R_i are symmetric and all r_i are vanishing

$$TMR = \frac{1}{3} \frac{P^2}{1 - P^2}. \quad (6.5)$$

Measured TMR $\sim 3.4\%$ as a function of applied in-plane magnetic field between electrodes F2 and F3 is shown in Fig.5.14 at $V_g = -2.875V$. The spin polarization calculated using Jullière's model [18] is $\sim 13\%$. the resistor model (Eq.(6.3)) yields higher spin polarization or $\sim 19\%$.

The expected non-local TMR value (see Fig.6.1(c)) can be calculated from the resistor model. The general result, including all resistors of the network, is quite complicated.

The non-local TMR estimated in the case of ballistic SWCNT ($R_{i,j} = r_i = 0$) is

$$TMR_{nl} = \frac{V_0 P^2}{(R_1 + R_2)(\sum G_i)}, \quad (6.6)$$

where $G_i = R_i^{-1}$. From this expression we see that the non-local signal is maximized when R_1 and R_2 are small (high transmission) but vanishes as they become large (low transmission). Furthermore, when R_3 and R_4 are large the non-local signal is finite and vanishes as they become very small.

We also calculated the TMR_{nl} signal from the resistor model assuming a resistance in the middle segment of the tube,

$$TMR_{nl} = \frac{V_0 P^2}{(R_1 + R_2) \left((G_1 + G_2 + G_3 + G_4) + R_{23}^{tot} (G_1 + G_2)(G_3 + G_4) \right)}, \quad (6.7)$$

where R_{23}^{tot} is the total resistance of the connection between injector and detector which also includes the additional contact resistances r_2 and r_3 .

We now calculate the non-local voltage neglecting the F nature of the two middle contacts. As shown in Fig.6.1(c), the current is injected through electrode F2 and drains at the electrode N1. The non-local voltage V_{nl} is measured between electrodes F3 and N4. Within the model, where the charge current flows through the detection branch of the device, the non-local voltage of the ballistic SWCNT at zero field is:

$$V_{nl} \sim \frac{V_0(R_3 - R_4)}{R_I}, \quad (6.8)$$

where R_I is the input impedance of the voltage probes. From the above expression we see that depending on the relative ratio of the contact resistances of the detector part of the circuit, the non-local voltage can be both positive and negative as the transmissions of the contacts change with the applied back-gate voltage.

Using the resistor model for polarized current flow Eq.(6.6) through the device, we have calculated the amplitude of the non-local spin signal. From the estimated spin polarization of our electrodes ($P \sim 15\%$) [12] the highest value of the V_{nl} which is only due to the spin transport is $\sim 0.1\%$ of V_0 , *i.e.* $V_{nl} \sim 0.2\mu V$.

Direct comparison to the measured V_{nl} (Fig.6.3(a)), shows that the expected non-local signal only due to the propagation of the spin is found only for certain values of the back-gate voltage, while it breaks down with values of the non-local resistance much higher than expected from the resistor model, with amplitudes $\sim 10 \mu V$.

V_{nl} has this maximum amplitude when $V_g \in [-2.75, -2.80]$ (see Fig.6.3(a)). The resistance of the detection segment in this interval is $\sim 40 \text{ k}\Omega$. We take this value for the difference in the contact resistances of the detector segment ($R_3 - R_4$) when estimating V_{nl} using the resistor model (Eq.(6.8)). The non-local signal was measured with $R_I = 10 \text{ M}\Omega$ and the maximal value of V_{nl} from Eq.(6.8) is $V_{nl} \sim 1 \mu V$. The observed oscillations are 10 times bigger than this.

This is also the case when measuring $V_{nl}(V_g)$ with higher input impedance as done in the second non-local measurement (see 6.4), where $R_I = 100 \text{ M}\Omega$. The maximal amplitude of V_{nl} is $\sim 1 \mu V$ when $V_g \in [1.4, 1.5]$ and the resistance of the detection segment in this interval is $\sim 100 \text{ k}\Omega$. Estimating the amplitude of V_{nl} using Eq.(6.8) yields $0.2 \mu V$, which is still smaller than observed.

This is of the same order of magnitude as TMR_{nl} that we expect, estimated from the resistor model. The TMR_{nl} signal was however not resolved

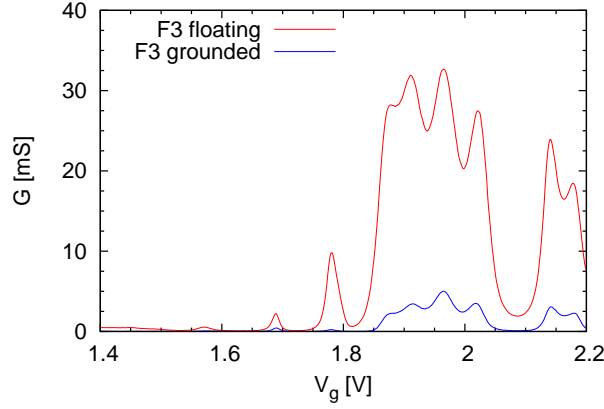


Figure 6.6: Conductance G measured as a function of V_g between F2 and N4, when F3 is floating (red line) and grounded (blue line). The difference is ~ 5 fold.

in this sample. When estimating the expected TMR_{nl} signal using Eq.(6.8) we do not take the resistance between the injector and the detector segment into account. That is done in Eq.(6.7), where R_{23}^{tot} represent this resistance including all the additional contact resistors r_2 and r_3 . The size of these resistors can be estimated by measuring the conductance (G) over two segments. In Fig.6.6 the conductance between F2 and N4 is measured, once with F3 grounded and once with it floating. The difference in the conductance is ~ 5 fold which means that the additional conductance resistances r_3 are four times bigger than R_3 . Measuring the conductance between N1 and F3 in the same way yields similar result, the additional conductance resistances r_4 are almost ~ 5 times bigger than R_4 .

The additional contact resistances r_3 and r_4 are thus higher than the R_3 and R_4 resulting in a significant size of R_{23}^{tot} in Eq.(6.7), which can explain why the non-local spin signal is not resolved in our measurements.

6.4 Possible source of oscillations

We further focus on the origin of the current flow in the detector arm of our device. Surprisingly, we found that the amplitude is still larger than expected when the input impedance of the voltage probes is increased by an order of magnitude and therefore pointing to another mechanism which plays a crucial role in the appearance of the observed oscillating non-local signal. We believe that this is possible due to the interference effects in our mesoscopic device.

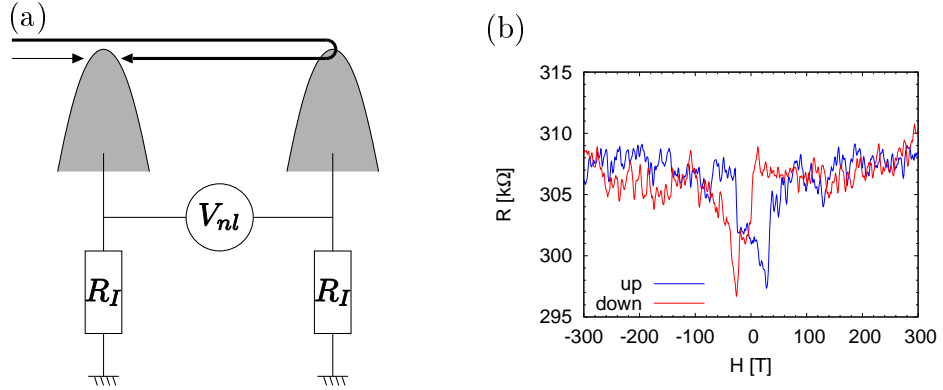


Figure 6.7: Transmission through the F - N. (a) depicts the electronic wave function propagating to the detector part of the device due to the high transmission of the F contact. (b) Spin signal measured on the detector part, i.e. between the F3 and N4 electrodes.

Typical appearance of the negative non-local signal is depicted in Fig.6.7(a), which shows an electronic wave function propagating pass the contact F3 due to its low transparency (high resistance: R_3) further to the contact N4 with high transparency (high resistance: R_4). The amplitude of such signal which originates from the interference effects is highly dependent on the position of the back-gate voltage.

Another indication of the existence of such mechanism are spin-valve measurements that are done between F3 and N4. An example of such measurement is shown in Fig.6.7(b). This behavior has been observed in other samples and can yield both negative and positive value of TMR. Measured TMR between F and N electrode cannot be explained by the resistor model.

6.5 Conclusion

We measured an oscillating non-local resistance which changes sign and magnitude as the back-gate voltage is swept in multi-terminal SWCNT devices. This resistance is modulated by the QD characteristics of the detection segment of the circuit and is in contrast with the expected constant background for the fixed magnetic field. We find that the sign change of the resistance is in agreement with classical resistor model of the three segments of which, each represent a QD. Furthermore, the amplitude of the signal is larger than that estimated from the classical resistor model and therefore interference

effects needs to be taken into account.

Chapter 7

Summary

7.1 Obtaining SWCNT

Individual SWCNT can be obtained both from suspension solution and by growing them directly on the surface. The tubes that come in suspension are grown using methods such as HiPCO or laser ablation, that are known to produce SWCNT of high quality. The main disadvantage of the suspension tubes is that the process of separating the tubes involves sonication, which can shorten the tubes. Moreover the surfactant used to dissolve the nanotubes in water can influence the contacts when making devices.

With a CVD system with the appropriate settings of the growing parameters one can obtain material of good quality [13]. The CVD process can however be sensitive and minor changes in growing parameters or raw materials can have a big effect on the quality of the material. The main advantages of the CVD growing is that the nanotubes are grown directly on the surface, where they are to be connected. Moreover the CVD system is relatively simple and the growing can be done in-house.

7.2 Ferromagnetic contact material and switching characteristics

PdNi has been proved to make a stable reliable contact to SWCNT and some good results [11, 12, 14]. The switching characteristics are however not optimal. The PdNi contact seem to be of many magnetic domains and magnetometry measurements have revealed that the easy axis of magnetization is not fixed in the plane of the sample. Permalloy and Co, which have better controlled magnetic properties, were used to make SWCNT spin-valves. The

main problem was the strange switching behavior of both materials and in the case of Co it didn't make stable reliable contacts to the SWCNTs.

In an attempt to combine the good connecting properties of PdNi and the good magnetic properties of Co, SWCNT were connected by PdNi/Co bilayer. Magnetometry measurements have shown that the easy axis of magnetization is in plane in such films and the switching characteristics have improved.

7.3 Temperature dependence of TMR

The temperature dependence of the TMR signal was measured in the temperature range between 1.8 and 5 K. The TMR signal of the SWCNT devices is highly dependent on temperature and for temperatures of ~ 10 K and higher the signal has totally disappeared. The temperature dependence of the TMR seems to be correlated with the temperature dependence of the conductance of the devices. However the relative changes between spin dependent and spin independent resistances in the spin valve with temperature are not sufficient to explain this behavior. The source of the temperature dependence could originate in the mixing of spin up and spin down states of the electron at the contacts.

7.4 Non-local measurements

Oscillating non-local resistance which changes sign and magnitude as the back-gate voltage is swept was measured in multi-terminal SWCNT devices. This resistance is modulated by the QD characteristics of the detection segment of the circuit and is in contrast with the expected constant background for the fixed magnetic field. The sign change of the resistance is in agreement with classical resistor model of the three segments of which, each represent a QD. Furthermore, the amplitude of the signal is larger than that estimated from the classical resistor model and therefore needs to take into account the interference effects.

Bibliography

- [1] M. N. Baibich *et al.*, Phys. Rev. Lett. **61**, 2472 (1988).
- [2] S. A. Wolf *et al.*, Science **294**, 1488 (2001).
- [3] I. Žutić, J. Fabian, and S. D. Sarma, Rev. Mod. Phys. **76**, 323 (2004).
- [4] H. W. Kroto, J. R. Heath, S. C. O'Brien, R. F. Curl, and R. E. Smalley, Nature **318**, 162 (1985).
- [5] S. Iijima, Nature **354**, 56 (1991).
- [6] S. J. Tans *et al.*, Nature **386**, 474 (1997).
- [7] K. Tsukagoshi, B. W. Alphenaar, and H. Ago, Nature **401**, 572 (1999), First spin transport measurement in CNT.
- [8] B. W. Alphenaar, K. Tsukagoshi, and M. Wagner, J. Appl. Phys. **89**, 6863 (2001).
- [9] B. Zhao, I. Mönch, T. Mühl, H. Vinzelberg, and C. M. Schneider, J. Appl. Phys. **91**, 7026 (2002).
- [10] B. Babić and C. Schönenberger, Phys. Rev. B **70**, 195408 (2004).
- [11] S. Sahoo, T. Kontos, and C. Schönenberger, Appl. Phys. Lett. **86**, 112109 (2005).
- [12] S. Sahoo *et al.*, Nature Physics **1**, 99 (2005).
- [13] J. Furer, *Growth of Single-Wall Carbon Nanotubes by Chemical Vapor Deposition for Electrical Devices*, PhD thesis, Universität Basel, 2006.
- [14] S. Sahoo, *An Experimental Investigation of Spin Polarized Transport in Carbon Nanotubes*, PhD thesis, Universität Basel, 2005.

-
- [15] S. J. van der Molen, N. Tombros, and B. J. van Wees, Phys. Rev. B **73**, 220406 **73**, 220406(R) (2006).
- [16] N. Tombros, S. J. van der Molen, and B. J. van Wees, Phys. Rev. B **73**, 233403 (2006).
- [17] P. M. Tedrow and R. Meservey, Phys. Rev. B **7**, 318 (1973).
- [18] M. Jullière, Phys. Lett. A **54**, 225 (1975).
- [19] W. J. M. Naber, S. Faez, and W. G. van der Wiel, J. Phys.D: Appl. Phys. **40**, 205 (2007).
- [20] C. Kittel, *Introduction to Solid State Physics* (Joh Wiley & Sons, Inc., 1996).
- [21] K. Yosida, *Theory of Magnetism* (Springer, 1996).
- [22] R. J. Soulen Jr. *et al.*, Science **282**, 85 (1998).
- [23] N. W. Ashcroft and N. D. Mermin, *Solid State Physics* (Saunders College Publishing, 1976).
- [24] D. K. Cheng, *Field and Wave Electromagnetics*, Second ed. (Addison-Wesley Publishing Company, 1989).
- [25] S. Mørup, *Nanomagnetism* (Kluwert Academic Publishers, 1993), chap. Studies of superparametnetism in samples of ultrafine particles, pp. 93–99.
- [26] W. Thomson, Proc. Roy. SOC. **8**, 546 (1857).
- [27] T. McGuire and R. Potter, IEEE Trans. magn. **Mag-11**, 1018 (1975).
- [28] G. Binasch, P. Grünberg, F. Saurenbach, and W. Zinn, Phys. Rev. B **39**, 4828 (1989).
- [29] E. Y. Tsymbal and D. G. Pettifor, Solid State Physics **56**, 113 (2001).
- [30] S. S. P. Parkin, N. More, and K. P. Roche, Phys. Rev. Lett. **64**, 2304 (1990).
- [31] S. S. P. Parkin, R. Bhadra, and K. P. Roche, Phys. Rev. Lett. **66**, 2152 (1991).
- [32] N. Mott, 1936 **153**, 699 (1936).

-
- [33] N. F. Mott, Proc. Royal. Soc. **156**, 368 (1936).
- [34] J. S. Moodera, L. R. Kinder, T. M. Wong, and R. Meservey, Phys. Rev. Lett. **74**, 3273 (1995).
- [35] R. Y. Gu, D. Y. Xing, and J. Dong, J. Appl. Phys. **80**, 7163 (1996).
- [36] Y. Qi, D. Y. Xing, and J. Dong, Phys. Rev. B **58**, 2783 (1998).
- [37] S. Datta and B. Das, App. Phys. Lett. **56**, 665 (1990).
- [38] A. Fert and H. Jaffrés, Phys. Rev. B **64**, 184420 (2001).
- [39] J.-H. Park *et al.*, Nature **392**, 794 (1998).
- [40] A. K. Geim and K. S. Novoselov, Nature materials **6**, 183 (2007).
- [41] P. Wallace, Phys. Rev. **41**, 622 (1947).
- [42] S. Reich, J. Maultzsch, C. Thomsen, and P. Ordejón, Phys. Rev. B **66**, 035412 (2002).
- [43] A. Hirsch, Angew. Chem. Int. Ed. **41**, 1853 (2002).
- [44] M. S. Strano *et al.*, J. Nanosci. Nanotech. **3**, 81 (2003).
- [45] M. Islam, E. Rojas, D. Bergey, A. Johnson, and A. Yodh, Nano Lett. **3**, 269 (2003).
- [46] G. Cowan, *Statistical Data Analysis* (Clarendon Press, Oxford, 1998).
- [47] D. Mawhinney *et al.*, Chem. Phys. Lett. **324**, 213 (2000).
- [48] J. Paredes and M. Burghard, Langmuir **20**, 5149 (2004).
- [49] M. Radosavljević, M. Freitag, K. V. Thadani, and A. T. Johnson, Nano Lett. **2**, 193 (2002).
- [50] W. Kim *et al.*, Nano Lett. **3**, 193 (2003).
- [51] M. Z. Atashbar, S. Member, B. E. Bejcek, and S. Singamaneni, IEEE Sensors Journal **6**, 524 (2006).
- [52] D. Mann, A. Javey, J. Kong, Q. Wang, and H. Dai, Nano Lett. **3**, 1545 (2003).
- [53] A. Javey, J. Guo, Q. Wang, M. Lundstrom, and H. Dai, Nature **424**, 654 (2003).

-
- [54] J. K. Böhlke *et al.*, J. Phys. Chem. Ref. Data **34**, 57 (2005).
- [55] K. S. Krane, *Introductory to nuclear physics* (John Wiley & Sons, Inc., 1988).
- [56] R. Martel *et al.*, Phys. Rev. Lett. **87**, 256805 (2001).
- [57] A. W. Overhauser and A. I. Schindler, J. Appl. Phys. **28**, 544 (1957).
- [58] R. Meservey and P. M. Tedrow, Phys. Rep. **238**, 173 (1994).
- [59] R. Thamankar *et al.*, App. Phys. Lett. **89**, 033119 (2006).
- [60] W. H. Meiklejohn and C. P. Bean, Phys. Rev. **102**, 1413 (1956).
- [61] W. H. Meiklejohn and C. P. Bean, Phys. Rev. **105**, 904 (1957).
- [62] S. Datta, *Electron Transport in Mesoscopic Systems* (Cambridge University Press, 1995).
- [63] H. van Houten, C. W. J. Beenakker, and A. A. M. Staring, *Single Charge Tunneling* (Plenum, New York, 1992), chap. Colomb-Blockade Oscillations in Semiconductor Nanostructures, pp. 167 – 216.
- [64] M. Bockrath *et al.*, Science **275**, 1922 (1997).
- [65] M. R. Buitelaar, A. Bachtold, T. Nussbaumer, M. Iqbal, and C. Schönenberger, Phys. Rev. Lett. **88**, 156801 (2002).
- [66] W. Liang *et al.*, Nature **411**, 665 (2001).
- [67] C. Gould *et al.*, Phys. Rev. Lett. **93**, 117203 (2004).
- [68] I. K. Yanson *et al.*, Nano Lett. **7**, 927 (2007).
- [69] H. T. Man, I. J. W. Wever, and A. F. Morpurgo, Phys. Rev. B **73**, 241401 (2006).
- [70] B. Zhao, I. Mönch, H. Vinzelberg, T. M. hl, and C. M. Schneider, Appl. Phys. Lett. **80**, 3144 (2002).
- [71] L. E. Hueso *et al.*, Nature **445**, 410 (2004).
- [72] M. Johnson and R. H. Silsbee, Phys. Rev. Lett. **55**, 1790 (1985).
- [73] F. J. Jedema, A. T. Filip, and B. J. van Wees, Nature **410**, 345 (2001).

-
- [74] X. Lou *et al.*, Nature Physics **3**, 197 (2007).
- [75] N. Tombros, C. Jozsa, M. Popinciuc, H. T. Jonkman, and B. J. van Wees, Nature **448**, 571 (2007).
- [76] B. Gao, Y. F. Chen, M. S. Fuhrer, D. C. Glattli, and A. Bachtold, Phys. Rev. Lett. **95**, 196802 (2005).

Appendix A

The CVD procedure

A.1 The catalyst preparation

The catalyst consist of three nanopowders materials $\text{Fe}(\text{NO}_3)_3 \cdot 9\text{H}_2\text{O}$, Al_2O_3 40 nm nanopowder and MoO_2Cl_2 . The catalyst materials were suspended in 2-Propanol and it were spread on the surface of the sample from that solution.

In order to ensure continuity over long time three stem solution of each catalyst have been made. 30 mg Al_2O_3 40 nm nanopowder, 93 mg $\text{Fe}(\text{NO}_3)_3 \cdot 9\text{H}_2\text{O}$, and 27 mg MoO_2Cl_2 where dissolved in 20 ml 2-propanol each. The working catalyst solution, from which the catalyst is spread on the surface of the samples. consist of 0.5 ml of each stem solution thinned with 18.5 ml of 2-propanol. This diluted solution proved to provide a feasible density of catalyst particles on the surface when spread appropriately [13].

A.2 The oven and the gas handling system

In Fig.A.1 a photo of the CVD oven and schematics of the CVD system. A carbon containing gas mixture is led in a quartz pipe through an oven. In this case three gases where used. Argon (Ar) as an inert gas, Hydrogen (H_2) for minimizing amorphous carbon deposit and methane CH_4 which is the carbon source. When exiting the oven the gas is led through a “bubbler”, a sealed glass full of deionized water. From the bubbler the gas is led out. The main purpose of the bubbler is to show if the gas is flowing through the system and out of the building as it should.

The gas handling system in shown in Fig.A.2. The pressure of the gasses when they are taken into the system is ~ 0.3 bar and that pressure is regulated on the pressure regulators on the gas bottles. The gasses are lead though one-way valves and then through the input valves to the flow meters. The

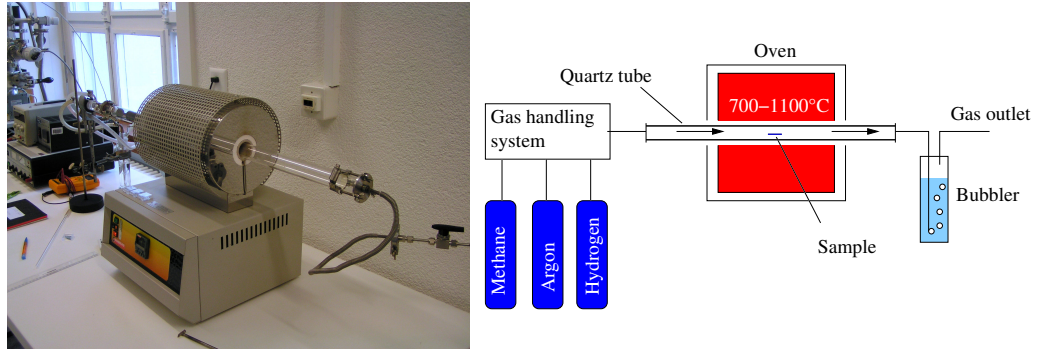


Figure A.1: A photo and schematics of the CVD system. The three processing gasses go first through the gas handling system where their flow is regulated and they are mixed. The gas mixture flows through a quartz pipe through the CVD oven. The hot gas from the oven is taken through a bubbler and then out.

flow meters a simple ball meters and they need to be calibrated according to the density of the gases and the pressure drop over them. The pressure is measured behind the flow meters where the gasses have been mixed. The normal pressure drop over the flow meters is ~ 0.2 bar. The standard recipe assumes that the pressure is of that size. The Gas mixture is then taken to the CVD where it goes through a one-way valve before it enters oven.

A.3 The growing protocol

1. Mount sample and close the tube.
2. Regulate the gas flow and the pressures.
3. Open all gas valves. Check if there are bubbles.
4. Flush the lines for 2 minutes.
5. Close the H_2 and CH_4 .
6. Keep Ar flowing at 1.4 l/min. The reading on the flowmeter should be 105 l/h.
7. Heat oven to growing temperature.
8. Open H_2 . The reading on the flowmeter should be 8 l/h
9. Close Ar.

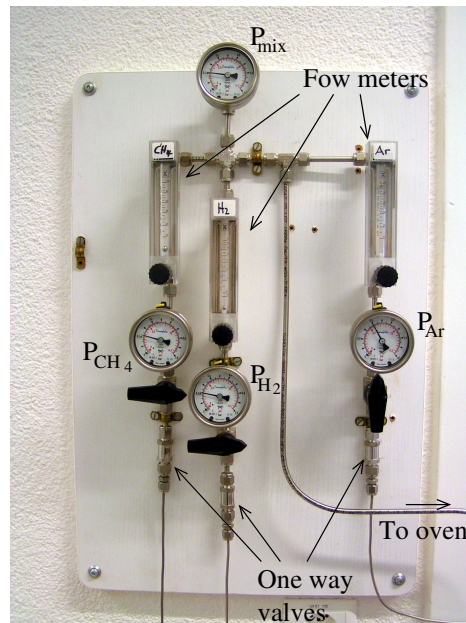


Figure A.2: The gas handling system. One way valves are where the gasses are taken into the system just before the input valves (in this photo only the Ar input valve is open). The pressure of the gasses is measured in front of the flow meters. Behind the flow meters the gasses are mixed and the pressure is measured.

10. Open CH_4 . The reading on the flowmeter should be 44 l/h
11. Let the gases flow for 10 min.
12. Open Ar.
13. Close CH_4 .
14. Let oven cool down to 550°C .
15. Close H_2 .
16. Sample can be unmounted when temperature is $\leq 350^\circ\text{C}$.
17. Close Ar.

Appendix B

Measurement setups

B.1 Setup of the linear response measurements

The TMR signal was measured by standard lock-in techniques at cryogenic temperatures. The cryostat used is Cryogenics He-4 cryostat equipped with a superconducting magnet. Sample temperature of ~ 1.75 K can be reached in this cryostat with the dipsticks used. Two type of dipsticks were used, one for measurements where the magnetic field (H) is applied in plane of the sample and one for H applied out of plane. Both dipsticks are simple “home

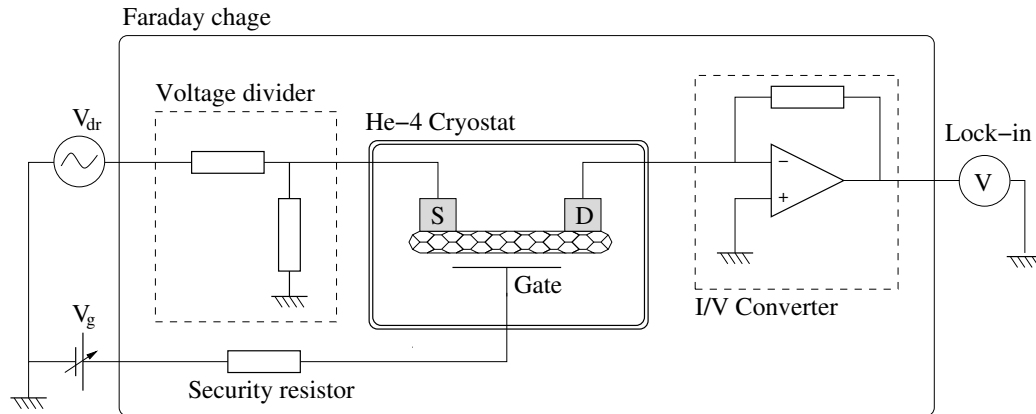


Figure B.1: Setup of the spin valve measurements. The measurements were done in a He-4 cryostat equipped with a superconducting magnet. The measurements are done using standard lock-in technique in voltage bias measurements. The current was measured using I/V-converter having gain of 10^7 V/A. The cryostat, the voltage divider and the I/V-converter were placed in a Faraday cage.

made” equipment. The resistance of the wires in them are low ($\sim 1.5 \Omega$) and the capacitances also.

Schematics of the setup is shown in Fig.B.1. The current is driven by the internal oscillator of a SR830 Lock-in amplifier. The driving signal (V_{dr}) was 1 – 2 V and that was divided by 10^4 , giving excitation voltage (V_{ex}) of 100 – 200 μV , which is applied on the source of the sample (S). The current flowing through the sample was measured by I/V-converter, having amplification of 10^7V/A , which was connected to the drain of the sample (D). The output of the I/V-converter was measured using the same lock-in as used as oscillator. The cryostat, the voltage divider and the I/V-converter were placed in a Faraday cage.

The gate of the sample was connected to HP3245A voltage source. A resistor of $10 \text{ M}\Omega$ was connected in series to the gate for security to prevent that to high currents leak through the gate in case of gate failure.

Measuring the TMR

The TMR was measured using the same setup as for measuring the linear response. The superconducting electromagnet of the cryostat was driven using Kepco bipolar current source. This current source works like an analogue V/I-converter giving 1 A/V and it can give current in the range of $\pm 10 \text{ A}$. The current source was controlled using the Auxiliary output of the lock-in amplifier which can give voltage in the range of $\pm 10.5 \text{ V}$ in steps of 1 mV. The magnetic field could be swept in the range of $\pm 1 \text{ T}$

B.2 Setup for doing grayscale measurements

The grayscale measurements were done in practically the same setup as the linear response measurements. The only difference is that the source-drain bias is (V_{sd}) taken from the HP3245A voltage source to the voltage divider. The driving voltage (V_{dr}) was added to V_{sd} in a transformer which is between the voltage source and the voltage divider. The voltage source can give voltages in the range of $\pm 10.1 \text{ V}$. The voltage divider in this case divided the input voltage with 10^3 giving possible source drain-bias ranging between $\pm 10.1 \text{ mV}$. V_{dr} in the grayscale measurements was normally 0.1 V giving excitation voltage of 100 μV .

Publications

Talks

- *Single Wall Carbon Nanotubes*
Invited talk at the Science Institute of the University of Iceland, Reykjavík, October 6, 2006.
- *Optimizing the Switching Characteristics of Ferromagnetic Contacts to Single Wall Carbon Nanotubes* Talk at the ICN+T 2006 conference in Basel, August 4, 2006.

Poster contributions

- *Oscillating non-local voltage signal in four terminal single wall carbon nanotube devices*
G. Gunnarsson, Jelena Trbovic, and C. Schönberger. Poster at the Frontiers in Nanoscale Science and Technology in Basel, January 6 - 8, 2008.
- *Spin transport in graphene strongly coupled to ferromagnetic leads*
J. Trbovic, H. Aurich, G. Gunnarsson and C. Schönberger. Poster at the Frontiers in Nanoscale Science and Technology in Basel, January 6 - 8, 2008.
- *Spin transport in single walled carbon nanotubes contacted by ferromagnetic electrodes*
G. Gunnarsson, J. Trbovic, C. Schönberger, A. Singh, and C. Sürgers. Poster for the visit of the Review Panel of the Swiss National Science Foundation (SNF) to the NCCR Nanoscale Science, Basel, April 25 - 26, 2007.
- *Electric field control of spin transport in carbon nanotubes*
S. Sahoo, T. Kontos, J. Furer, C. Hoffmann, M. Gräber, A. Cottet,

G. Gunnarsson, and Christian Schönenberger. Poster at the Annual Meeting of NCCR Nanoscale Science in Gwatt October 6 – 7 2005.

- *Classical and quantum behavior of periodic electron orbits in a lateral superlattice in a magnetic field*
Poster at the Danish Physical Society Annual Meeting 2002, Hotel Nyborg Strand, May 30 – 1 June 2002.

Paper

- *Large oscillating non-local voltage in multi-terminal single wall carbon nanotube devices*
G. Gunnarsson, J. Trbovic, and C. Schönenberger. arXiv:0710.0365
submitted.

Curriculum Vitae

Gunnar Gunnarsson

Born February 11, 1974 in Reykjavík, Iceland

Education

- 1994: Menntaskólinn við Hamrahlíð (Hamrahlíð College): Stúdentspróf (University entrance examination) in the field of Physics and mathematics.
- 1999: University of Iceland: B.Sc. in Physics and Geophysics.
- 2003: University of Copenhagen: Cand. Scient. in Physics under the supervision of Poul-Erik Lindelof. Title of thesis: *Classical and quantum behavior of periodic electron orbits in a lateral superlattice in a magnetic field.*
- Oktober 2003: Ph.D. in Experimental Physics at the University of Basel. Supervisor: Prof. Christian Schönenberger.

Working experience

- Summer 1995: Deutscher Bundestag.
- Summer 1996: Worked with a fellow student Ms. Kristín Jónsdóttir on measuring microseism around the geothermal powerplant in Svartsengi, SW-Iceland. Project supported by *Nýsköpunarsjóður Námsmanna* (Students' Development Fund) and the local power company.
- Summers 1997, 1998, and 1999: Various Surface geophysical measurements such as.

- Summer 2000: University of Iceland, Science Institute. Worked on a project titled “Defects in GaN” under the supervision of Prof. Hafliði P. Gíslason. Project supported by *Nýsköpunarsjóður Námsmanna* (Students’ Development Fund).
- Summer 2001: University of Iceland, Science Institute. Working with Dr. Sveinn Ólafsson.
- 2002 - 2003: Orkustofnun (National Energy Authority) – Research department. Working on Geothermal Well logging and groundwater hydrology.

Teaching experience

- Autumn semester 1996: Menntaskólinn við Hamrahlíð. Support teacher in Physics for deaf students.
- Spring semester 1999: University of Iceland. Teaching assistant in the experimental part of Physics II.
- Autumn semester 2002: University of Iceland. Teaching assistant in the experimental part of Physics I.
- Spring 2004: United Nation University – Geothermal Programme: Giving lectures on geothermal well logging.
- 2005 - 2007: University of Basel. Teaching assistant in nanocurriculum block course on Carbon nanotubes.
- Winter Semester 2005 -2006: Winter semester: University of Basel, Teaching assistant in “Anfänger Praktikum”

For valuable lectures and experimental guidance in my physics studies I want to thank following people

University of Iceland

Einar Guðmundsson, Eggert Briem, Robert J. Magnus, Páll Einarsson, Magnús Tumi Guðmundsson, Jón Ingólfur Magnússon, Þór Jakobsson, Leó Kristjánsson, Örn Helgason, Ari Ólafsson, Snorri Agnarsson, Þórður Jónsson, Helgi Björnsson, Hafliði P. Gíslason, Kristján Jónasson, Lárus Thorlacius, Viðar Guðmundsson, Þorvaldur Búason, Áslaug Geirsdóttir, Hreggviður Norðdahl,

University of Copenhagen

Henrik Smith, Jan W. Thomsen, Karsten Flensberg, Jens Jensen, Bjarne Andresen, Poul-Erik Lindelof

University of Basel

Christian Schönenberger, Wolfgang Belzig

Acknowledgements

At the end of this thesis I would like to thank all the people, who I have been working with during my Ph.D. First of all I would like to thank Prof. Christian Schönenberger for giving me the opportunity of doing a Ph.D. in his group. Thanks also to the co-referees, Prof. Jean-Philippe Ansermet and Dr. Takis Kontos for reading through the thesis and for interesting discussions in my defense. I should also thank Takis for his collaboration when he was a member of the Schönenberger's group.

Most of the measurements were done in a close collaboration with the postdoc Jelena Trbovic. I want to thank her for all her help and good advises.

For collaboration and friendship I would like to thank the present and former members of the Schönenberger's group namely, Christian Hoffmann, Bakir Babić, Erasmus Bieri, Alex Eichler, Roman Huber, Dino Keller, Andreas Kleine, Songmei Wu, Zheng-Ming Wu, Michel Calame, Szabolcs Csonka, Teresa Gonzalez, Jianhui Liao, Stefan Oberholzer, Markus Weiss, Jón Skírnir Ágústsson, Laetitia Bernard, Bong-Ryoul Choi, Jürg Furer, Matthias Gräber, Lucia Grüter, Soufiane Ifadir, Sangeeta Sahoo, and Sense Jan van der Molen. Thanks also to Sigurður Erlingsson (*Ef þú skyldir lesa þetta þá þakka ég þér hjálpina Siggí*).

I thank the secretaries, Astrid Kalt and Barbara Kammermann for taking care of the "bureaucracy", and Werner Roth for taking care of the cryogenic liquids.

Financial support for this work was provided by the NCCR on Nanoscience, the Swiss National Science Foundation, and the University of Basel.

Finally I want to thank my wife, Hafdis Hanna Ægisdóttir for all her support.